STATIC AND DYNAMIC WETTING OF ALIGNED NANOROD ARRAYS

by

JIANGUO FAN

(Under the Direction of Yiping Zhao)

ABSTRACT

A systematic study of the static and dynamic wettability of nanorod array surfaces prepared by glancing angle deposition is presented.

The static wettability of the aligned Si nanorod array surfaces was investigated by the sessile drop method. As-prepared nanorod samples were hydrophilic, while after hydrofluoric acid treatment or fluorocarbon coating, they became hydrophobic. The contact angle θ was successfully tailored from superhydrophilic (θ = 3^{o}) to superhydrophobic (θ = 170^{o}) by controlling the nanorod height, rod-rod separation, and chemical treatment. For the as-prepared samples, a wetting transition from a porous surface to a hemi-wicking surface was observed as the nanorod height increases. For HF treated samples, a transition from rough surface to composite surface was also observed. The transitions took place at the same critical nanorod height about 150 nm. The superhydrophilic and superhydrophobic behaviors as well as the wetting transitions are well interpreted by Wenzel's law and Cassie's law.

In the wetting experiment, nanorods bundled together to form patterns. This nanocarpet phenomenon presents a challenge for high aspect-ratio nanostructures to be used in liquid environments. Both the morphology of the pattern and the physical origin were investigated theoretically and experimentally. The bundling was caused by unbalanced capillary forces acting

on the nanorods either during the spreading process or the drying process. Thus controlling the wetting and dewetting process may reduce the bundling. Furthermore, the mechanical stability of several nanorod structures was compared and a capping layer method was proposed to minimize the nanorods from bundling.

Dynamic spreading and capillary rise experiments were investigated by fast CCD video imaging. During the spreading of water droplets on the nanorod surface, water also penetrates into the nanorod channels and transports faster than the apparent contact line. The contact line dynamics was similar to those on flat surfaces due to the spreading of the precursor film inside the nanorod channels ahead of the contact line. And the evolution of the precursor film follows Washburn's law. The scaling of these dynamics is almost not affected by the nanorod heights. For the capillary rise, the contact line and precursor dynamics are more complicated and they are affected by the sample size as well as the gravity effect.

INDEX WORDS: glancing angle deposition, contact angle, wetting, superhydrophobic, nanorod, nanocarpet effect, spreading, capillary rise

STATIC AND DYNAMIC WETTING OF ALIGNED NANOROD ARRAYS

by

JIANGUO FAN

B.S., Shanghai Jiao Tong University, China, 1999

M.S. Shanghai Jiao Tong University, China, 2002

A Dissertation Submitted to the Graduate Faculty of The University of Georgia in Partial Fulfillment of the Requirements for the Degree

DOCTOR OF PHILOSOPHY

ATHENS, GEORGIA

2007

STATIC AND DYNAMIC WETTING OF ALIGNED NANOROD ARRAYS

by

JIANGUO FAN

Major Professor:	Yiping Zhao
Committee:	William M. Dennis Richard S. Meltzer Henning Meyer Guigen Zhang

Electronic Version Approved:

Maureen Grasso
Dean of the Graduate School
The University of Georgia
December 2007

ACKNOLEDGEMENTS

First and foremost, I would give my sincere thanks to my advisor Dr. Yiping Zhao for giving me constant support and insightful advices to every piece of work that I have done in my Ph.D. study. Dr. Zhao has spent tremendous time to guide me to think broadly and deeply on every experimental phenomenon we have encountered. His devotion to science and hard-working spirit has set a good example for me and will continue to inspire me in my future work.

I would also thank all other members in my advisory committee, Dr. Dennis, Dr. Meltzer, Dr. Meyer, and Dr. Zhang, for providing me with insightful comments and suggestions to my research work.

I thank Dr. Zhang and his student Dustin Dyer for the collaboration work to understand the nanocarpet effect. I am much obliged to Dr. Jason Locklin for sharing his experience using chemical vapor deposition to coat a monolayer organic film on a solid surface. I thank Dr. John P. Shields and Dr. Jingsong Wu for instructing me using the SEM, TEM, ESEM, etc.

Finally I want to thank my labmates, Xiaojia Tang, Shihong Li, Steven Chaney, Junxue Fu, Wilson Smith, Yongjun Liu and Yuping He for the teamwork during these years. I thank Andrew Collins for working with me in the last two years and he has proven to be very helpful.

TABLE OF CONTENTS

Page

LIST OF TABLES

Page

LIST OF FIGURES

Page

CHAPTER 1.

INTRODUCTION

Wettability is a fundamental property of a solid surface. Controlling the wettability (hydrophobic/hydrophilic property) is critical to many processes from ink-jet printing, coating, oil recovery, to microfluidic systems, lab-on-a-chip assay. Over two centuries ago, Thomas Young and Pierre Simon de Laplace formulated the static wettability (contact angle) of a flat solid surface as the thermodynamic equilibrium of the interfacial energies of the contacting solid and liquid [1]. However, real surfaces are rarely flat. Instead, they are often physically rough and chemically heterogeneous. These two factors dramatically affect the apparent contact angles. To solve this problem, Wenzel and Cassie proposed two different models in 1936 and 1944 to modify Young's model [2,3]. These two models are still generally used today to explain hydrophobic/hydrophilic phenomena occurring on surfaces decorated with smaller and smaller features (e.g. from macroscopically roughened surfaces to micro-patterned surfaces). In 1997, botanists Barthlott and Neinhuis discovered the superhydrophobic lotus leaf on which water drops form spherical shapes and are able to roll off the surface easily. In addition, water drops collect dust particles on their path and make the surface clean [4]. This "self-cleaning" effect or lotus effect has inspired great interest in creating superhydrophobic surfaces and understanding the mechanism. This is also one of the objectives of this dissertation. Before giving a brief

introduction to the current study in the superhydrophobicity, I will define some basic concepts in wettability.

1.1. Fundamental concepts in wetting

1.1.1. Contact angle on a flat surface

When a water drop contacts a solid (flat) surface, it may take different shapes. Most commonly, we see shapes similar to Fig. 1.1(a), with an acute contact angle $\theta < 90^o$, and in this case, the surface is referred as hydrophilic; yet sometimes we may see shapes like Fig. 1.1(b), with an obtuse contact angle $90^o < \theta < 180^o$, and in this case the surface is called hydrophobic. In some special case, water will wet the surface completely ($\theta = 0^o$), as depicted in Fig. 1.1(c); and on the other extreme (ideally), we may expect to see a spherical drop depositing on a surface (Fig. 1.1(d), $\theta = 180^o$, which corresponds to completely non-wetting). The phenomena in Fig. 1.1(a) and 1.1(b) are also called partial wetting. Millimetric drops (more strictly, the size of the drop should be smaller than the capillary length $\kappa^{-1} = \sqrt{\gamma / \rho g}$ so that the effect of gravity is

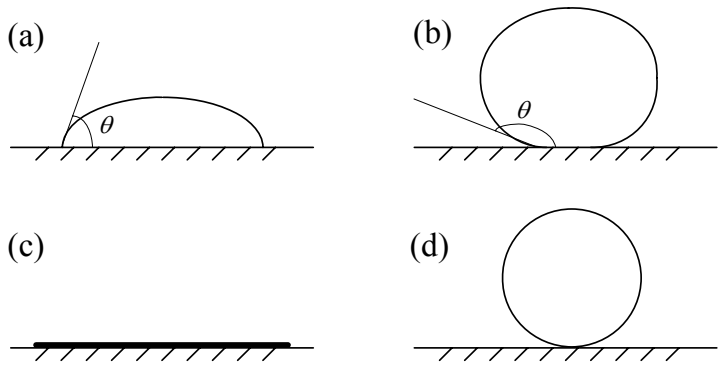

Figure 1.1. The shapes of liquid on a solid surface (a) hydrophilic (b) hydrophobic (c) complete wetting, and (d) complete non-wetting.

negligible, where γ is the surface tension of the liquid, ρ the liquid density and g the acceleration of gravity) take a spherical cap shape on a partial wetting surface due to the surface energy minimization. The area of the liquid-surface contact is outlined by a line (the rim of the drop) and it is termed the contact line. For a homogeneous surface, the contact line is a circle. The contact line is also called the three phase line or triple line since this is where the gas (V), liquid (L), and solid (S) phases meet. Each interface has its surface free energy per unit area, namely γ_{SL} , γ_{SV} , and γ_{LV} (or γ) for the solid-liquid, solid-vapor, and liquid-vapor interface, respectively. Macroscopically, there are two common approaches to evaluate the contact angle.

a. Force approach

Figure 1.2(a) is a sketch showing the forces (here consider a unit length of line along the S-L-V interface) acting on the contact line. By balancing the forces in the horizontal direction, one obtains

$$\gamma_{SV} = \gamma_{SL} + \gamma \cos\theta , \tag{1.1}$$

or

$$\cos\theta = \frac{\gamma_{SV} - \gamma_{SL}}{\gamma} . \tag{1.2}$$

This is the well known Young's relation derived by Thomas Young in 1805 [1]. In the vertical

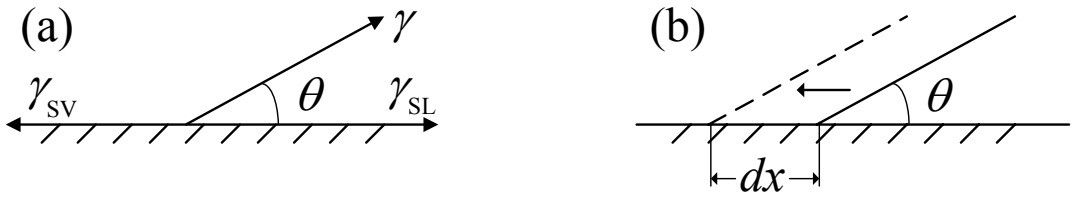

Figure 1.2. Sketch of (a) the forces on a three phase contact line, and (b) an infinitesimal displacement of the contact line along the solid surface.

direction, there is a force $\gamma \sin\theta$ pulling the surface, which is often balanced by the reaction force of the solid surface. However, if the surface is a thin film which only binds weakly to the substrate, the film may peal off. This is frequently encountered in experiments involving liquid-surface interactions.

b. Energy minimization

The second approach is associated with the total free energy change by a small displacement dx of the contact line (Fig. 1.2(b)). The energy change is

$$dE = \gamma \cos\theta \, dx + \gamma_{SL} dx - \gamma_{SV} dx . \tag{1.3}$$

Minimization of this energy, again we obtain the Young's relation (Eq. 1.2).

1.1.2 Contact angle on a rough surface

Practically, most surfaces are inhomogeneous. For a rough and heterogeneous surface, Young's law must be modified to describe the apparent contact angle θ^*.

1.1.2.1 Wenzel's law

For water wetting a rough surface, there are two possibilities: one is water following the surface features, and the other is water staying on top of the surface features with air inclusion. These two possibilities are sketched in Fig. 1.3. The problem again can be treated by the total free energy minimization. As shown in Fig. 1.3(a), assuming there is an infinitesimal displacement dx in the horizontal direction. The associated energy change can be written as:

$$dE = r(\gamma_{SL} - \gamma_{SV})dx + \gamma dx \cos\theta^* , \tag{1.4}$$

where r is the roughness factor defined as the ratio of the real surface area to the projected surface area on the horizontal plane. Intuitively, r is always larger than unity for a rough surface. Energy minimization requires $dE = 0$, thus the apparent contact angle θ^* can be related to the

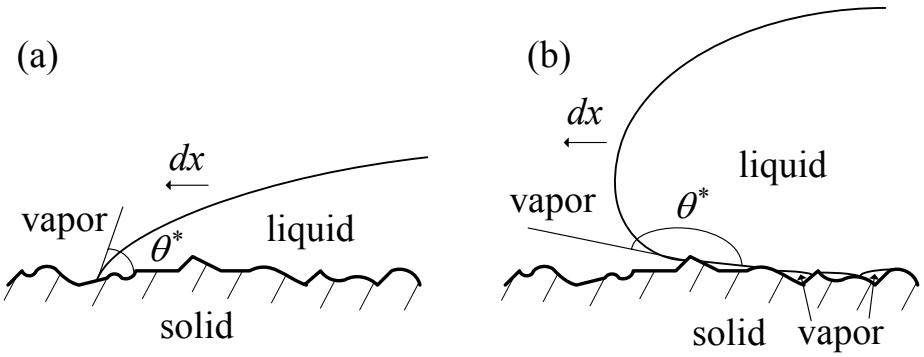

Figure 1.3. Infinitesimal displacement of the three phase contact line on a rough solid surface: (a) hydrophilic surface, and (b) hydrophobic surface.

Young's angle θ on a flat surface as:

$$\cos\theta^* = r\frac{\gamma_{SV} - \gamma_{SL}}{\gamma} = r\cos\theta\,. \tag{1.5}$$

This relation was first derived by Wenzel in 1936 [2]. Note, for a flat surface, $r = 1$, so Young's relation is naturally recovered. It is easy to draw some conclusions from Eq.1.5:

a. if a flat surface is hydrophilic, roughening makes it more hydrophilic, i.e. $\theta^* < \theta < 90^o$;

b. if a flat surface is hydrophobic, roughening makes it more hydrophobic, i.e. $\theta^* < \theta < 90^o$.

In short, surface roughness always enhances the wetting properties. However, the validity (applicability) of this relation should be examined further: according to Wenzel's relation, a complete wetting is achievable once the roughness factor $r = \dfrac{1}{\cos\theta}$ so that $\cos\theta^* = 1$, but what if r increases further? The value of $\cos\theta^*$ exceeds unity, which is mathematically impossible. From the derivation of Eq.1.5, it is implied that the drop should conform to the surface roughness. In the large roughness region, the contact phenomenon becomes the imbibition phenomenon. Figure 1.4 is a sketch showing a liquid drop spreading on a rough surface. Since the liquid is

spontaneously imbibed into the grooves, the actual spreading is on a solid-liquid composite surface. This modifies not only the static wetting property but also the dynamic spreading process. Bico et al. studied the imbibition phenomenon on textured surfaces, and defined a criterion for spontaneous imbibition [5,6],

$$\theta < \theta_c \text{ with } \cos\theta_c = \frac{1-\Phi_{dry}}{r-\Phi_{dry}}, \tag{1.6}$$

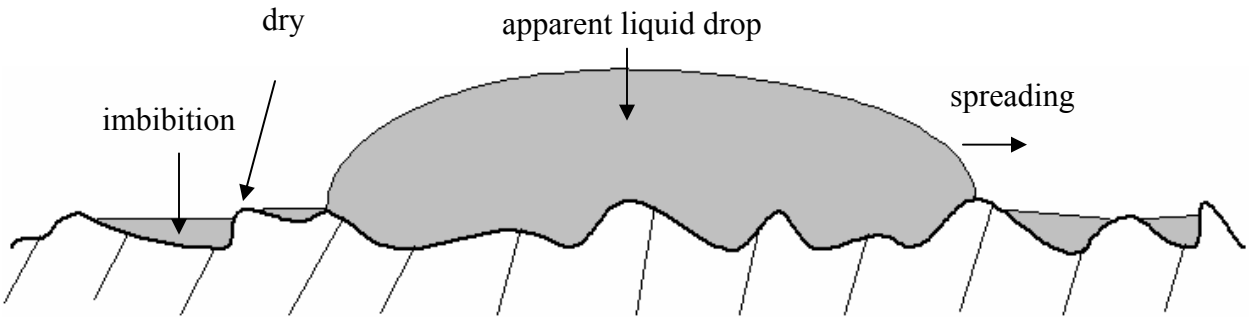

Figure 1.4. Liquid spontaneously imbibed into the surface grooves which forms a composite liquid-solid surface for the apparent liquid drop to spread on.

where Φ_{dry} is the solid fraction remaining dry. If this criterion is satisfied, a film will develop in the rough channels. This criterion also suggests that a drop will not be in the Wenzel's regime if $\theta < \theta_c$, due to the existence of the liquid film (precursor film) in the channels. In this case, the drop is actually sitting on an effective flat surface or a composite liquid and solid surface. The physical treatment of a composite surface will be discussed below.

1.1.2.2 Cassie-Baxter's law

Figure 1.3(b) is the case of a water drop sitting on top of the surface roughness features. In this case, the surface is not only geometrically rough but also chemically heterogeneous (a

composite surface of solid and air). Again, suppose the contact line displaces *dx* along the horizontal plane, and the total free energy change is [7,8]:

$$dE = \Phi_s r_\Phi(\Phi_s)(\gamma_{SL} - \gamma_{SV})dx + (1-\Phi_s)\gamma dx + \gamma dx\cos\theta^*, \tag{1.7}$$

where $r_\Phi(\Phi_s)$ is the roughness ratio of the wetted solid surface, Φ_s is the fraction of the projected solid surface that is wetted by the liquid, and $1-\Phi_s$ is thus the fraction of the air included in the interstices (it may be more precise also to include a roughness ratio for the liquid surface suspended on the air pockets since it can never be ideally flat). The roughness ratio r_Φ is introduced because the interface of the liquid-solid contact generally is not flat (Fig. 1.3(b)). It is important to note that in practice r_Φ is hard to determine precisely since it depends strongly on the material's wettability and the shape of the surface features [5]. It is reasonable to reduce this parameter to unity if the surface is ultrahydrophobic in which case the liquid only touches the very top of the texture or the top of the texture is ideally flat. Through energy minimization, we can simplify Eq. 7 and get [8,9]

$$\cos\theta^* = \Phi_s(1 + r_\Phi\cos\theta) - 1, \tag{1.8}$$

or rewrite it as

$$\cos\theta^* = \Phi_s r_\Phi\cos\theta + (1-\Phi_s)\cos 180^o. \tag{1.9}$$

Equation 1.9 is called the Cassie-Baxter law, which clearly shows that the apparent contact angle is the average effect from the two composites, solid and air, underlying the drop [3]. This law can be readily generalized to a complicated surface with more composites. For the hydrophilic case discussed in the last section, if a liquid film develops in the channels, the problem can be treated by the Cassie-Baxter equation. The angle 180^o in the above equation needs to be changed to 0^o, since a drop wets the same liquid film completely.

Now the question is: what is the condition for a drop to be in Wenzel's regime or Cassie's regime? Basically, for a hydrophilic surface, as the criteria stated in the last section is satisfied ($\theta < \theta_c$), a precursor film will impregnate the surface channels, and the drop is in a Cassie state. Otherwise, the drop will conform to the rough features and it is in a Wenzel state; for a hydrophobic surface, a drop also could be either in a Wenzel state or in a Cassie state. The criterion for a drop to be in the Cassie state is quite similar to that described in Eq. 1.6 [6]:

$$\theta > \theta_c \text{ with } \cos\theta_c = -\frac{1-\Phi_s}{r-\Phi_s}. \tag{1.10}$$

The solid fraction Φ_s can be determined theoretically for regularly structured surfaces. But for a randomly roughened surface, the difficulty is obvious. We notice that usually $\Phi_s << 1$, and $r > 1$, so the criterion can be reasonably approximated as $\cos\theta_c = -1/r$. Experimentally, the state can be determined by measuring the contact angle hysteresis, or sometimes the sliding angle. And it is also possible to induce a transition from the Cassie to Wenzel state.

1.1.3 Contact angle hysteresis

In Eq. 1.9, the coverage of solids Φ_s by the water drop is actually not unique for a given surface. When injecting water slowly (e.g. via a microsyringe) into a drop depositing on the surface, initially the contact line remains fixed, while the contact angle increases. There is a critical point, after which the contact line proceeds smoothly, and the contact angle after this point is called the advancing contact angle θ_a. Conversely, when taking water out of the drop slowly, the contact line first remains fixed while the contact angle decreases. After a certain point, the contact line recedes smoothly, and the contact angle after this point is called the receding contact angle θ_r. The difference between θ_a and θ_r is called the contact angle hysteresis

$\Delta\theta$, with $\Delta\theta = \theta_a - \theta_r$ and $\theta_a > \theta^* > \theta_r$. This relationship implies multiple possible (static) contact angles measurable from a surface because the water drop could exist in several metastable states (local energy minimum states). For an ideally smooth surface, the hysteresis should vanish and only one contact angle should be observed. However, for a real surface, the magnitude of the hysteresis is usually between 20^o and 50^o.

1.1.4 Lucas-Washburn's law

Imbibition into a capillary tube takes place if the tube is wettable ($\theta < 90^o$) by the liquid. The rate of the liquid penetration into the tube is a fundamental dynamic wetting problem with many practical implications in industrial and environmental applications including oil recovery, water distribution in soil substrates, surface coatings and printing of paper. The best-known solution of the imbibition rate was introduced by Lucas [10] and Washburn [11], which combined the Laplace relation with Poiseuille's equation.

Figure 1.5 shows the liquid column in a capillary tube with radius *R*. The capillary force that causes the liquid to rise in the tube is:

$$F_c = 2\pi R\gamma\cos\theta. \tag{1.11}$$

At equilibrium, balancing this force with the weight of the liquid column gives the final capillary rise height (Jurin's law)

$$z_{\max} = \frac{2\gamma\cos\theta}{\rho g R}, \tag{1.12}$$

where ρ is the liquid density and *g* is the gravitational acceleration. For the dynamics of the capillary rise, the equation of motion is described by the Newtonian equation

$$\frac{\mathrm{d}(MV)}{\mathrm{d}t} = F_c - F_\eta - Mg, \tag{1.13}$$

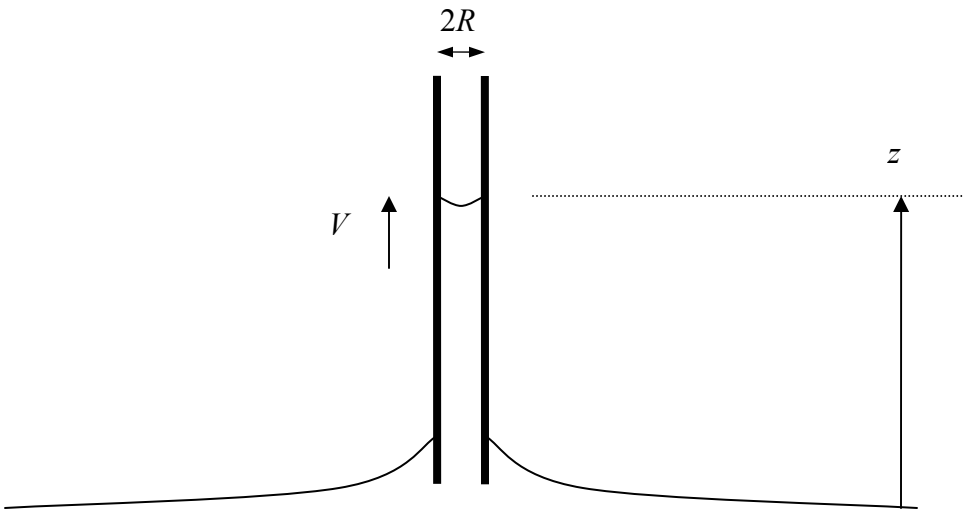

Figure 1.5. Capillary rise in a capillary tube with inner radius R. The height of the meniscus is z and the progression speed is V.

where M is the mass of the liquid, V is the capillary rise velocity, and F_η is the viscous drag force. The viscous drag force in a tube is given by Poiseuille's law. The assumptions are that the liquid is incompressible and viscous, and the liquid in the center of the tube is moving fastest while the liquid touching the wall of the tube is stationary (non-slip condition). Thus the drag force is written as

$$F_\eta = 8\pi\eta V z \,. \tag{1.14}$$

where η is the viscosity of the liquid. Discussing the dynamics of capillary rise, it seems natural to take the initial conditions for Eq. 1.13 to be $z(0) = \dot{z}\,(0) = 0$. However, there is a singularity at $t = 0$, when a finite force is applied to an infinitesimal mass $M = \pi R^2 \rho z (z \to 0)$. This problem will be discussed in details in Chapter IV. The effect of the inertial term $\frac{\mathrm{d}(MV)}{\mathrm{d}t}$ is explicitly written as $\pi R^2 \rho\left[(\ddot{z} + (\dot{z})^2\right]$, and it is usually significant only in the early stages of penetration or

when R is large and/or η is small. The gravitational term Mg in Eq. 1.13 can be neglected when R is small and when z is not too large or the capillary tube is horizontal instead of vertical. Under these restrictions, Eq. 1.13 is simplified to

$$2\pi R\gamma\cos\theta = 8\pi\eta\dot{z}z\ . \tag{1.15}$$

Integration leads to the Lucas-Washburn's law:

$$z = \sqrt{\frac{\gamma R t\cos\theta}{2\eta}}\ . \tag{1.16}$$

i.e. the penetration length of liquid into a capillary tube is proportional to the square root of time.

1.2 Current status of research in liquid-nanostructure interaction

Since the discovery of the lotus effect, there has been huge number of papers devoted to creating superhydrophobic surfaces. Many of them can be found in several review articles [6,12,13]. In general, there are two types of structures used in these studies, one mimicks the lotus leaf, which is composed of a hierarchical micro-nano binary structure, and the other is a single structure having one length scale. Jiang's group has made a comparison of artificial surfaces composed of aligned carbon nanotube (ACNT) arrays with and without the hierarchical structure [14-16]. When there was only an ACNT array film (the average length of the nanotube was about 3 μm and the outer diameter was about 60 nm), the surface was found to exhibit a large water contact angle ~ 159^{o}. But the sliding angle was larger than 30^{o}. This indicates a water droplet is sticky on the surface. After a slight modification to the preparation technique, lotus-like ACNT film was fabricated, with nanoscale ACNTs growing on the surface of microscale islands. The water contact angle was about 166^{o} and the sliding angle was only 3^{o}. This comparison demonstrates that the micro-nano heterogeneous structure may have a great impact

on the sticking behavior of water droplets. There are also many other examples of creating superhydrophobic surfaces by mimicking the hierarchical structure of a lotus leaf [17-35]. For example, Lu et al. used a simple method to form a low-density polyethylene (LDPE) floral-like superhydrophobic surface by controlling its crystallization behavior through adjusting the crystallization time and nucleation rate [18]. The reported contact angle was as high as 173^{o}, and the sliding angle was only 1.9^{o}. Sun et al. reported the nanocasting of a lotus leaf by poly(dimethylsiloxane) (PDMS) [24]. The positive replicate had almost the same morphology as the original lotus surface on both micro- and nano- scales. The water contact angle was 160^{o}, which is the same as that of a lotus leaf, and the sliding angle for a droplet with 1 mm radius was less than 2^{o}, indicating a quite good non-sticking surface. Zhu et al. fluorinated three types of surfaces (a micropatterned silicon substrate, a micropatterned carbon nanotube (CNT) array deposited on a smooth silicon wafer, and an aligned CNT array on a micropatterned silicon substrate) and compared their superhydrophobicity [33]. They discovered that the nanoscale roughness from the CNT array did not increase the water contact angle significantly. However, the hysteresis was greatly reduced. Furthermore, the combined micro-nano structure reduced the design requirement for a superhydrophobic surface. These examples further demonstrate that a combination of micro-nanostructure is important for non-sticking surfaces.

However, a pure micro- or nano- structure can also be non-sticking, as can be seen from several examples such as the Johnson and Dettre's experiment [36], the regular nanopatterns formed by e-beam lithography [37], CNTs coated with poly(tetrafluoroethylene) (PTFE) [38] and the slender silicon spike arrays by photolithography [39].

Two special goals in the area of surface wettability are to create transparent superhydrophobic surfaces and to create wettability switchable surfaces. Water-repellent

coatings on transparent surfaces have many practical applications like the automobile windshield, optical components and so on. It is realized that superhydrophobicity requires roughness and low surface energy. When roughness is increased, hydrophobicity is enhanced. However, since roughness is the source of scattering, increasing roughness means decreasing transparency. Thus to create a transparent superhydrophobic surface, the roughness must be carefully controlled. For visible light transparency, since the wavelength is in the range of ca. 400-760 nm, the surface roughness should not exceed 100 nm. Recent work has involved creating transparent superhydrophobic structures including silica nanoparticle based sol-gel and fluorocarbon self-assembly [40-42], a CVD method of growing silicone nanofilaments onto various surfaces [43], self-assembly of hydrophobic monolayers on electrochemically prepared transparent porous alumina films [44], and plasma modification of LDPE [45]. Wettability switchable surfaces are becoming more and more important due to the potential applications in biomaterials, biosensors, and smart microfluidic devices. According to Liu et al., these surfaces can be categorized into three types [46]: one is based on the modification of solid substrates with polymer molecules, which respond to external stimuli like temperature, light or solvent quality; the second is based on self-assembled monolayers (SAMs), which have response to temperature, electrochemical potential, light, or PH; the third is based on metallic oxides, especially TiO_2 and ZnO because of their attractive photocatalytic properties.

To summarize, the challenge is to fabricate nanostructures with controllable parameters such as the texture height, separation, composition, crystallinity, and functionality. There are many existing nanofabrication techniques to address this challenge such as electrochemical deposition, electrospinning, CVD, plasma etching, polymer sphere lithography, photolithography, e-beam lithography and so on. However, these techniques either have trouble to control the

nanostructure parameters precisely, or are very expensive. In this dissertation, I will employ a simple but versatile nanofabrication technique called glancing angle deposition (GLAD) to systematically design nanorod arrays which is capable of meeting the challenges presented above. In addition, the liquid-nanostructure interaction in this systematic study is not limited to the control over the wettability of a nanostructure surface, but also will investigate the applicability of classic wetting laws to nanostructured surfaces and the mechanical stability of nanostructures under the influence of liquid environment. The later two subjects are still not well studied yet.

.

1.3 Glancing angle deposition

Glancing angle deposition is a physical vapor deposition (PVD) method used to fabricate various columnar nanostructures, which combines oblique angle deposition (OAD) with dynamic substrate motion control.

The OAD has been studied for over one hundred years [47]. Early work involved PVD on static substrates oriented in a position where incident vapor flux arrived at oblique angles (off surface normal) [47-53]. The results revealed that tilting the substrate changes the properties of the film, which was thought to be a result of film morphology and in particular, the tendency of the 'grains' of the film to grow in the direction of the vapor source. In 1966, Nieuwenhuizen and Haanstra presented images from an electron microscope confirming that obliquely deposited films are comprised of columns that are tilted and grow in the direction of the vapor source [54]. Directional columnar growth is a result of atomic shadowing mechanisms that occur at the substrate surface. As shown in Fig. 1.6, during the initial stages of the PVD process, adatoms condense onto the substrate and form individual islands, or nuclei [55,56]. When the substrate is tilted such that incident vapor arrives at oblique angles, the topography of adatom nuclei results

in geometrical shadowing over regions of the substrate, preventing the coalescence of nuclei into a continuous thin film layer. Instead, the nuclei capture the vapor flux that would have landed in the shadowed regions, resulting in the formation of columns growing in the direction of the vapor source. It is noteworthy that this type of columnar growth is only possible from a

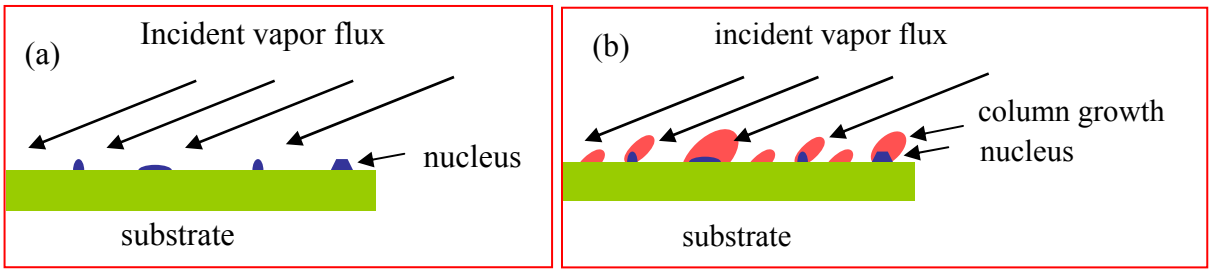

Figure 1.6. Geometrical shadowing and column growth. (a) Adatoms condense and form initial nuclei; (b) column growth as a result of the geometrical shadowing of the initial nuclei.

directional vapor source with a small angular distribution to maintain atomic shadowing. Another requirement of columnar growth is that the diffusivity of adatoms is limited. This requires that the temperature of the substrate should not be too high. At higher temperatures, the surface diffusivity of adatoms increases and at a certain point the diffusion length is large enough that they are able to diffuse into the geometrically shadowed areas [48,53].

In 1995, Robbie and Brett reported the GLAD technique [57,58], which is a major improvement to the conventional OAD technique. GLAD utilizes computerized control of substrate motion to change the relative vapor flux direction to manipulate the column growth and engineer the nanostructure of the resulting thin film. Figure 1.7 is a schematic representation of a GLAD system. Inside a PVD system, the source material is evaporated on the substrate at an oblique angle α (typically $\alpha > 80^{o}$), which is precisely controlled by a stepper motor (polar rotation, not shown). During the deposition, the substrate can be rotated about the normal axis by

another stepper motor (azimuthal rotation) as shown in the Fig. 1.7. Various nanostructures can be obtained by a proper combination of the oblique angle and the substrate rotation. Figure 1.8 shows several scanning electron microscope (SEM) images of GLAD thin films. The vertical posts in Fig. 1.8(a) are obtained by continuously rotating the substrate azimuthally at a fast rate, or more precisely, the rotation rate/deposition rate is large. A detailed study of the rotation

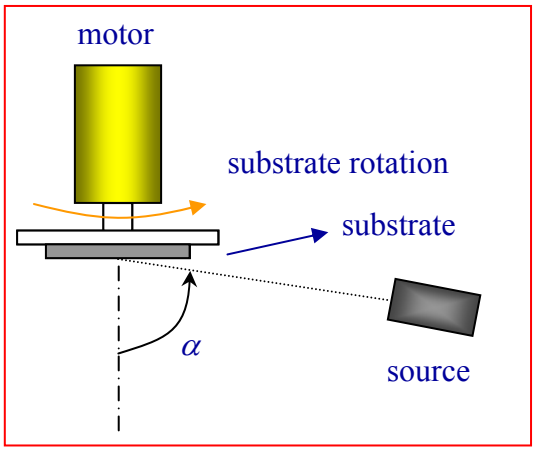

Figure 1.7. Schematic of the GLAD system

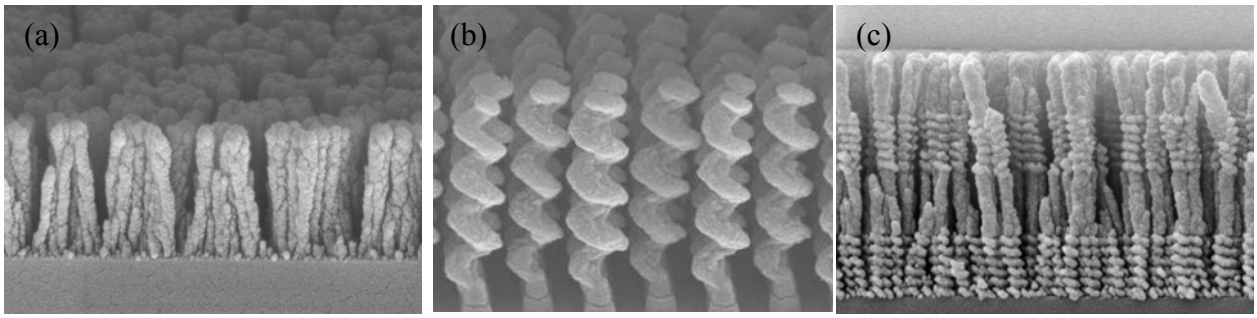

Figure 1.8. SEM images of several representative nanostructures fabricated by GLAD: (a) vertical posts, (b) regular spiral structure on a seeded surface, and (c) multilayer post/spiral structure

rate/deposition rate on the film morphology can be found in Ref. [59]. At slower substrate rotation rate, a spiral structure is obtained. Figure 1.8(b) shows a regular spiral structure grown on a flat surface patterned with regular polystyrene beads. Figure 1.8(c) shows a multilayer

post/spiral structure by changing the substrate rotation rate during the deposition. More GLAD structures will be introduced in later chapters and the conditions will be specified.

1.4 Organization of the dissertation

The material in the dissertation is arranged in the following manner:

Chapter 2 systematically investigates the equilibrium water contact angles of vertically aligned Si nanorod films by the sessile drop method. The affects of several parameters on the static contact angles are studied. Those parameters include the nanorod height, density, and chemical treatment. Both superhydrophobic and superhydrophilic surfaces are obtained, and the wetting transition between different wetting regimes is discussed.

Chapter 3 presents our finding of the nanocarpet effect and our step-by-step interpretation of this phenomenon. When a water droplet spreads on a vertically aligned Si nanorod surface, the nanorod array will bundle together to form percolated patterns. This so called nanocarpet effect presents a challenge for applications of high aspect-ratio nanostructures in liquid environments. We characterize the nanocarpet effect in several ways and employ both theoretical modeling and cryo-SEM to understand the mechanism of this phenomenon. Finally, we compare the mechanical stability of several typically nanorod structures and propose a method to stabilize the nanorod structure while maintaining the high porosity.

Chapter 4 studies the spreading and capillary rise on vertically aligned nanorod array surfaces. We compare the scaling relationships of the contact line and precursor film dynamics with those established laws governing the liquid dynamics on flat or microporous surfaces.

Chapter 5 summaries this dissertation and gives a vision for future work in the liquid-nanostructure interaction field.

CHAPTER 2.

SUPERHYDROPHOBIC AND SUPERHYDROPHILIC SURFACES

This chapter presents a systematic study of several factors that affect the static contact angles on a nanorod surface. The aim is to provide a clear route for creating superhydrophobic and superhydrophilic surfaces.

2.1 Tailoring the wettability of aligned nanorod array surfaces

2.1.1 Introduction

The wettability of a solid state surface is affected by both the surface roughness and the surface chemical composition [60]. It has been demonstrated that fractal rough surfaces and patterned microstructured pillar arrays can greatly alter the contact angle, depending on the wettability of the original flat surface: for a hydrophilic surface, a super-hydrophilic property can be developed, and for a hydrophobic surface, a super-hydrophobic property can be produced [37,61-67]. Recently, the super-hydrophobic property has also been found in chemically treated, vertically aligned carbon nanotube arrays and polyacrylonitrile nanofiber arrays [14,68]. The two studies showed that the one-dimensional nanowire/rod array has a dramatic effect on the wettability of the surface. Unfortunately the detailed relationships of the wettability and structure parameters have not been investigated. Recently, a systematic study has been performed by

Muller *et al*. based on Ge nanopyramids grown on Si(001) by the molecular beam epitaxy (MBE) method [69]. It was found that the contact angle hysteresis increased as the surface roughness increased. However, as compared to the nanotube and polyacrylonitrile nanofiber cases, the nanostructures in [69] were limited by the fundamental growth mechanism, and a high aspect ratio of the surface roughness could not be achieved [14,68]. Therefore, in order to probe how the nanometer features affect the wettability of a surface, the most difficult task is to fabricate and quantify nanostructures that can be systematically varied. In this section, we carry out a systematic investigation on the wettability of vertically aligned Si nanorod arrays with different heights (aspect ratio) fabricated by GLAD.

2.1.2 Sample preparation and Contact angle measurement

To fabricate Si nanorod samples, we fixed the vapor incidence angle at 86^{o}, the deposition rate was 0.2nm s^{-1}, and the rotation speed was 0.05 rev s^{-1}. All Si nanorod samples were fabricated in an e-beam evaporator, with a quartz crystal microbalance (QCM) to detect the normally grown film thickness *d*. In order to perform a systematic study, the final thicknesses of the QCM were set to be 25, 50, 70, 100, 500, 1000, 1500, and 2000 nm. We expected the height of the resulting nanorod arrays to increase correspondingly. The substrates were as-received p-type Si(100) wafer sonicated in acetone for 5 min. After rinsing with de-ionized water, the substrates were dried by compressed nitrogen. The control sample was a 500 nm Si thin film deposited under the same conditions, except that the substrate was stationary and the incidence angle was 0^{o}. The static contact angle of the as-grown control sample was measured within 30 minutes after the sample was taken out from the vacuum chamber by the sessile drop method (Dataphysics OCA 20). The sessile drop method uses an optical system to capture the profile of a

pure liquid on a solid substrate. The angle formed between the liquid/solid interface and the liquid/vapor interface is the contact angle. Figure 2.1 shows the picture of the OCA20 system. The profile of the drop is captured by a CCD camera (max 50 frame/second) and the contact angle is analyzed by software.

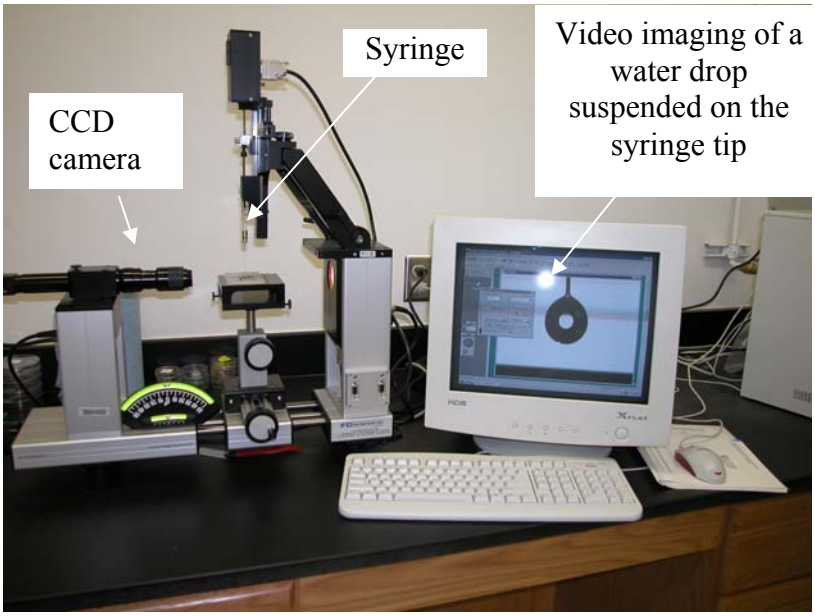

Figure 2.1 The contact angle measurement system: a liqud drop is dispensed onto a sample surface through a microsyringe, the profile of the drop is caputrued by a CCD camera.

The angle on the control sample was determined to be 50 ± 3^{o}. Another piece of the control sample was dipped into hydrofluoric acid (HF: 48–51% from J T Baker) for one minute. This process generates a thin layer of H-Si on the original fresh Si surface (usually it is covered with a very thin layer of silicon oxide). The contact angle of the HF treated surface was measured to be 78 ± 1^{o}. The contact angles of the as-grown nanorod samples were also measured within 30 minutes after the samples were taken out from the vacuum chamber. The as-grown Si nanorod samples were also dipped into HF for one minute and the contact angles were measured by the same sessile drop method. The structures of the as-grown nanorod samples were characterized by

a field emission scanning electron microscope (SEM; LEO 982).

2.1.3 Structural characterization of Si nanorod substrates [70]

The structure parameters of the nanorod films, such as the height h, diameter D, separation L of the nanorod, the occupation fraction f, and the roughness ratio r (ratio between the real surface area and the projected area), can be measured and derived from the SEM cross-

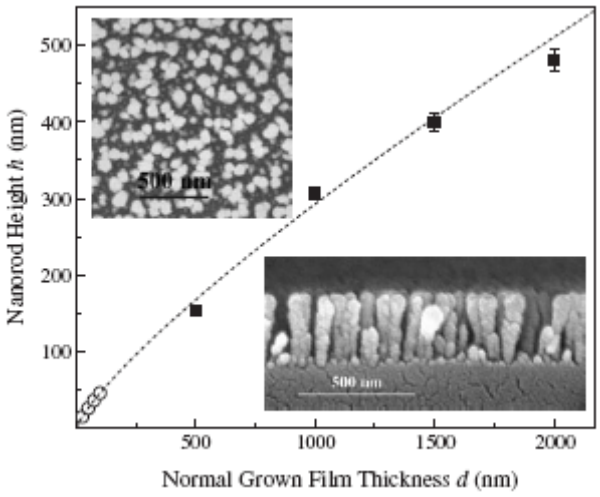

Figure 2.2. The height of the nanorod h versus normal film thickness d. The solid squares are the experimental data. The dashed curve is the power law fitting, and the open circles are the rod heights extrapolated from the fitting. The two inset SEM images are the top-view and cross-sectional view of the film at d = 1500 nm.

section and top-view images. Since the evaporated Si beam impinges at an angle with respect to the substrate surface normal, the actual Si vapor flux that arrives on the substrate surface will be smaller in quantity than that deposited on the QCM (ideally a $\cos\alpha$ relationship, where a is the vapor incidence angle). Therefore, the height of the nanorods h will be much smaller than the QCM thickness d. Figure 2.2 shows the Si nanorod height h as a function of the normal film thickness d. The measurable data show that the rod height increases monotonically with the normal film thickness. Representative SEM top view and cross-sectional view images of the Si

nanorods (d = 1500 nm) are shown as insets in Fig. 2.2. The nanorods have a uniform height across the entire substrate and the lateral arrangements of those nanostructures are random. Due to the limitation of the SEM resolution, we could not make a reliable measurement of the rod height for d < 500 nm. However, since the growth is dominated by the shadowing effect, according to the dynamic scaling hypotheses for surface roughness evolution during thin film evolution, the root mean square roughness (here the height of the nanorod h is proportional to the

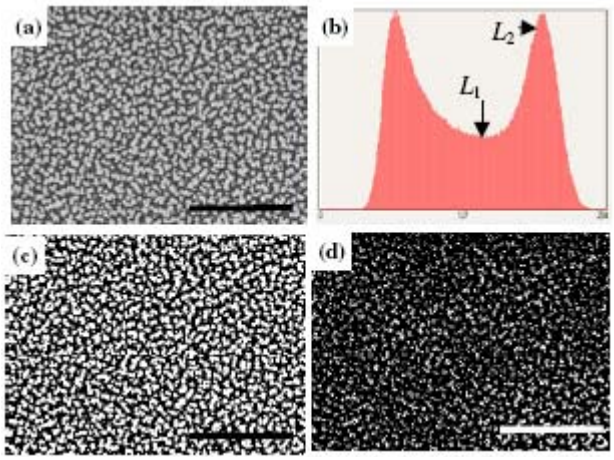

Figure 2.3. The calculation of the nanorod occupied surface fraction f. (a) An SEM top view image of d = 1500 nm; (b) the intensity distribution of image (a). The Y -axis is the number of counts and X-axis is the greyscale. The binomial distribution exhibits that there are only two characteristic surface heights of the rods: top and bottom. The location of L_1 is the threshold set for the nanorods (the minimum greyscale value between the two peaks), while L_2 is the threshold set for the top of the nanorods (10 greyscale values away from the peak). (c) The occupation of nanorods (white area) after threshold L_1.(d) The occupation of the tips of the nanorods (white area) after threshold L_2.The scale bars in (a), (c), and (d) are 2 μm.

roughness) obeys a power law with respect to the normal film height (or time) [71-74]. Thus, the rod height and the normal film height can be fitted by a power law, $h = 1.15d^{0.80}$.The dashed curve in Fig. 2.2 represents the fitting function, and the open circles are the extrapolated rod heights, 15, 27, 37, and 46 nm, at normal film thickness of 25, 50, 75, and 100 nm, respectively. The surface fraction f of nanorods was determined from the top view SEM image through a

threshold cut-off as shown in Fig. 2.3 (corresponding to d = 1500 nm). Usually the intensity (greyscale) distribution of the nanorod SEM image is a binomial distribution, and if the threshold (by an image processing software ImageTool) is selected as the minimum greyscale in between the two peaks, as shown in Fig. 2.3(b), L_1, we obtain the projected rod surface ratio f of 46%, as shown in Fig. 2.3(c) (the white areas are occupied by the nanorods). However, if the threshold is close to the higher peak position (10 greyscales away), indicated as L_2 in Fig. 2.3(b), the surface

Table 2.1 The structural parameters of the nanorod films obtained from the SEM images

Normal thickness d (nm)	Rod height h (nm)	Rod diameter D (nm)	Rod separation L (nm)	Rod coverage f_{L1}	Rod coverage f_{L2}	Effective surface area ratio r
500	154 ± 5	50 ± 6	76 ± 3	0.53	0.2	5.2
1000	307 ± 5	62 ± 6	80 ± 10	0.38	0.18	10.3
1500	400 ± 11	93 ± 14	174 ± 14	0.46	0.19	4.9
2000	481 ± 14	84 ± 6	152 ± 10	0.43	0.2	6.5

fraction will be greatly reduced to ~20% as shown in Fig. 2.3(d). For a nanorod surface shown in Fig. 2.2, assuming that each nanorod has a cylindrical shape, the roughness ratio r can be expressed as

$$r = 1 + \frac{\pi D h}{L^2}. \qquad (2.1)$$

Table 2.1 summarizes the structural parameters of the nanorod arrays measured from SEM images. As shown in Table 2.1, the nanorod structure greatly enhances the surface area.

2.1.4 Static wettability of Si nanorod arrays [70]

Figure 2.4 shows some representative shapes of water droplets on the as-deposited Si nanostructured films (left column of Fig. 2.4) and on the HF treated nanostructured films (right column of Fig.2.4). For the as-deposited hydrophilic Si surfaces, the contact angle θ^* decreases from 31.1^o to 3.2^o with increase of the normal film thickness from 25 to 2000 nm; while for the HF treated hydrophobic Si surfaces, the contact angle θ^* increases from 86.8^o to 142.7^o under the same growth conditions. We observed the following trends: for an original hydrophilic film, the increase of nanorod height made the film more hydrophilic, while for HF treated hydrophobic film, the increase of nanorod height made the film more hydrophobic. And the super-hydrophilic and super-hydrophobic properties of the nanostructured films depended closely on the height of the nanorods. In Fig. 2.5 we plotted the water contact angles of as-grown Si nanostructures and

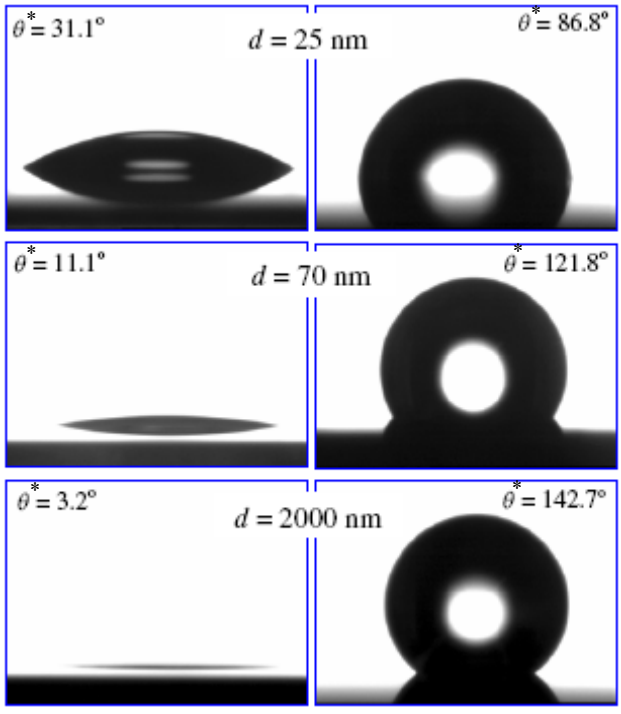

Figure 2.4. The representative shapes of water droplets on the as-deposited Si nanostructured films (left column) and on the HF treated nanostructured films (right column).

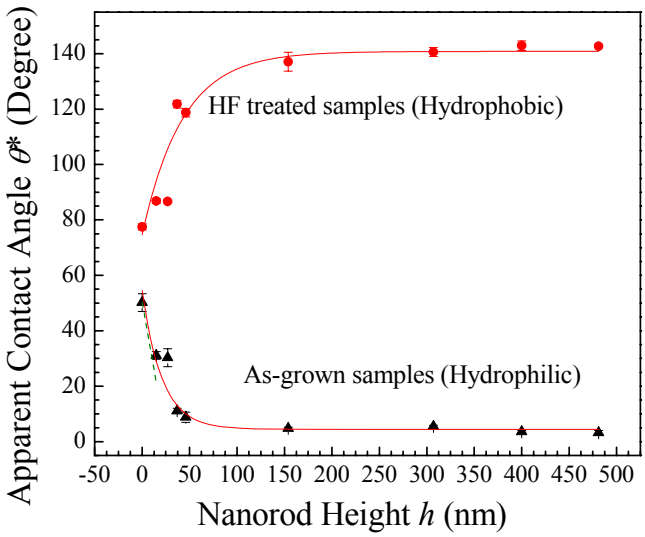

Figure 2.5. The water contact angles versus nanorod height for the as-deposited and HF treated nanorod films. The solid curves are the best fittings according to Wenzel's and Cassie's laws. The dashed curve is the calculation of the contact angles from the SEM data based on Wenzel's law.

HF treated Si nanostructures versus the nanorod height h. The trend observed in Fig. 2.4 was clearly demonstrated. Surprisingly, the contact angles at both the hydrophilic surface and the hydrophobic surface experienced a transition at $h \sim 150$ nm: for $h < 150$ nm, the contact angle had a steep increment or decrement, while for $h > 150$ nm, the contact angle tended to saturate.

According to classic wetting theory, we can treat the case of hydrophilic nanostructured surface as a rough surface [60], while treating the hydrophobic nanostructured surface as a composite surface, with air and hydrogen bond terminated Si islands [60]. According to the classic theory, the apparent contact angle θ^* for a rough surface obeys Wenzel's law [2]:

$$\cos\theta^* = r\cos\theta \tag{2.2}$$

where r is the roughness ratio and θ is the contact angle of a flat substrate. If Wenzel's equation

holds for the hydrophilic surface, then for different nanorod surfaces, θ^* is a function of nanorod height h. A detailed investigation of Fig. 2.5 revealed that when r and h followed an exponential decay relationship, $r = 1.55 - 0.69e^{-h/22}$, we obtained a best fit to the experimental results using Eq. 2.2. Using the data in Table 1, assuming that the rod diameter $D \approx 62$ nm and separation $L \approx 80$ nm are constant for different nanorod height, we can calculate the apparent contact angle θ^*. The dashed curve in Fig. 2.5 is the result from the calculation. For $h < 25$ nm, the calculated values follow the experimental data. However, for larger h, since the product $r\cos\theta > 1$, Wenzel's equation cannot predict the contact angles [75,76]. For these cases, the surface can be considered as being porous, and a special kind of imbibing (called hemi-wicking) will develop

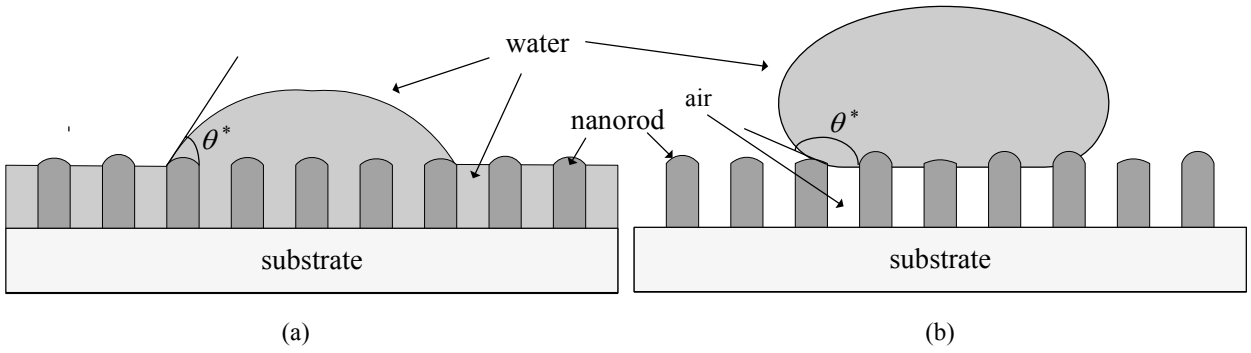

Figure 2.6. (a) Hemi-wicking: the water was first absorbed into the nanochannels, and then spread across the water–solid composite to form the equilibrium contact angle; (b) water only wetted the tips of the nanorods for the high aspect ratio hydrophobic surfaces.

due to the invasion of the liquid into the nanostructure, as shown in Fig.2.6(a) [76]. As a water droplet is deposited onto the surface, a small amount of water is imbibed into the nanorod array, and will fill the space between nanorods. Thus, the top of the nanorods remains dry [76]. For this hydrophilic behavior, since the top of the nanorod is not flat, the associated change in the surface free energy per unit length can be written as [76]:

$$dF = (\gamma_{SL} - \gamma_{SV}) r_f f \, dx - \gamma(1 - f)dx + \gamma \cos \theta^* dx, \quad (2.3)$$

where γ_{SL}, γ_{SV} and γ are the surface tensions of the solid–liquid, solid–vapor, and liquid–vapor interfaces, respectively, r_f is the roughness of the nanorod top that remains dry, and f is the nanorod fraction remaining dry. The equilibrium condition $dF = 0$ together with Young's relation gives

$$\cos \theta^* = r_f f \cos \theta + 1 - f. \quad (2.4)$$

For $h > 150$ nm, we can assume that both f and r_f remain constant; therefore the apparent contact angle is fixed. From the experimental data, let $f \approx 0.4$, $r_f \approx 1.55$, and $\theta = 50.2^o$; Eq. 2.4 gives a θ^* of 4.5^o, which is very close to our experimental result.

For the HF treated hydrophobic surface, the apparent contact angle θ^* can be expressed by Cassie's law [3]:

$$\cos \theta^* = f \cos \theta + (f - 1). \quad (2.5)$$

Here the roughness ratio factor r_f, as introduced in Eq. 1.7, for water covered nanorods is omitted. For the nanostructured films shown in Fig. 2.5, f is also a function of h. The best fit of the experimental data also results in an exponential decay relationship, $f = 0.18 + 1.03e^{-h/46}$, which gives $f \sim 0.18$ for h = 154, 307, 400, and 481 nm. From table 1 we have obtained that $f_{L1} \sim 0.53$, 0.38, 0.46, and 0.43; and $f_{L2} \sim 0.20$, 0.18, 0.19, and 0.20 for those heights, respectively. Clearly the experimental results suggest that the water only occupies the very top of the nanorods, as shown in Fig. 2.6(b). For $h < 150$ nm, according to Johnson and Dettre [77], the surface fraction of the water covered rod area will increase, which leads to the decrement of the contact angles. Therefore, the dramatic change of the slope of the contact angle at h = 150 nm indicates that there is a transition from a partially composite surface to a composite surface. Due to the lack of

detailed structural information for $h < 150$ nm, this interpretation needs to be further investigated.

2.1.5 Summary

We have measured the equilibrium water contact angles of vertically aligned nanorod Si films by the sessile drop method. For the as-deposited hydrophilic films, there was a contact angle transition from a rough surface to a hemi-wicking porous surface at nanorod height $h = 150$ nm, while for the HF treated hydrophobic films, a transition from a partially composite to a composite surface was also observed at the same nanorod height. The observed results can be reasonably well interpreted within the classical Young theory. The above results demonstrate that in order to change the wettability of a surface into a super-hydrophilic or super-hydrophobic surface, the nanorod array structures need to meet certain criteria. In addition, to create superhydrophobic surfaces, the nanorod height needs only to be over 150 nm.

2.2 Creating superhydrophobic surfaces

From our above study, we have demonstrated that at nanorod height $h > 150$ nm, water drops sit on top of the nanorod surface as shown in Fig. 2.6(b). The measured static contact angle is over 140^{o}. To create a real superhydrophobic surface that having the self-cleaning effect, which often requires the static contact angle $\theta^{*} > 150^{o}$ and low contact angle hysteresis or low sliding angle, we can either increase the Young contact angle θ or lower the solid fraction f as predicted from Eq. 2.5.

2.2.1 Self-assembled monolayer on Si nanorod surfaces

The Young contact angle θ can be increased by lowering the surface free energy. To

realize this, we can either directly deposit nanorods with a material having low surface energy or coat existing nanorods with low energy material. In our study, we use a self-assembled (heptadecafluoro-1,1,2,2-tetrahydrodecyl)trichlorosilane ($CF_3(CF_2)_7CH_2CH_2SiCl_3$: HFTS) monolayer on a flat Si (100) surface. The HFTS is applied onto Si nanorod surfaces fabricated by GLAD. The length of the HFTS molecule is ~ 1.7 nm [78] and the critical surface tension γ_c of the $-CF_3$ group is about 6 mN/m, which is the lowest critical surface energy ever reported [79].

In general, there are two methods to apply the HFTS monolayer, the rubbing method and the chemical vapor deposition (CVD) method. In the rubbing method, the HFTS is dissolved in a solvent, e.g. isopropanol, and the sample is immersed in the solution until the reaction is complete. After reaction, it is usually necessary to rub the surface with a soft cloth to remove excessive chemicals. This method will not be applicable for coating HFTS on Si nanorod surface since the surface can be easily destroyed by the rubbing procedure. Thus we use the CVD method. The setup is sketched in Fig. 2.7. The Si wafer or Si nanorod sample was first treated in piranha solution (sulfuric acid : hydrogen peroxide 4 : 1) for 10 minutes. After drying with compressed N_2, the sample was baked in an oven at 110^o for 30 minutes to remove adsorbed water molecules. Then the sample was loaded into a Wheaton vacuum chamber (Fisher scientific) as shown in Fig. 2.7. A drop of 40 μL HFTS was dispensed onto a microscope glass slide at the bottom of the chamber. Finally the chamber was pumped down using the wall vacuum. After 12 hours, the sample was taken out from the chamber and rinsed with toluene and DI water, and dried with N_2. The static contact angle was measured immediately with the sessile drop method and the sliding angle was measured with a custom built system.

The contact angle on the HFTS modified Si wafer was measured to be 110 ± 2^o (Fig. 2.8(a)), which is in agreement with the value reported in Ref. [78]. Using the same piranha

treatment and the same CVD method for the Si nanorod sample deposited at $\alpha = 86^{o}$, with h = 412 ± 19 nm, we find the contact angle was enhanced significantly to 155 ± 1^{o}, as shown in Fig. 2.8(b). We can estimate the apparent contact angle θ^{*} using Cassie's law. The Young angle θ for HF treated Si was $\theta_{HF} = 78^{o}$ and for HFTS treated Si was $\theta_{HFTS} = 110^{o}$. If we take the solid

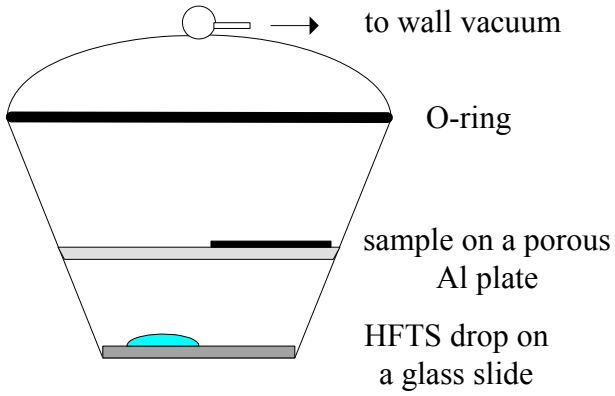

Figure 2.7. Sketch of the CVD setup for monolayer coating.

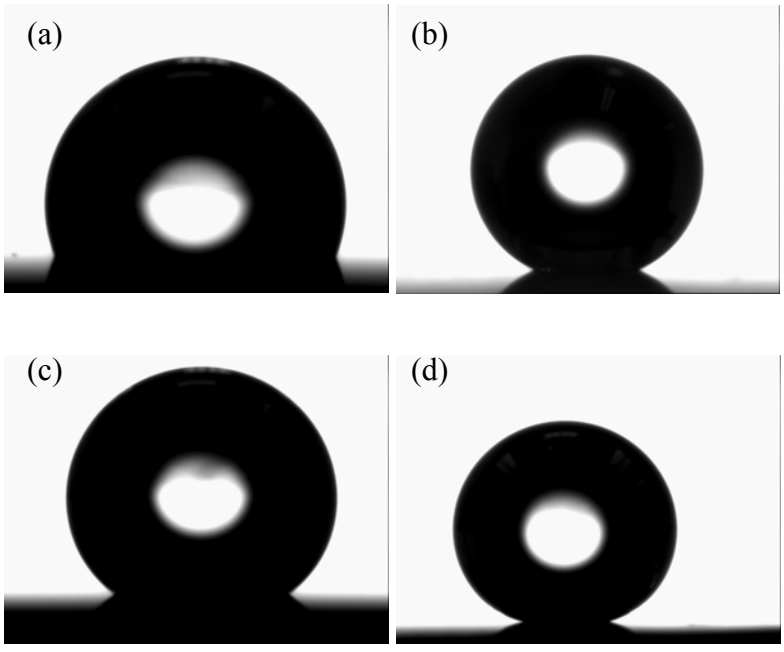

Figure 2.8. Contact angles measured for HFTS treated surfaces (a) Si wafer and Si nanorods deposited at α = (b) 86^{o}, (c) 84^{o}, and (d) 88^{o}.

fraction from threshold L_2, and the solid coverage f = 0.2, which is almost independent of the nanorod height for h > 150 nm, we obtain from Eq. 2.5, θ^*_{HF} = 139°, and θ^*_{HFTS} = 150°. The calculated θ^*_{HF} is in good agreement with the measured one, but the θ^*_{HFTS} deviates from the measured 155°. This deviation should arise from the change of the real solid fraction f in contact with water. As discussed in Chapter 1 after Eq. 1.9, f should be dependent on the surface chemistry: for more hydrophobic material, the water drop is more repelled (the capillary pressure is proportional to $\gamma\cos\theta/L$, where L is the gap of the nanorod channel) out of the channels, thus it contacts less with the nanorod tip. When f decreases, Eq. 2.5 will give a larger θ^*. We will examine the nanorod coverage effect next.

2.2.2 Change the nanorod density

From Cassie's law, to further increase the contact angle, the solid fraction in contact with water should be reduced. This can be achieved quite easily with the GLAD technique. At oblique angle α > 80°, the nanorod density is strongly dependent on α [80]. We will make a comparison of the density of Si nanorods grown at α = 84° and 88°, and hence the water contact angles after HFTS treatment. The normal Si film thickness used for this study was 1 μm.

Figure 2.8(c) and (d) clearly demonstrate that the water contact angles are quite different for the samples prepared at α = 84° and 88°. The contact angles are 148 ± 2° and 167 ± 3°, respectively. This difference implies that the density of the nanorods does change with the oblique incident angle. Figure 2.9 shows the top-view and cross-section SEM images of the two samples. Again we used ImageTool to estimate the nanorod coverage, using L_2 for the threshold, we obtain f_{84} = 22% and f_{88} = 14%. From Eq. 2.5, the calculated apparent contact angles are θ^*_{84} = 149° and θ^*_{88} = 155°, respectively. Clearly the estimated contact angle for the 88° sample is

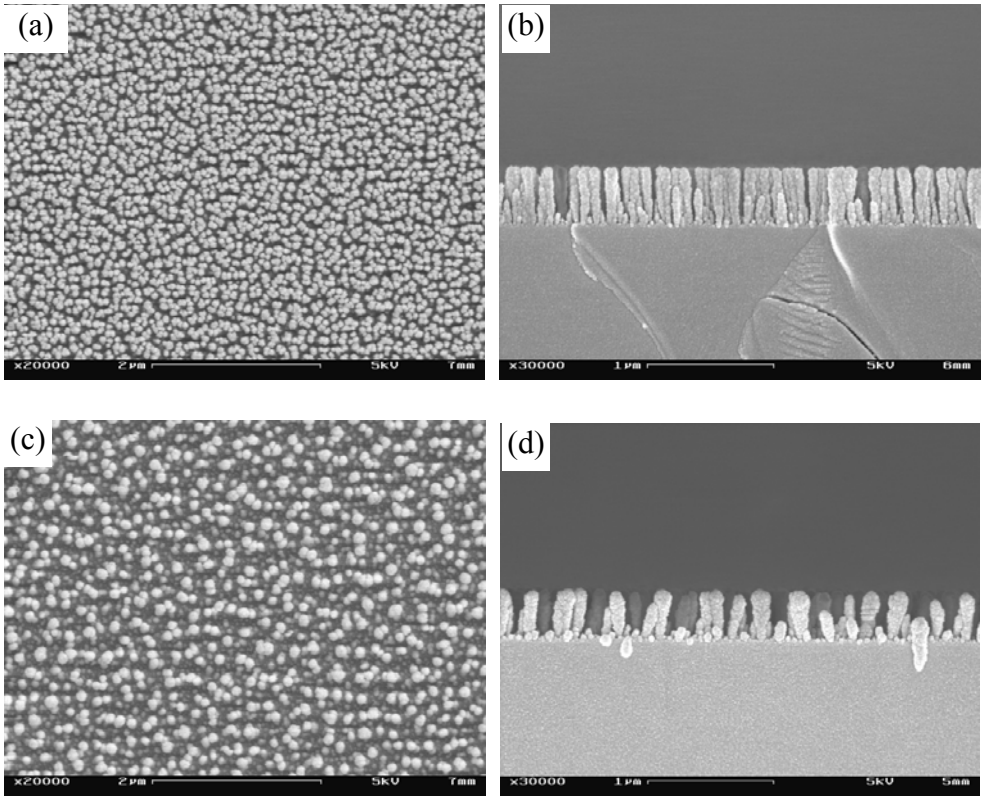

Figure 2.9. SEM top-view and cross-section images of Si nanorods grown at two different oblique angles: (a) and (b) for $\alpha = 84^{o}$, and (c) and (d) for $\alpha = 88^{o}$.

much less than the measured value. There are two possibilities for this inconsistency: one is that the nanorods grown at this extreme oblique angle are less uniform in height, so water may only contact with those very tall nanorods, and this further reduces the solid fraction *f*; the other possibility is that during the piranha treatment, some nanorods are detached from the substrate and reduces the density of the nanorods.

2.2.3 Characterization of a superhydrophobic surface

As defined previously, the demonstration of a superhydrophobic surface is not only that it has a high static contact angle, but it should also have a small sliding angle so a droplet on the surface is able to roll around freely. The method of measuring the sliding angle is shown in

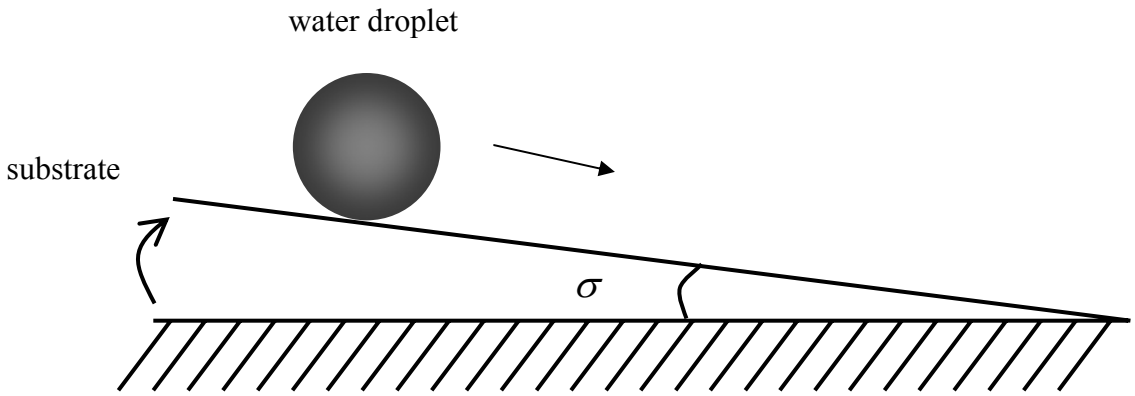

Figure 2.10. Sketch of the sliding angle measurement setup. At critical angle σ, the water droplet begins to roll off the substrate surface.

Fig. 2.10. Initially, the sample substrate was laid flat on a leveled surface, and then a water droplet was dispensed onto the surface by a microsyringe. Then, the substrate was tilted slowly until the droplet began to roll off the surface, the angle σ at this point is the sliding angle, and it can be simply read from a vernier attached to the setup. The volume of the droplet used was 10 μL. For the 84^o sample treated with HFTS, the sliding angle was $\sigma = 24 \pm 2^o$, and for the HFTS treated 88^o sample, $\sigma < 1^o$. This result shows the nanorod sample prepared at $\alpha = 88^o$ is indeed superhydrophobic after HFTS treatment.

The superhydrophobicity can also be tested with a droplet impact experiment. In Fig. 2.11, a droplet (6 μL) was released (Fig. 2.11(a)) from a microsyringe about 1 cm above the HFTS treated surface (Si nanorods at $\alpha = 88^o$), and the motion was monitored with a fast CCD camera (Pyramid Imaging: 210 frame/second). After the first impact (Fig. 2.11(b)) on the surface, the water droplet was able to bounce back to a very high level (Fig. 2.11(c)), which was about 64% of the original height. Then the bouncing could repeat many times with reduced height level each time (Fig. 2.11(d) and (e)) until finally the droplet jumped off the sample surface (Fig. 2.11(f)). The rebound height may provide a criterion for the hydrophobicity of a surface,

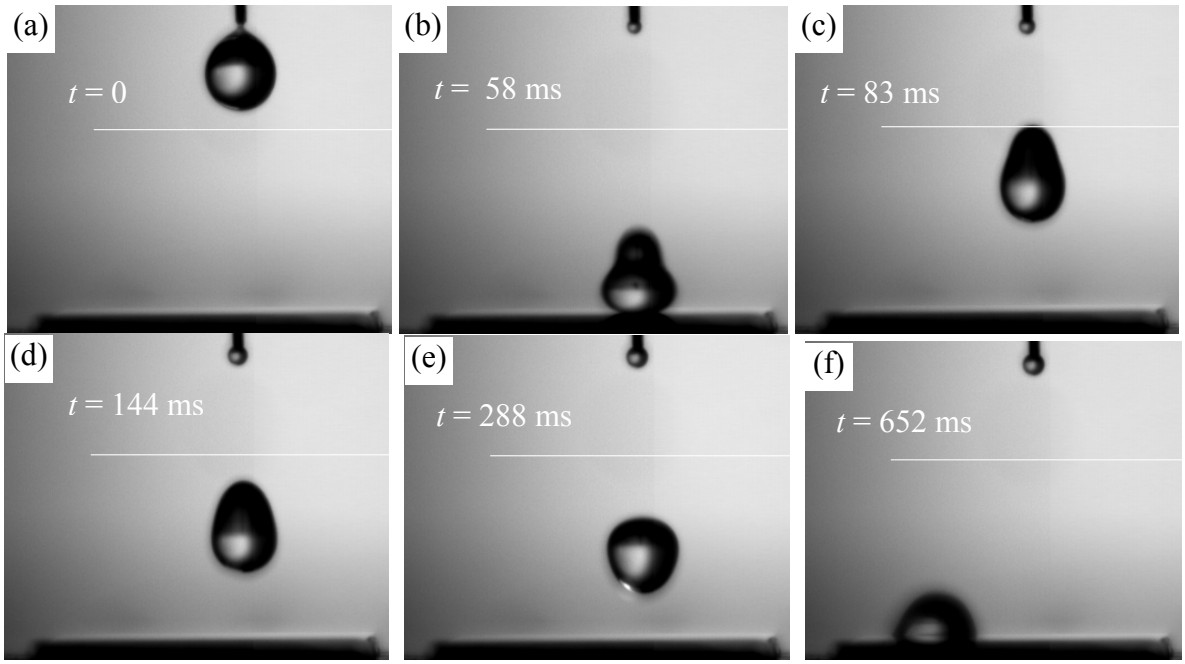

Figure 2.11. Snapshots of a water droplet impacting a superhydrophobic surface.

especially when the surface is extremely hydrophobic and the sliding angle is too small to be measured accordingly.

2.2.4 Summary

We have demonstrated that with an ultra low-surface energy material coating and reducing the coverage of the nanorods, a superhydrophobic surface with static contact angle about 167^{o} and sliding angle less than 1^{o} is obtained. In addition, fast video imaging of the droplet impacting may provide a new criterion for judging a superhydrophobic surface.

2.3 Conclusion

In this chapter, we have investigated the static wettability of aligned Si nanorod array surface prepared by GLAD. The as-prepared Si nanorod surface is hydrophilic and the HF

treated Si nanorod surface is hydrophobic. Both the hydrophilic and hydrophobic properties are highly dependent on the nanorod height. For the as prepared nanorods, the contact angle decreases when the nanorod height increases; while for HF treated surface, the contact angle increases when the nanorod height increases. However, after a critical nanorod height of about 150 nm, both contact angles saturate. This result is interpreted as the wetting transition from a rough surface to a hemi-wicking surface for the as prepared sample and from a rough surface to a composite surface for the HF treated one. Furthermore, we demonstrated that superhydrophobic surfaces can be obtained by simply combining a low surface free energy monolyaer coating and increasing the oblique deposition angle of GLAD.

CHAPTER 3.

NANOCARPET EFFECT: FORAMTION AND CHARACTERIZATION

3.1 Nano-Carpet Effect

3.1.1 Introduction

Recently there have been intense research efforts on how an array of nanostructures changes the wettability of a surface [14,68-70,81-83]. Structures like quantum dot arrays [69], polyacrylonitrile nanofiber arrays [68], half-shell nanoparticles [81], aligned carbon nanotube arrays [14,82], vertically aligned Si nanorod arrays [70], nanosphere lithography arrays [83], etc. have been fabricated and their wetting properties, especially the superhydrophobic property, have been investigated. These studies show that the surface chemistry and topology (such as individual nanostructure size, separation, and aspect ratio) of one-dimensional nanowire/rod arrays have dramatic effects on the wettability. Müller et al. has performed a systematic wettability study on Ge nanopyramids grown on Si(001) by the molecular beam epitaxy (MBE) method [69]. They found that the contact angle increased as the density of Ge nanopyramid increased. Lau et al. studied the wettability of the as-grown carbon nanotube arrays and poly(tetrafluoroethylene) (PTFE) coated carbon nanotube arrays [82]. They found that a water droplet could easily spread on the as-grown carbon nanotube array while showed superhydrophobic behavior on PTFE coated carbon nanotube arrays. The contact angle increased as the height of PTFE coated carbon nanotube array increased. In Chapter 2 we studied the

wettability of vertically aligned Si nanorods [70]. We found that as the height of the nanorod increased, the water contact angle of as-grown Si nanorods decreased (the superhydrophilicity), and the water contact angle of HF treated Si nanorods increased (superhydrophobicity). When the rod height exceeded about 150 nm, the contact angles for both as-grown samples and HF treated samples remained almost unchanged at about 4^o and 142^o, respectively. For the above mentioned experiments, the top surface of the vertically aligned nanostructures can be considered as a special kind of rough surface. Classical theories, such as Wenzel's equation [2] and Cassie's law [3,60], were successfully applied to describe the wetting of this kind of rough surface for many different experimental situations.

However, when compared to conventional rough surfaces, the vertically aligned nanotube or nanorod arrays have their own unique characteristics. The individual nanotubes or nanorods not only have a high aspect ratio (the ratio of feature's height to its diameter), but they also have an end anchored to the surface. The separation between the adjacent nanotubes or nanorods is on the order of 50 – 200 nm. In a liquid environment, such an arrangement will result in a large capillary pressure ($\Delta P \propto \frac{\gamma}{L}$, where γ is the surface tension of the liquid [60], and L is the separation) which could easily cause the nanotubes or nanorods to deform, thus changing the surface of the entire nanostructure assembly permanently. Several groups have reported that either pyramid or cellular structures were formed from CNT forests or polymeric nanofiber arrays [82,84-88]. Two different processes have been shown to be responsible for the structure change. Some studies have shown that after immersing into a liquid, and dried, the aligned nanowires (i.e., CNTs) bundled together to form cellular network structures [82,84,88,89]; while other studies showed that the bundling of nanorods occurred during the spreading of a liquid droplet [85,86]. Lau et al. [82] found that CNTs with a length of 2 μm formed pyramid-like

bundles after the spreading of water on the surface. The authors attributed this bundling to the attractive capillary forces that arose during the evaporative drying. Similar pyramid-like CNT clusters were observed by Nguyen et al during the CNT purification process [89]. In their study, the length of the CNTs was ~ 1 μm, and the diameter of the bundled CNTs was less than 1μm. Chakrapani et al. observed the formation of cellular networks after immersing and drying 50 μm long aligned CNT arrays [84]. The average size of the cell domain was about 100 – 200 μm. Both freeze-dried experiment and in-situ optical microscope observation suggested that the cellular network formed during the evaporation process. Recently Journet et al. also observed the formation of pyramid-like CNT clusters due to the evaporative drying of ethanol during the alkanethiol fuctionalization process [88]. The length of the CNTs was on the order of a few micrometers (typically 2um). On the other hand, Liu et al. also observed the cellular network formation on aligned CNT array (h = 19 μm) [86]. The size of the cellular domain ranged from 30 μm to 60 μm. Their observation of the color changing of the CNT array during spreading suggested that the pattern formed during the spreading process. Correa-Duarte et al. attempted to culture cells on the cellular patterns formed by CNTs [85]. They found that for small CNT lengths (~ 3 μm), pyramid-like CNT clusters formed. However, for CNT lengths of 35 μm and 50 μm, cellular networks with average domain size of 5-15 μm and 5-60 μm formed, respectively. All these observations have revealed two important features for a liquid interacting with CNT arrays: (1) For short CNT array (h < 3μm), pyramid-like clusters are formed; but for much longer CNT, cellular network structures are generally formed; (2) the cluster size, or the cellular domain size depends on the length (or the aspect ratio) of the CNT. The longer is the CNT array, the larger is the cluster size or the domain size. In our study, with the as-grown Si nanorod array, we also noticed a dramatic change in surface structure. This change in surface

structure may play a very important role in affecting the performance of devices developed based on these kinds of nanostructures. The questions remain whether the pattern change follows a statistical rule, and what the physical cause is for such a change. Answering these questions will help us not only to understand the mechanism of droplet spreading on a nanostructured surface, but also to find ways to either utilize or avoid this effect. In this chapter, we report a detailed characterization of the water droplet induced pattern (nano-carpet effect) on vertically aligned Si nanorods and its physical origin.

3.1.2 Experiment

The Si nanorod arrays were fabricated using the GLAD technique. The substrates were as-received p-type Si (100) wafers cleaned using RCA1 (solution of deionized (DI) water : hydrogen peroxide : ammonium hydroxide 5 : 1 : 1 heated to 70 ^{o}C) for 10 minutes. The vapor incident angle was fixed at 86^{o}, the deposition rate was 0.2 nm/s, and the rotation speed was 0.05 rev/s. Samples with normal film thickness from 200 – 2000 nm were fabricated for this study. The contact angles of the as-grown nanorod samples were measured by the sessile drop method within 30 minutes after their removal from the vacuum chamber. The structures of the as-grown nanorod samples and the water droplet induced pattern were characterized by SEM, a Mitutoyo optical microscope (1000×, bright/dark-field), and a measurescope (Unitron TMS6618).

3.1.3 Nanocarpet effect: pattern formation [90]

The top-view SEM image of the as-deposited Si nanorod array (normal film thickness 2000 nm) is shown in Fig. 3.1(a). The nanorods are uniformly aligned in vertical direction but randomly distributed in lateral directions on the Si substrate. The cross-section SEM image

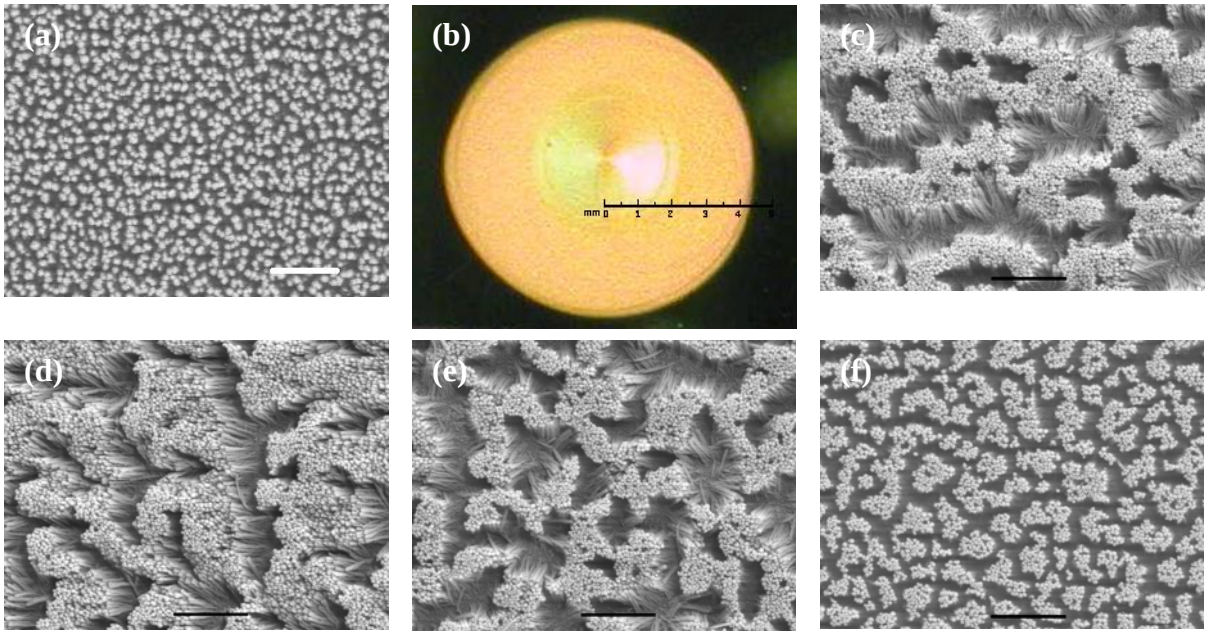

Figure 3.1. (a) SEM top view of as-grown Si nanorod surface. The scale bar is 1 μm. (b) Water mark formed after a droplet of 2.5 μl water spreading on the Si nanorod surface; (c) to (f) are the patterns in the water mark for r = 0 mm, r = 0.4 mm, r = 1.96 mm and r = 4.5 mm, respectively. The scale bars in those images represent 2 μm.

shows that the diameter of the nanorod increases gradually from its base near the substrate surface to its top which is consistent with previous observations [91]. The nanorods have an average diameter d_s = 22 ± 4 nm near the substrate, and an average diameter d_t = 103 ± 14 nm at the top. The rod-rod separation is about L = 131 ± 20 nm, and the height is about h = 890 ± 43 nm. On average, a single nanorod occupies an area of $A_{\text{unit}} = 1.7\times10^{-2}$ μm^2 if we assume that the nanorods are closely packed. The as-grown nanorod arrays show superhydrophilic behavior with a measured contact angle of 3.2 ± 0.8$^{\text{o}}$.

During the contact angle measurement, we observed an intriguing phenomenon: once the water droplet touched the nanorod surface, the color of the sample under the water droplet began to change from yellow green (nanostructured film color) to light orange. The light orange colored area spread as the water droplet spread on the surface. After the water droplet stopped

spreading, a shiny orange colored disk shaped mark (with a diameter d_o ~ 9 mm) was left on the sample's surface (Fig. 3.1(b)). Tilting the sample to a grazing angle, we observed a diffraction pattern around the center of the water mark that was very similar to the pattern of a commercial compact disk (CD). The inner disc shown has a diameter of d_i ~ 3.5 mm. Note that, for a 2.5 μL water droplet to form a 3.2° spreading on a flat substrate, ideally, the maximum spreading base will have a diameter of d_e ~ 7.7 mm, which is smaller than d_o but much larger than d_i. Since there is no chemical reaction that could create a new substance leading to the color change (the only possible reaction is the oxidation of Si during water spreading, which is slow and should not change the color), the only possible explanation for the color change is the physical change of nanorod structures during the spreading of the water. We believe that because of the high aspect ratio of the nanorods and the narrow nanochannels in-between, a sufficiently high capillary force will be generated to deform the rods so the spatial arrangement of the nanorod array may be altered. This will subsequently change the light scattering property of the surface, and thus, the color. We called this phenomenon the nano-carpet effect.

The SEM images confirmed this speculation. Figures 3.1(c) to 3.1(f) show some representative SEM images taken at several selected locations (represented by parameter r) from the center of the disk. Compared with the as-deposited film (Fig. 3.1(a)), the uniformly aligned nanorod array changed its morphology. In general, there are three distinct morphologies. Region I is at r = 0 mm. At the center of the water mark, there were long, micrometer sized channels, and the nanorods were severely deformed into a network of nanorod clusters with a width of about 1 – 2 μm. Region II is from r = 0.39 mm to 1.57 mm (the region with shiny disk shown in Fig. 3.1(b)). In this region, the nanorods were all tilted toward the center of the disk, which was confirmed by the SEM image taken at the left side of the center (image not shown). Region III is

from r = 1.96 mm to 4.5 mm (the orange region outside the shiny disk shown in Fig. 3.1(b)). In this region, the morphology of the nanorod array seemed to resemble that at the center, and there was no dominating direction in the tilting of the nanorods.

It appeared that the morphology of the surface changed systematically with the distance from the center. At a shorter distance from the center, the nanorods were deformed more laterally, and the clusters were large. At a larger distance, the nanorods were deformed less, and the clusters were small. The similarity in these three different regions is that nanorods are bundled together to form clusters while channels made by water invasion are connected throughout the entire area. It is clear that the nanorods along the edge of the water mark are pushed away from the channel, leaning towards opposite directions. This surface pattern is very similar to the patterns formed by percolation of thin metal films [92].

In order to obtain quantitative information from the surface pattern, two dimensional power spectra of the SEM images were obtained. Figure 3.2(a) shows a typical power spectrum, $P(k)$, for the SEM image taken at r = 1.96 mm and it has a ring-like structure. This demonstrates that there is a homogenous characteristic length in the surface pattern, indicating no dependence on any particular direction [72,93]. The center of the power spectrum ring k_c is directly related to the average cluster-cluster distance λ on the surface by $k_c = 1/\lambda$ [72]. All the other power spectra at different r have similar ring-like structures. Figures 3.2(b) and 3.2(c) show several examples of the circularly averaged power spectra for r = 0.39 mm, 0.78 mm, 1.17 mm, and 1.57 mm, respectively in Region II, and r = 1.96 mm, 2.74 mm, 3.51 mm, and 4.50 mm, respectively in Region III. In region II, where the nanorods are tilted towards the center, the power spectra do not change as a function of the distance r. The four power spectra overlapped with each other. The peak position, k_c, of the power spectrum, is in the range of 0.6 – 0.66 μm^{-1}, which

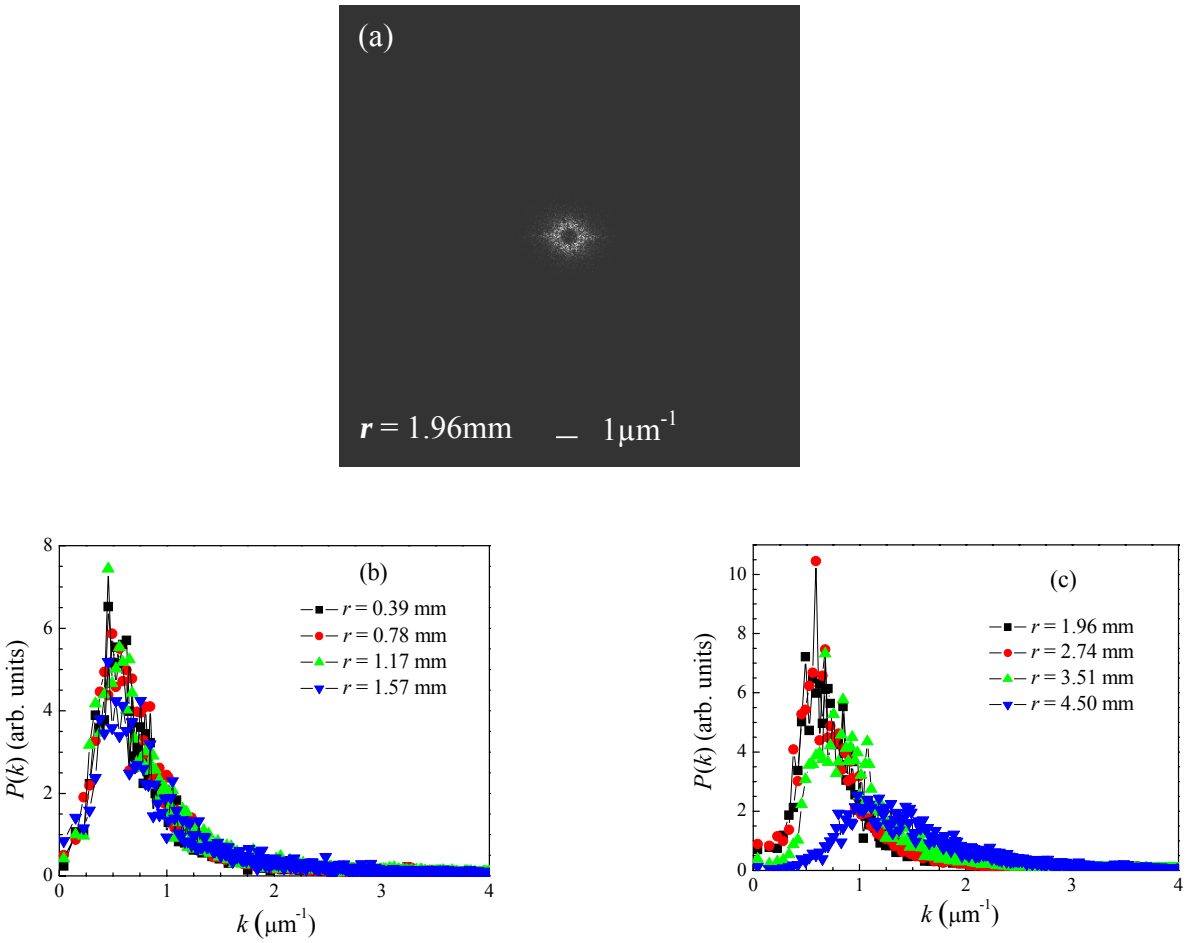

Figure 3.2. (a) A typical power spectrum for an SEM image (r = 1.96 mm); (b) Circularly averaged power spectra for r = 0.39 mm, 0.78 mm, 1.17 mm, and 1.57 mm, respectively (Region II); (c) circularly averaged power spectra r = 1.96 mm, 2.74 mm, 3.51 mm, and 4.50 mm, respectively.

corresponds to a cluster-cluster separation of 1.5 – 1.7 μm. However, in Region III, as shown in Fig. 3.2(c), not only the peak position k_c of the power spectra increases as r increases, the width of the peak Δk of the power spectrum also increases – The parameter Δk represents the uniformity and distribution of the nanorod clusters; therefore, when moving closer to the edge of the watermark, the nanorod cluster size and distribution become more random. Nevertheless, all the power spectra in Region III (and Region II as well) obey the same scaling function, $f(k/k_c) = k_c^2 P(k)$. This scaling relationship was originally proposed for percolated cluster

morphologies [92]. This result is very intriguing since the wetting process is a combined invasion and percolation process. The value of the ring location, k_c, can be determined by fitting the circularly averaged power spectra shown in both Fig. 3.2(b) and 3.2(c). Figure 3.3 plots both the k_c and λ versus the distance r. In Regions I and II (r < 1.9 mm), both k_c and λ are almost

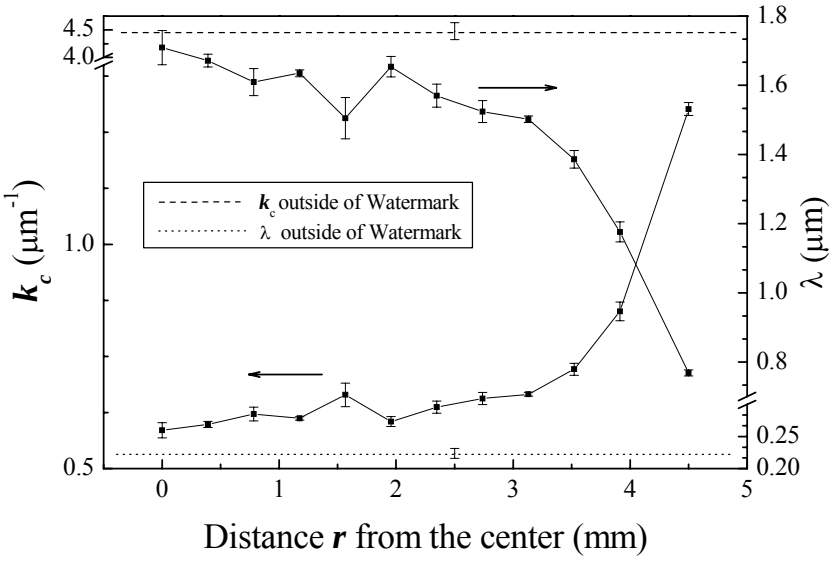

Figure. 3.3 The calculated center position k_c of the power spectra and the average separation λ of the nanorod clusters as a function of distance r from the center of the watermark.

unchanged, while in Region III, these two parameters change systematically with respect to the distance r: k_c increases and λ decreases as r increases. Particularly, at the edge of the watermark, k_c increases dramatically. k_c (or λ) reaches a constant outside of the watermark (as indicated by the dashed (dotted) line in Fig(3.3)). This observation is consistent with the power spectra.

3.1.4 Capillary deformation [90]

The SEM images also showed that the deformation of the nanorods varies with locations: the closer the nanorods to the center, the larger the induced displacement. This was supported by

the power spectra analysis in which the average cluster separation, λ, decreases. All the SEM images showed that the top of the nanorod arrays occupied about 50% of the entire surface area (by the ImageTool threshold setting, as introduced in Chapter 1). Therefore, the average cluster size can be estimated as $l = \lambda / \sqrt{2}$. In addition, as shown in Fig. 3.1, before water wetting, the nanorods on as-grown sample are all separated, but after wetting, the nanorods are closely packed to form clusters. If we assume the nanorods are regularly packed in clusters with uniform diameter D, then the average number of nanorods in one cluster can be estimated as

$$N = \frac{A_{cluster}}{A_{unit-cp}} = \frac{\pi l^2 / 4}{\sqrt{3} D^2 / 2} = \frac{\pi l^2}{2\sqrt{3} D^2}, \tag{3.1}$$

where $A_{cluster}$ is the average area occupied by a cluster, and $A_{unit\text{-}cp}$ is the area of a unit cell of a closely packed pattern. Assuming that from the substrate to the top of the nanorods the cluster has a shape of an inverted frustum, then the diameter l_b of the base circle is

$$l_b = 2\sqrt{NA_{unit} / \pi}. \tag{3.2}$$

Then the lateral displacement y of the outer most nanorods with respect to the surface normal direction can be estimated as

$$y = (l_b - l)/2. \tag{3.3}$$

This displacement y is caused by the water-nanorod interaction. Figure 3.4 shows the average lateral displacement y, which is almost monotonically decreasing with the distance r. In addition, the maximum lateral displacement $y_{\max}$ of the nanorods on the edge of the cluster can be measured from the SEM images directly. Figure 3.4 also plots the maximum shift $y_{\max}$ as a function of the distance r. In Regions I and II, the shift $y_{\max}$ is large and increases with distance, while in Region III, the shift is decreasing. Compared with the average displacement y calculated from the power spectra, $y_{\max}$ is several times larger.

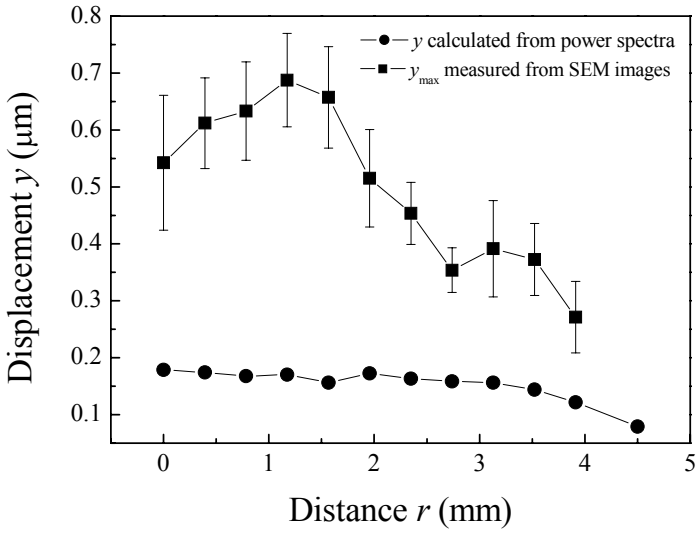

Figure 3.4. The average lateral displacement y of nanorods calculated from power spectra and the measured maximum lateral displacement y_{max} from SEM at different location of the watermark.

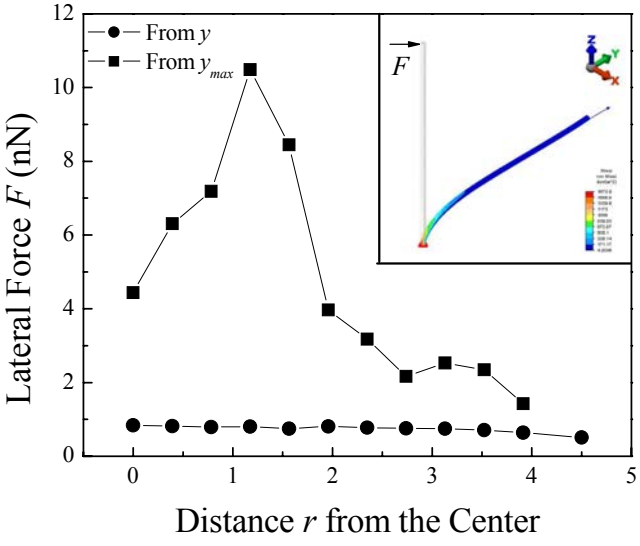

Figure 3.5. The lateral loading force F calculated from the displacement by finite element analysis. The force calculated from y_{max} is several times larger than that calculated from y. The insert shows the location where the force is applied to the nanorods.

To estimate the range of the forces encountered by the nanorods, we considered a uniform cylindrical rod with a horizontal force F acting at the top (see inset in Fig. 3.5). Because of the large deformations seen in the nanorods, we used nonlinear finite element analysis (FEA) to model a single silicon nanorod isolated from its surrounding neighbors. Here, a commercial FEA software package by *ALGOR*® was used. To simulate the bending of an actual nanorod, which has roughly the shape of an upside down frustum, two cylindrical models were created. The smaller model had a diameter of 20.4 nm (the dimension at the base of an actual rod), and the larger model had a diameter of 109.2 nm (the dimension at the top of an actual rod). Both rods had a height of 900 nm. The smaller model used 3239 elements and the larger model consisted of 3034. These elements were more closely spaced at the base of the nanorod models to provide good continuity in the stress calculations since high stress is expected near the connection of the nanorod to the substrate. To provide an estimate of the force needed to cause the deformations seen in the SEM images of the nanorod covered substrate, the base of each rod was constrained in all 6 degrees of freedom, and a force F was applied in a direction perpendicular to the rods' central axis at the free end. For this study, nonlinear and large-deformation elastic analyses were performed. The modulus of elasticity, E, of silicon was taken to be 130 GPa with a Poisson's Ratio, v, of 0.28 [94]. The force F was applied gradually over the course of 500 time steps (250 for loading and 250 for unloading) with $F_{min} = 0$ nN and $F_{max} = 98$ nN. For each time step, the deflection at the free end was obtained. Figure 3.5 shows the calculated force experienced by the nanorods for the average lateral displacement and maximum lateral displacement from the smaller model. The maximum forces are estimated between 1.26 nN and 10.1 nN, while the average forces obtained were between 0.5 and 0.9 nN, depending on the distance from the center of the water mark. In Regions I and II, the force is between 4 to 10

nN, while in Region III, the force decreases by about one order in magnitude. This indicates that, the water-nanorod interaction close to the center of the water mark is much stronger than those at the edge, and it decreases as the distance increases. As a note, the force values reported above only consider the amount of force needed to deform (nonlinear-elastically) the structures to the observed displacements shown in Fig. 3.4. We believe that nonlinear plastic deformation may also contribute to the residual deformation observed in Fig. 3.1(c)-(e).

If we assume that this lateral force is the result of capillary attraction, then the capillary force we obtained with the FEA model was estimated in the range of 1.26 nN to 10.1 nN. However, according to Kralchevsky et al. [95], for two cylindrical rods partially immersed in liquid, the static lateral capillary force can be estimated by

$$F(s) = 2\pi\gamma Q_1 Q_2 / L \tag{3.4}$$

where $Q_k = r_k \sin\psi_k$, k = 1,2, r_k is the radius of the rods, ψ_k is the meniscus slope angle (π/2– contact angle θ). Here $\gamma = 7.3\times10^{-2}$ N/m, and the contact angle is 50.2° as we measured from a flat Si film surface previously. The estimated static capillary force is on the order of 10^{-10} N.

3.1.5 The size characterization of the watermarks [96]

In this section we investigate in detail how the height of the nanorod array and the volume of the water droplet affect the watermark size. The samples had nanorod heights from 50, 115, 421, 649, to 890 nm as measured from SEM images. When a 2 μL water droplet made contact with the 890 nm silicon nanorod surface, it spread out quickly and the base of the water droplet reached a maximum within 3 seconds. The contact angle was measured to be about 3°. Figure 3.6 shows three snapshots of the water spreading fronts taken from the top of the contact angle system with a fast CCD camera. Upon immediate impact, a circular puddle formed on the

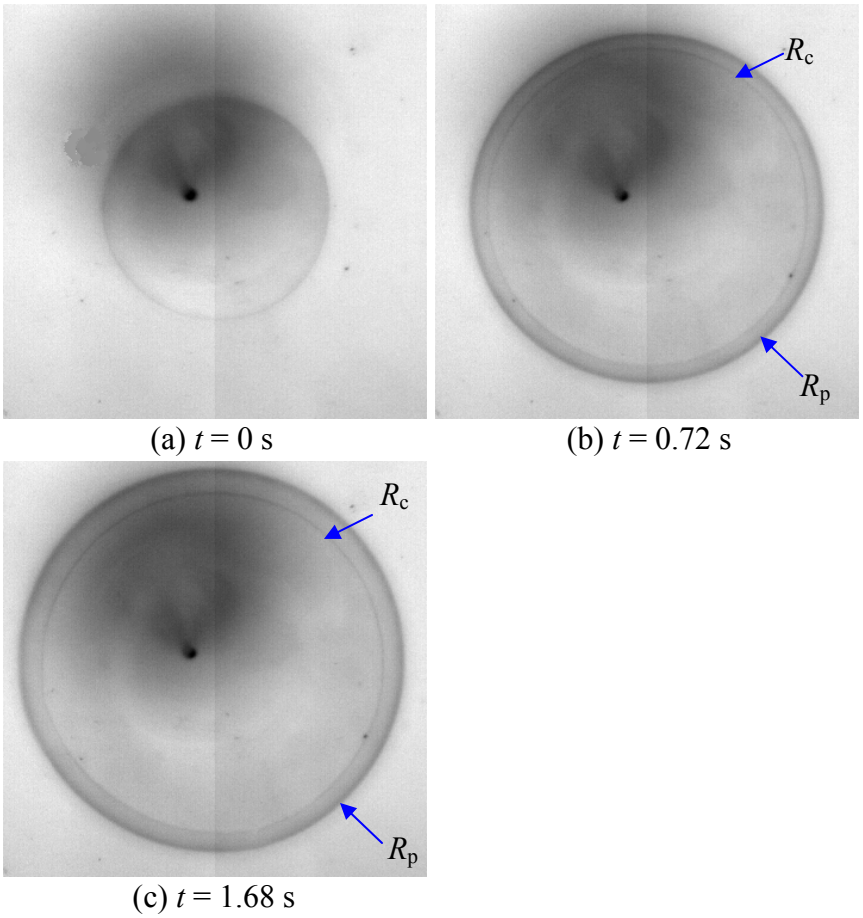

Figure 3.6. Snapshots of the water spreading fronts, taken from the top of the spreading water droplet with a CCD camera at 210 fps at (a) $t = 0$ s (arbitrarily determined); (b) $t = 0.72$ s, and (c) $t = 1.68$ s, respectively. R_c and R_p represent the radii of the contact line and precursor film, respectively.

nanostructured surface (Fig. 3.6(a), $t = 0$ s). The circular boundary of the puddle is defined as the contact line, or the three-phase line of the water droplet, and the radius of the contact line is denoted as R_c. After less than 0.2 s, in addition to the spreading of the contact line, a small dim ring appeared in front of the contact line. The size of the ring, as well as that of the contact line, started to grow with time. This ring is due to water imbibed into the nanorod structure, and we name it as the precursor film, with its radius denoted as R_p (Fig. 2(b), $t = 0.72$s). When the radius of the contact line spread further, the width of the precursor film also kept growing (Fig. 3.6(c), $t = 1.68$ s). In about 2 s, the radius of the contact line R_c reached a maximum, while the width of

the precursor rim kept increasing for another 2 s. Both the precursor front and the contact line remained at the maximum positions for about 2 minutes, then both R_c and R_p receded slowly. Occasionally, the contact line would stop for a few seconds before withdrawing further due to hysteresis. In about 3 minutes, the water droplet totally evaporated, and an orange disk-like watermark was left on the surface, as shown previously. If one examines the watermark carefully, one can see the existence of several rings. Those rings are due to the contact line pinning during the receding process (drying).

The watermark is the result of nanorod bundling. Since the precursor rim has a larger radius than that of the contact line. The maximum radius of the watermark is determined by the precursor rim rather than the contact line. This phenomenon is very similar to the rim formation during liquid droplet spreading on a rough surface [97,98], or to the stain left after liquid droplet spreading on a porous substrate [99-104]. For both rough surface spreading and porous structure spreading, the capillary flow through a groove or a channel plays a very important role. Conceptually, the nanorod array surface can be treated as a rough surface with high aspect ratio pillars, or as a three dimensional porous network with connected open capillaries. According to the classical theory derived by Washburn [11], the driving force for the spreading is due to the capillary pressure,

$$P_c = \frac{2\gamma}{r_e}\cos(\theta_e + \varphi), \tag{3.5}$$

where θ_e is the contact angle between the liquid and the surface of the nanorod, φ is the nanorod inclination angle, and r_e is the effective radius of the capillaries. Thus, the effective capillary radius r_e plays a crucial role for the dynamics of the precursor rim. For the nanorod array, the opening between two nanorods is equivalent to the cross-section of a capillary tube, therefore the effective capillary radius r_e is determined by the average height of the nanorods and the average

gap between the nanorods. In order to understand how the height of the nanorod affects the formation of the precursor rim, water drops with volumes of 0.1 μL to 4 μL were used to form

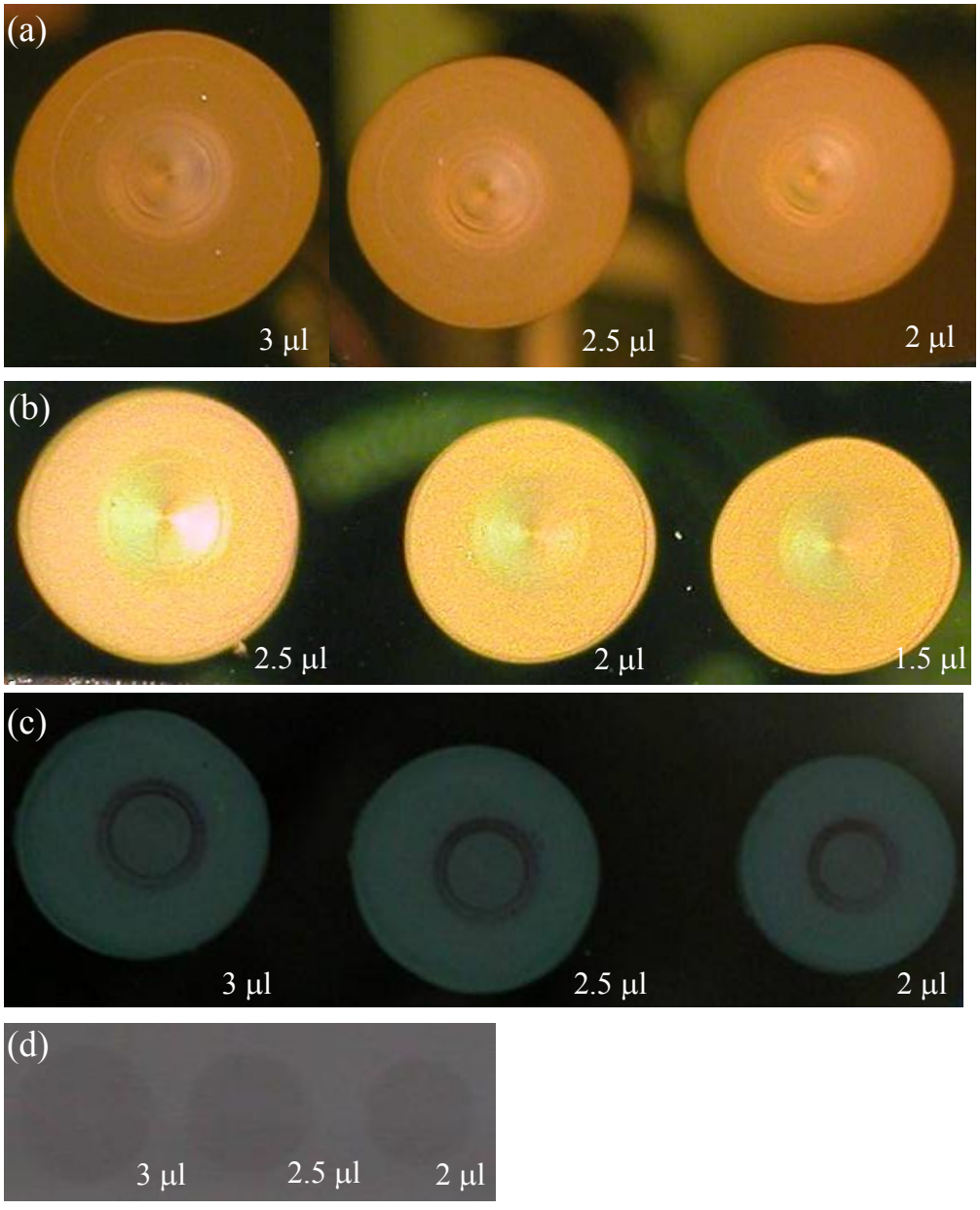

Figure 3.7. Optical micrographs of the watermarks formed on silicon nanorod substrates with heights of (a) 890 nm, (b) 649 nm, (c) 241 nm, and (d) 115 nm, respectively, and with water droplet volumes selected from 1.5 to 4 μl. The volume decreases from left to right for each sample.

watermarks on nanorod substrates with rod heights of 50 nm, 115 nm, 421 nm, 649 nm, and 890 nm, respectively. Figure 3.7 shows some representative optical images of the watermarks formed on Si nanorod surfaces having heights of 890 nm, 649 nm, 421 nm, and 115 nm, respectively.There are several distinct features: (1) the color of the as-deposited nanorod samples differs from each other. For nanorod heights of 890 nm, 649 nm, 421 nm, and 115 nm, the colors are yellow-green, green, dark-green and grey, respectively; (2) the colors of the watermark also differ from those of the as-deposited surfaces and watermarks with different nanorod height. They are orange, yellow, light blue and dark grey at decreasing nanorod height, respectively. These colors indicate there are characteristic light wavelengths which are reflected for different samples due to the film thickness and specific effective dielectric constant; (3) for the samples with rod heights of 890 nm, 649 nm and 421 nm, there exists a shining circular inner-disk in the center, which suggests that nanorod structures formed in the center are different from those outside the inner-disk, as pointed out in the previous section. However, on the Si nanorod sample with 50 nm rod height, the watermark could not be detected by naked eye. After coating with a thin layer of Chromium film (~ 10 nm), dim dark disks appeared on positions where the water drops were placed, meaning that watermark also formed on very short silicon nanorod substrates. The chromium coating simply enhanced the contrast of optical imaging; (4) the larger the volume of the water droplet, the larger the watermark size. This is true for all the samples with different rod heights.

The diameter of the watermark, $2R_p^{\max}$, measured by the measurescope, is plotted in Fig. 3.8 as a function of the nanorod height for different water droplet volume Ω. The diameter of the watermark increases almost monotonically with the nanorod height. More specifically, for nanorod height increasing from 115 nm to 421 nm, the watermark size almost doubles for all

water droplet volumes. But the changes in watermark sizes for the heights of 421 nm, 649 nm, and 890 nm, are very small. This trend is similar to the apparent contact angle change as a function of the nanorod height observed in Chapter 2. In Chapter 2, the apparent contact angle

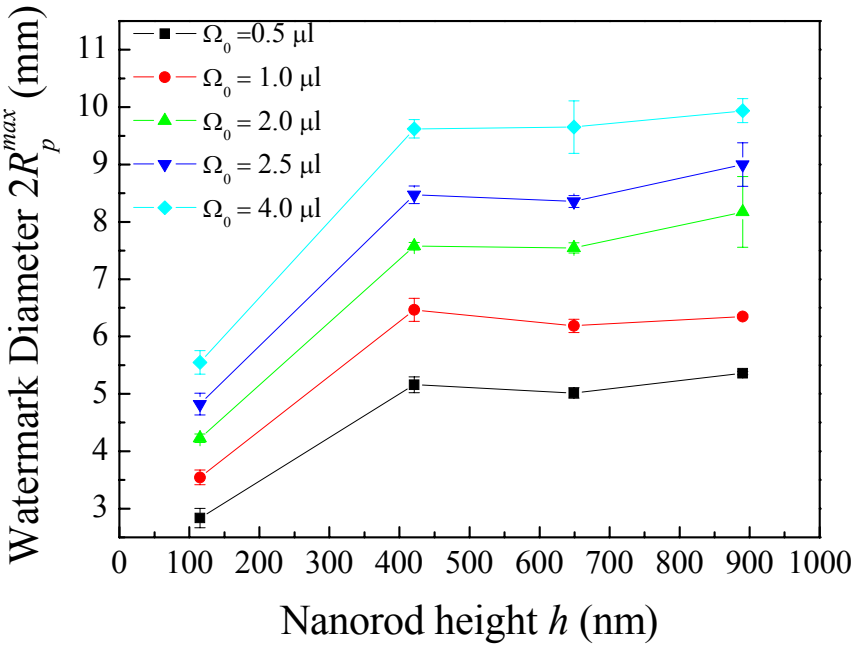

Figure 3.8. The plot of the watermark size as a function of the nanorod height for different water volumes. For different volumes, the $2R_p^{\max} \sim h$ relationship follows almost the same trend.

decreased almost exponentially for increasing nanorod height at h < 150 nm. While for taller nanorods, the contact angle reached a constant value. When the diameter of the watermark is plotted as a function of water volumes in log-log scale, as shown in Fig. 3.9(a), a power law relationship is observed,

$$R_p^{\max} \propto \Omega^{\beta}, \tag{3.6}$$

where β is the scaling exponent. It is found that β = 0.283 ± 0.002, 0.306 ± 0.010, 0.310 ± 0.008 and 0.322 ± 0.018 for samples with rod height of 890 nm, 649 nm, 421 nm and 115 nm,

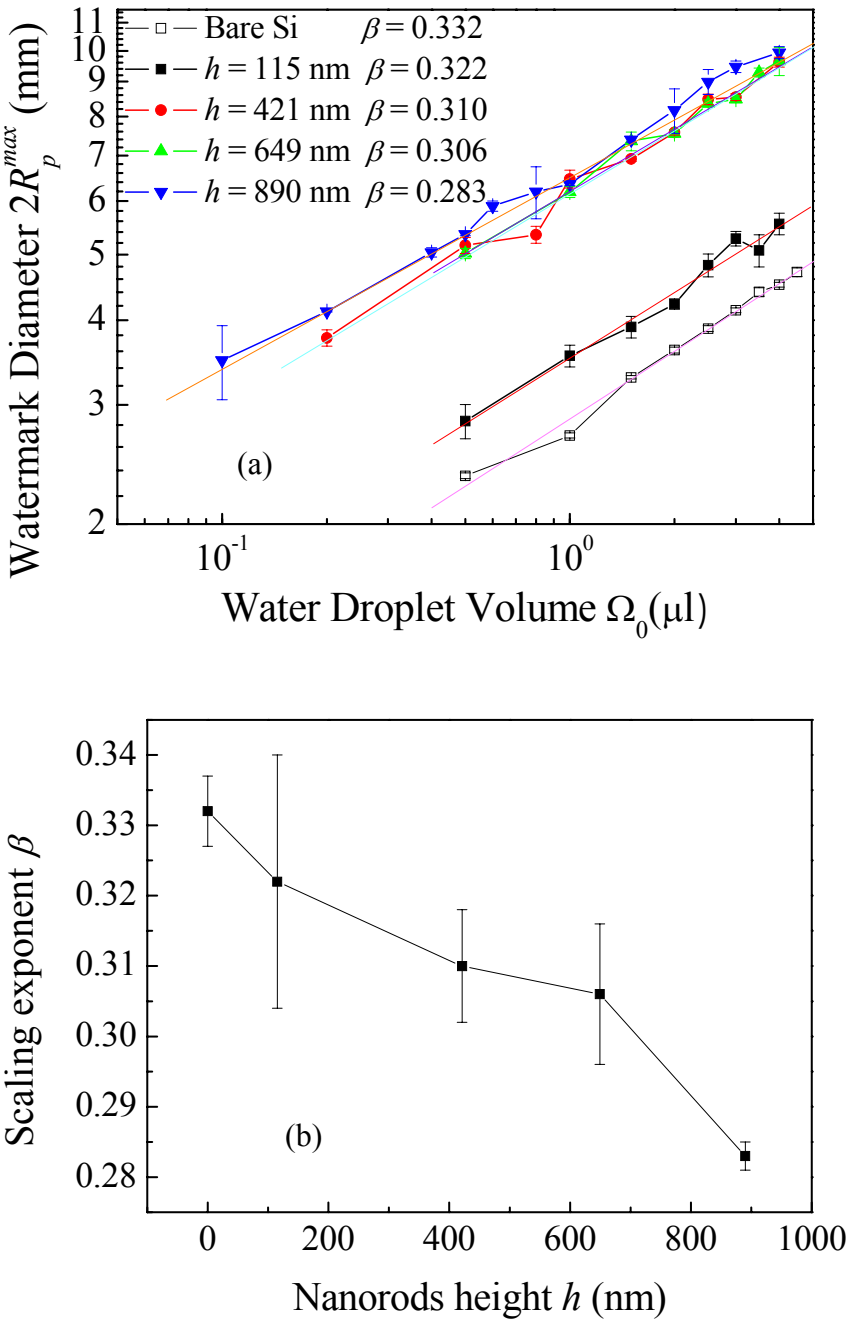

Figure 3.9. (a) Log-log plot of the watermark diameter versus water droplet volume on a 500 nm thick Si film and Si nanorod array substrates with height of 890 nm, 649 nm, 241 nm and 115 nm, respectively. A power law $2R_p^{\max} \propto \Omega_0^{\beta}$ has been observed; (b) the plot of power law exponent β as a function of the nanorod height h. The exponent β decreases monotonically with increasing nanorod height.

respectively. All the values of the exponent β are in the vicinity of 1/3. Moreover, with the increment of nanorod height, β decreases slightly as shown in Fig. 3.9(b). For reference, a 500 nm thin amorphous Si (a-Si) film on Si substrate was fabricated under the same deposition conditions without substrate tilting. Water droplets with different volumes were dispensed onto the reference sample. The side views of the droplets were taken when the drops stabilized, and the diameter of the drop base is also proportional to the maximum lateral dimension of the drop in the image. The plot of the drop base diameter versus volume in Fig. 3.9(a) gives $\beta = 0.332 \pm 0.005$, which is larger than all the β values obtained for nanorod samples.

Since the volume of the water droplet is relatively small, the shape of the water droplet on the *a*-Si film can be treated as a spherical cap, and the volume of the water drop can be expressed as

$$\Omega = \frac{1}{6}\pi H(3R_c^{\,2} + H^2), \tag{3.7}$$

where H is the height of the spherical cap. For a spherical cap,

$$H = R_c \cdot \tan(\frac{\theta}{2}), \tag{3.8}$$

where θ is the contact angle. Substituting Eq. 3.8 into Eq. 3.7, one obtains,

$$\Omega = \frac{\pi R_c^{\,3}}{6}(3 + \tan^2\frac{\theta}{2})\tan\frac{\theta}{2}. \tag{3.9}$$

Therefore,

$$R_c \propto \Omega^{1/3}. \tag{3.10}$$

This result agrees very well with the scaling exponent for the droplet on a flat surface. However, the derivation of Eq. 3.10 is based on the assumption that there is no liquid evaporated during the spreading. However, from the dynamic observation, as shown in Fig. 3.6, the watermark

formation process can be viewed as the competition of spreading with evaporation, as well as spreading inside the nanorod arrays. In order to simplify the problem, we assume that there are two connected processes, the evaporation during the spreading on a smooth surface, and the water invasion into nanorod array. The volume of water on the nanorod array contains two parts, the water above the nanorods (Ω), and the water imbibed into the nanorod channels (Ω_p). The assumption of a smooth surface (or a heterogeneous smooth surface) is based on the experimental observation of the precursor film spreading ahead of the contact line. This precursor layer effectively "lubricates" the surface by filling into the nanorod channels. In fact, the spreading law on such a surface agreed with that on a smooth surface (as will be explained in Chapter 4). Usually, $\Omega_p << \Omega$, and the volume Ω_p inside the channel can be neglected. For example, a 3 μL water droplet on the 890 nm silicon nanorods, which has the largest watermark size, will have a maximum watermark diameter of about 10 mm. Thus,

$$\Omega_p = \pi R_p^{\max 2} h * (1 - f). \tag{3.11}$$

where $R_p^{\max}$ is the maximum radius of the watermark, h is the height of the nanorods, and f is the nanorods coverage. Thus, Ω_p is found to be about 3.7×10^{-2} μL. This is much less than 3 μL. This volume could be important for later stage of evaporation. Since the water contact angle on nanorods is very small, Eq. 3.9 can be simplified,

$$\Omega = \frac{\pi}{4} R_c^3 \theta . \tag{3.12}$$

The time derivative of Ω gives,

$$\frac{d\Omega}{dt} = \frac{3}{4}\pi R_c^2 \theta \frac{dR_c}{dt} + \frac{\pi}{4} R_c^3 \frac{d\theta}{dt}. \tag{3.13}$$

The change of the water volume should equal to the volume evaporated. For simplicity, we assume that the water evaporates at a constant rate on the surface,

$$\frac{d\Omega}{dt} = -J\pi R_c^2 . \tag{3.14}$$

where $J = \frac{dH}{dt}$ is the evaporation rate and πR_c^2 is the approximate total surface area of the water droplet with a spherical cap shape. Substituting Eq. 3.14 into Eq. 3.13,

$$R_c \frac{d\theta}{dt} + 3\theta \frac{dR_c}{dt} = -4J . \tag{3.15}$$

In addition, for a water droplet with small contact angle, with its size decreasing due to evaporation, the change of the base radius R_c is simply related to the change of the height H of the droplet by,

$$dH = \frac{\theta}{2} dR_c . \tag{3.16}$$

Equation 3.16 can be directly derived from Eq. 3.8. Thus,

$$\frac{dR_c}{dt} = -\frac{2J}{\theta} . \tag{3.17}$$

For a non-volatile liquid, the droplet spreading on a smooth surface is governed by the capillary force [105],

$$\frac{dR_c}{dt} = \frac{V^*}{3ln}(\cos\theta_e - \cos\theta)\theta , \tag{3.18}$$

where $V^* \equiv \gamma/\mu$, μ is the viscosity of the liquid, and ln is a dimensionless coefficient. For water, V^* = 70 m/s, ln = 20, and θ_e is the equilibrium contact angle, which is very small in our case, and Eq. 3.18 can be simplified to

$$\frac{dR_c}{dt} = \frac{V^*}{6ln}\theta^3 . \tag{3.19}$$

Combining Eq. 3.17 with Eq. 3.19, the change of R_c due to the competition of spreading and evaporation can be written as,

$$\frac{dR_c}{dt} = \frac{V^*}{6ln}\theta^3 - \frac{2J}{\theta}. \tag{3.20}$$

Equations 3.15 and 3.20 are the two basic equations we use to solve the dynamics of R_c. When R_c reaches the maximum, $\frac{dR_c}{dt} = 0$, corresponding to a contact angle θ_c^* at $R_c^{\max}$, Eq. 3.20 gives,

$$\theta_c^* = \sqrt[4]{\frac{12ln \cdot J}{V^*}}. \tag{3.21}$$

The angle θ_c^* is the apparent contact angle that was measured in Chapter 2. Combining Eq. 3.15 with Eq. 3.20 yields,

$$\frac{dR_c}{R_c} = \frac{\frac{V^*}{6ln}\theta^3 - \frac{2J}{\theta}}{2J - \frac{V^*\theta^4}{2ln}} d\theta. \tag{3.22}$$

Equation 3.22 can be solved analytically, and the expression for $R_c^{\max}$ is,

$$R_c^{\max} = \sqrt[3]{\frac{4}{\pi}}\Omega_0^{\frac{1}{3}}\left(\frac{2}{3 - \theta_c^{*4}/\theta_0^{\,4}}\right)^{\frac{1}{6}}\theta_c^{*-\frac{1}{3}} \approx \left(\frac{2}{3}\right)^{\frac{1}{6}}\sqrt[3]{\frac{4}{\pi}}\Omega_0^{\frac{1}{3}}\theta_c^{*-\frac{1}{3}}, \tag{3.23}$$

where $\Omega_0 = \frac{\pi}{4}R_0^3\theta_0$ is the initial volume of the water droplet. This approximation is carried out under the condition that $\theta_c^* << \theta_0$. Equation 3.23 shows that the maximum radius of the contact line scales with both the drop volume Ω_0 and the apparent contact angle θ_c^*. The power law relationship between the maximum drop size and drop volume partly explains why all the scaling exponents β in Fig. 3.9 are in the vicinity of 1/3, and the deviations from 1/3, observed for nanorods with different heights, are due to the capillary spreading inside the nanochannel. From

the dynamic spreading measurement, we have confirmed that the precursor front obeyed the general Washburn relationship (Fig. 3.6) [11,99-104],

$$\delta = R_p - R_c = (\frac{r_e \gamma \cos\theta_e}{2\mu})^{1/2} t^{1/2}, \tag{3.24}$$

i.e.,

$$R_p = R_c + \delta. \tag{3.25}$$

When the radius of the precursor film reaches a maximum, $\frac{dR_p}{dt} = 0$,

$$\left.\frac{dR_c}{dt}\right|_{t=t_p} = -\frac{1}{2}(\frac{r_e \gamma \cos\theta}{2\mu})^{1/2} t_p^{-1/2}, \tag{3.26}$$

where t_p is the time when R_p reaches the maximum. The property $\left.\frac{dR_c}{dt}\right|_{t=t_p} < 0$ indicates that the contact line is in the receding process, i.e., when R_c is receding, R_p can reach the maximum. Thus, R_p takes longer to reach the maximum compared to that of R_c. This is consistent with our experimental observation described above. Inserting Eq. 3.26 into Eq. 3.20 and assuming $\theta_p^* << 1$, one has

$$\theta_p^* \approx 4J(\frac{2\mu}{r_e \gamma \cos\theta_e})^{1/2} t_p^{1/2}, \tag{3.27}$$

and

$$\begin{aligned} R_c^p &= R_c^{\max}(\frac{2\theta_p^{*4}}{3\theta_c^{*4} - \theta_p^{*4}})^{1/6} \frac{\theta_c^*}{\theta_p^*} \approx (\frac{2}{3})^{\frac{1}{3}} \sqrt[3]{\frac{4}{\pi}} \Omega_0^{\frac{1}{3}} \theta_p^{*-1/3} \\ &= (\frac{2}{3})^{\frac{1}{3}} \sqrt[3]{\frac{4}{\pi}} \Omega_0^{\frac{1}{3}} (\frac{1}{4J})^{1/3} (\frac{r_e \gamma \cos\theta_e}{2\mu})^{1/6} t_p^{1/6} \end{aligned}. \tag{3.28}$$

where R_c^p and θ_p^* are the radius of the contact line and the contact angle at time t_p. Thus,

$$R_p^{\max} \approx (\frac{2}{3})^{\frac{1}{3}} \sqrt[3]{\frac{4}{\pi}} \Omega_0^{\frac{1}{3}} (\frac{1}{4J})^{1/3} (\frac{r_e \gamma \cos\theta_e}{2\mu})^{1/6} t_p^{1/6} + (\frac{r_e \gamma \cos\theta_e}{2\mu})^{1/2} t_p^{1/2}. \quad (3.29)$$

Equation 3.29 shows that the capillary flow inside the nanorod array modifies the maximum radius for the precursor rim, leading to two major qualitative conclusions. First, the effective capillary radius, $r_e \propto h^{1/2}$, therefore, Equation 3.29 shows that $R_p^{\max}$ increases monotonically with the nanorod height, which is qualitatively consistent with the results in Fig. 3.8. However, as will be discussed later, the relationship $r_e \propto h^{1/2}$ will not hold for very long nanorods due to the bending and clustering of the nanorods, and the behavior of the watermark on the longer nanorod will be affected. Second, since the dynamic behavior of the contact line is expected to be the same for different nanorod heights, according to Eqs. 3.15 and 3.20, in order to satisfy Eq. 3.26, taller nanorods require a longer time t_p to reach the maximum. Thus, the taller the nanorods are, the larger the $R_p^{\max}$ will be. For the droplet volume dependence, roughly the maximum radius of the watermark (precursor film) obeys the $\Omega_0^{1/3}$ law, except that a constant term appears in Eq. 3.29. This extra term is closely dependent on the nanorod height as discussed above. With the increment of the rod height, the contribution of this constant term becomes more and more important, since it will increase with a much faster rate with respect to the rod height, as compared to the volume dependent term. Thus, with the increase of the rod height, the $R_p^{\max} \sim \Omega_0$ relationship will deviate further from the $\Omega_0^{1/3}$ law. Eventually, Equation 3.29 predicts that the exponent β will decrease with the nanorod height, which qualitatively agrees with the results in Fig. 3.9. It should be noted that, although the pinning of the contact line was observed during the liquid drop receding on the silicon nanorod surface, the above model does not include any pinning mechanism.

3.1.6 The Morphological Characterization of the Watermarks [96]

In this section, we give a detailed SEM characterization and comparison of watermarks formed at nanorod surfaces with different rod height. Figure 3.10 shows the representative top-view SEM images taken at three different regions of the watermark on nanorod sample with nanorod heights of 115 nm, 649 nm and 890 nm, respectively. The volume of the water droplet used to form those watermarks is fixed to $\Omega = 2.5$ μL. Three general characteristics are observed: (1) for the same watermark, the size of the bundled nanorod clusters decreases from the center of

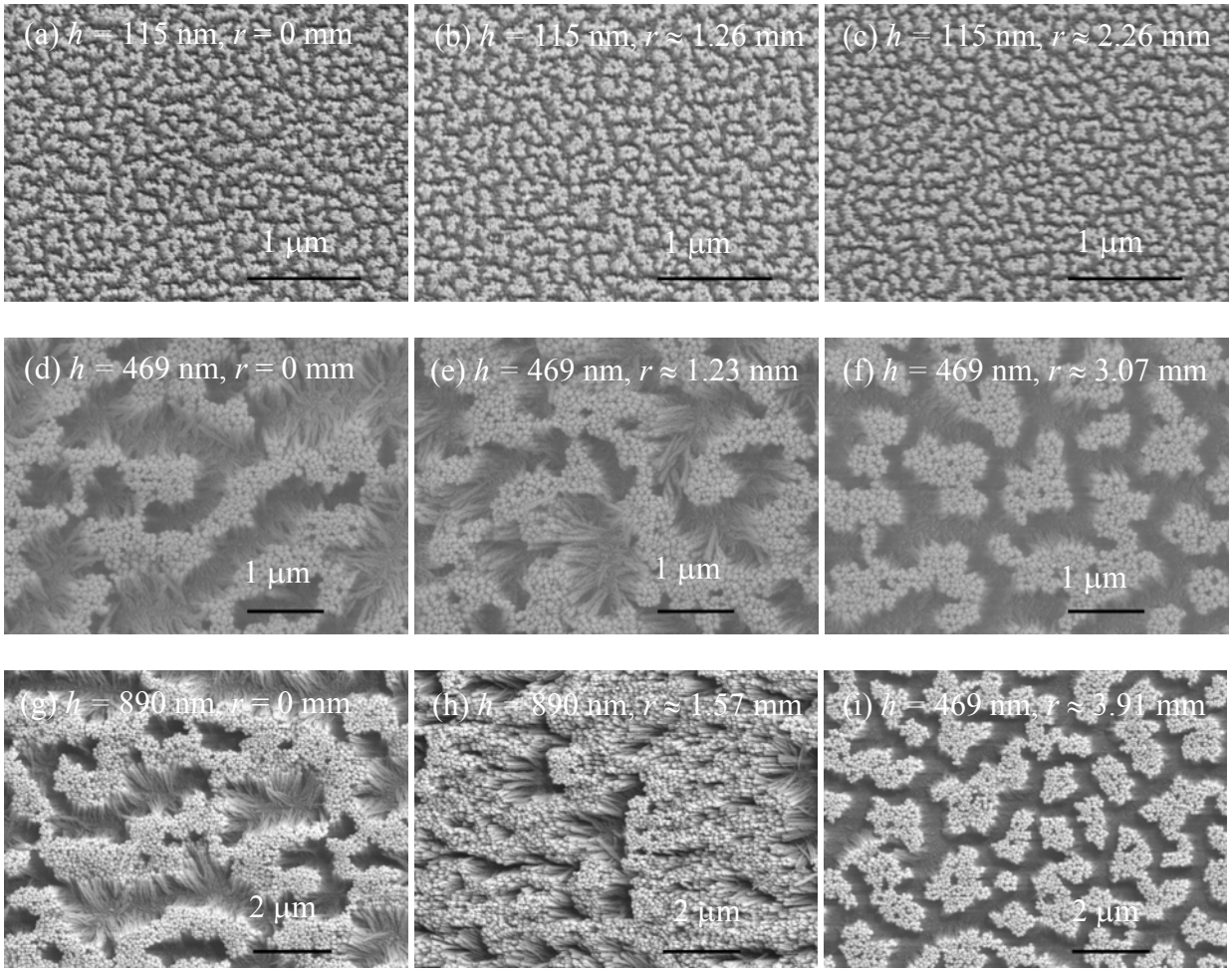

Figure 3.10. The SEM top-view images of the bundled nanorod clusters formed from the center to the edge of the watermark for different substrates. (a) – (c) are from the watermark on h = 115 nm nanorod arrays; (d) – (f) are from the watermark on h = 649 nm nanorod arrays; and (g) – (i) are from the watermark on h = 890 nm nanorod arrays.

the watermark towards the edge of the watermark; (2) the bundled clusters are irregularly shaped. In fact, those clusters are all isolated and surrounded by water channels made by water pathways during the invasion process. These water channels are percolated through the entire observation area; (3) both the cluster size and channel size are closely dependent on the nanorod heights. In fact, they increase as nanorod height increases.

One could speculate that the morphology of the nanorod clusters will be very similar to those formed in two-dimensional percolation theory, due to the nature of the invading process. Or more specifically, the morphology of the bundled nanorod clusters can be described by the invasion percolation (IP) model [71,106]. The IP model has been proposed to model the displacement of a wetting fluid in a porous medium, by the injection of another nonwetting fluid. In the absence of viscous or gravitational forces, the displacement is controlled solely by the capillary pressure, and the invasion front separating the two fluids advances by penetrating the pore throat at the front with the largest size [71,106]. Physically, the driving force in the IP model is the capillary pressure difference between the two fluids, which is similar to that of the water penetrating the nanorod array. The differences between the conventional invasion percolation and the invasion in nanorods are (1) the two fluids in the nanorod array are water and air; and (2) the porous network becomes the openings in the randomly distributed nanorod array. Since in the present study one can only measure the static SEM images of those invaded surfaces, one can only compare the static characteristics of the cluster morphology with that of the IP model. One most important parameter of those characteristics is the fractal dimension, D_f, of the clusters. The fractal dimension, D_f, can be determined by measuring the perimeter L and area A of the fractal clusters [92],

$$L \propto A^{D_f/2}. \tag{3.30}$$

Figure 3.11(a) plots the perimeters versus their areas of the bundled clusters of the watermark on the 890 nm nanorods at r = 1.97 mm in log-log scale. From the curve fitting in Fig. 3.11(a), the value of the fractal dimension D_f at r = 1.97 mm is obtained to be D_f= 1.8 ± 0.2. This result is consistent with the fractal dimension of the IP model [107,108]. In addition, the fractal dimension across the entire watermark has been calculated from the *L-A* plots, and in Fig. 3.11(b) the fractal dimension D_f is plotted as a function of the distance r from the center of the watermark on the 890 nm nanorod surface. From the near center to the far edge, the fractal dimension almost remains as a constant, $D_f \sim 1.8$. This result shows that the pattern or cluster morphology across

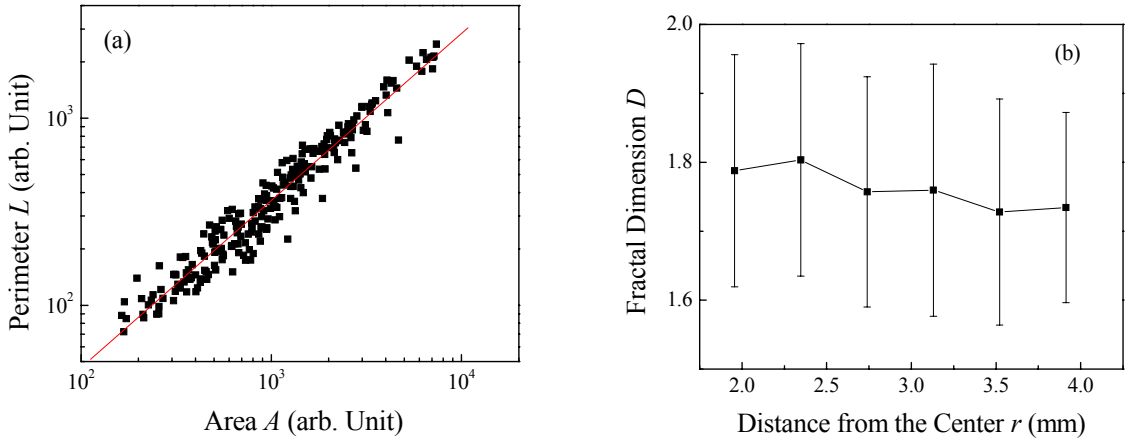

Figure 3.11. Determination of the fractal dimension of the watermark morphology using the perimeter-area plot. (a) A representative plot of perimeter L versus area A of the bundled nanorod clusters in the log-log scale. The plot was derived from an SEM image at a distance r = 2.35 mm from the watermark center, with the rod height of 890 nm, and a water droplet volume of 2.5 μL. The linear fitting gives a slope of 0.89. (b) The plot of the fractal dimension D_f as a function of the distance r from the center, of the same watermark.

the watermark is the same, which implies that the invasion percolation could be the main mechanism for the pattern formation. The invariance of D_f across the watermark is due to the universal property of the invasion percolation process.

Another independent way to characterize the morphology of a clustered surface is to calculate the two dimensional power spectrum of the surface. However, the SEM top-view images not only show the lateral characteristics of the clusters, such as size, shape, distance, but also contain their vertical characteristics, such as bending and height. Thus, the power spectrum obtained from a direct Fourier transformation of the original SEM image will mix the height information with the cluster information, and will make the interpretation more complicated. In order to obtain only the cluster information, we have to level-set the image as a black and white image. An example is shown in Fig. 3.12. Figure 3.12(a) is the original SEM image taken from the center of a watermark on 890 nm tall nanorod surface, and Fig. 3.12(b) shows the black-and-white image of Fig. 3.12(a) after the level-setting. This image only gives the lateral distribution and shape of the clusters. According to Amar et al, at large k, the power spectrum for a clustered surface obeys a power law [93]:

$$P(k) \sim k^{-D_f} . \tag{3.31}$$

Usually a circular average of the two-dimensional power spectrum is used to obtain the fractal dimension, so the circular averaged power spectra of Fig. 3.12(a) and (b) are both calculated and plotted in log-log scale in Fig. 3.12(c). Both power spectra have a maximum at $k_c \approx 0.546\ \mu m^{-1}$. However, at $k > k_c$, both spectra have a power law tail, and the exponents are very different. For the power spectrum obtained from the original SEM image (Fig. 3.12(a)) the exponent is -2.39 ± 0.02, while the exponent obtained from the level-setting image (Fig. 3.12(b)) is -1.81 ± 0.01. The large exponent obtained from the original SEM image is the result of the mixing of the height information (grey scale) with the lateral information in the power spectrum, or in other words, one has to treat the surface as a true topographic surface. However, the exponent (the fractal

dimension) obtained from level-setting image (two-level surface) is in agreement with those obtained by the perimeter-area method described above.

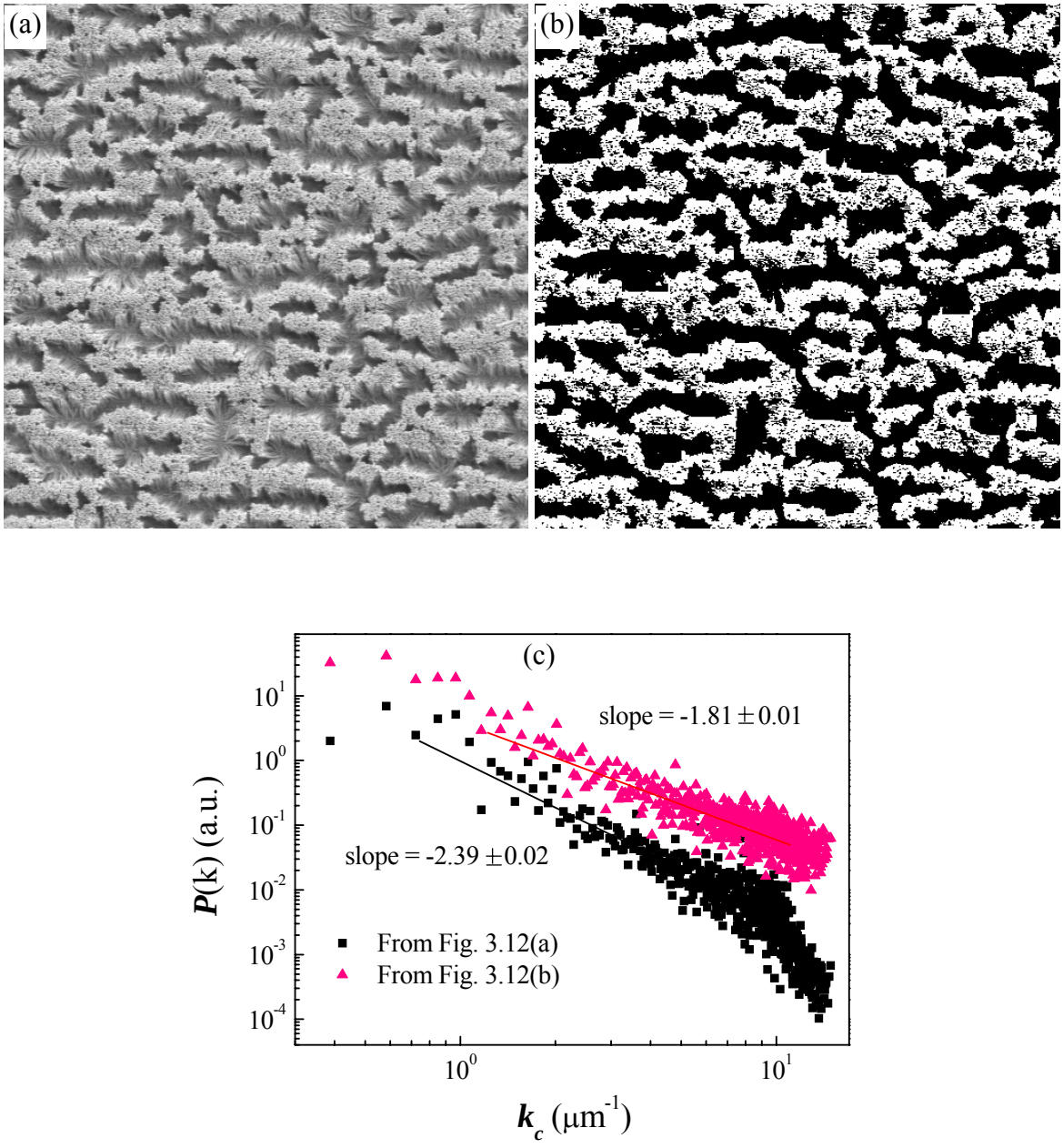

Figure 3.12. The use of power spectrum to determine the fractal dimension and the cluster size of the nanorod bundles: (a) the original SEM image at the center (r = 0 mm) of the watermark formed on the 890 nm Si nanorod array with a water droplet volume of 2.5 μL; (b) the level-setting image of (a). The white islands represent the bundled nanorod clusters, and the black channels are the water pathway. (c) The circular averaged power spectra of (a) and (b) plotted in log-log scale.

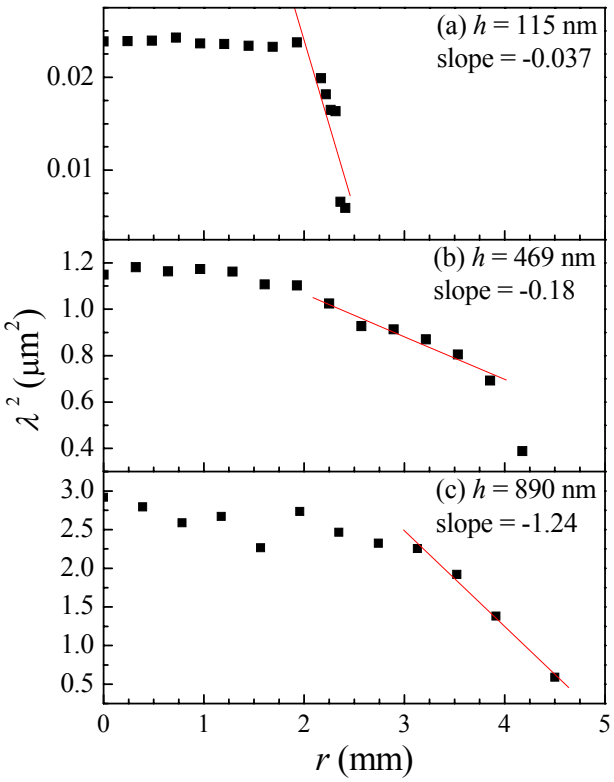

Figure 3.13. The plot of the cluster area λ^2 versus the distance r from the center of the watermark for nanorod heights of 115 nm, 649 nm, and 890 nm, respectively. Near the center of the watermark, the area λ^2 almost remains constant, while at the edge of the watermarks, the area λ^2 decreases almost linearly with r.

Besides the fractal dimension D_f of the clusters, the diameter or the area of the cluster is another important parameter to characterize the cluster morphology. This parameter can be derived from the power spectrum as well. For all the level-setting SEM images, either from different locations of the same watermark, or from watermarks on different nanorod surface, all the two dimensional power spectra have the same ring-like structure, indicating that there is a characteristic length scale on the surface. The center of the power spectrum ring k_c is directly related to the average cluster-cluster distance λ on the surface by $k_c = 1/\lambda$. Since the coverage of the nanorod f on the surface remains unchanged both before and after water invasion, and the

clusters are closely packed nanorods, the average diameter of the clusters is proportional to the average separation λ of the clusters, i.e., $\lambda = 1/k_c$ represents the average diameter of a cluster, and λ^2 is proportional to the average area of a cluster. Figure 3.13 plots the λ^2 obtained from k_c versus the distance r from the center of the watermark for three different nanorod surfaces with heights of 115 nm, 649 nm, and 890 nm, respectively. For all three different rod heights, the λ^2 remains almost constant from the center of the watermark to a relative large distance r from the center, and then it starts to decrease. This is consistent with the observation in Fig. 3.10. The λ^2 values near the center of the watermark are 0.024 μm^2, 1.17 μm^2, and 2.56 μm^2, for rod height of 115 nm, 649 nm, and 890 nm, respectively, i.e., the cluster size increases monotonically with the rod height. At the edge of the watermark, λ^2 decreases almost linearly with r, and the rate of decrease (slope) obtained from the linear fitting is -0.037 μm^2/mm, -0.18 μm^2/mm, and -1.24 μm^2/mm for rod height of 115 nm, 649 nm, and 890 nm, respectively. That is, the absolute value of the slope increases with the rod height.

3.2 Understanding the nanocarpet effect

In order to understand why both the cluster size and the cluster size decreasing rate at the edge of a watermark depend strongly on the nanorod height, we first investigate how the nanorod bundle is formed and the factors that affect its size.

3.2.1 Cluster size in the nanocarpet effect [109]

Very recently, Journet et al. used the balance between the elastic energy of a bent nanorod and the capillary energy to estimate the diameter of the bundled nanorods, $\lambda \sim \sqrt{\frac{\gamma h^4}{ED^3}}$,

where E is the Young modulus of the nanorods [88]. The expression γDh of the capillary interaction energy in their estimation is the interfacial energy when the liquid totally covers a nanorod. No further detail has been given for this expression. It is clear that the driving force for the bundling should be the capillary interaction due to the formation of meniscus on the adjacent nanorods. Thus, mechanical bending of the nanorods acts as a counter force to balance the capillary force caused by the meniscus. The bundling of the nanorods results from the balance between the capillary interaction and mechanical bending of the nanorods. In addition, all previous experimental investigations showed that the bundled clusters were closely packed. Therefore, one can simply treat the bundled cluster as a circular shape, and the nanorods are arranged on the circumferences with radius of D, $2D$, $3D$, …, where D is the diameter of the

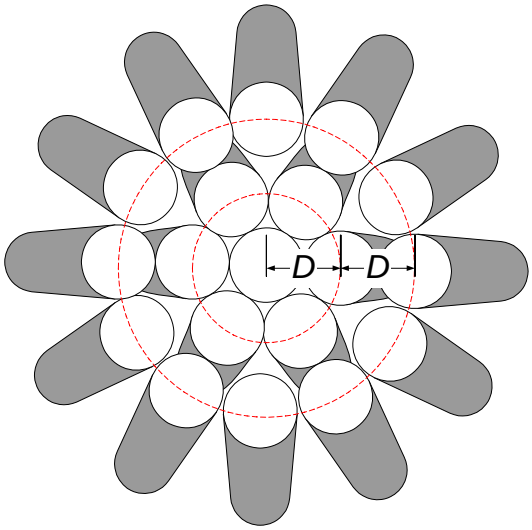

(a) Top view

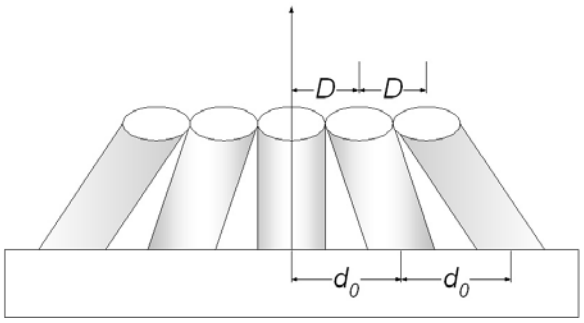

(b) Cross-sectional view

Figure 3.14. A geometric model of a cluster of bundled nanorods: (a) top view: the rod in the center is the nucleation seed; the nanorods bend towards the center are closely arranged on circumferences with radius of D, $2D$, $3D$, ….. (b) cross-sectional view: the bottom of the rods is fixed on the substrate with a separation of d_0 and the top of the cluster is almost closely attached to each other.

nanorod, as shown in Fig. 3.14(a). The rod in the center is standing straight, then the nanorods in first circumference bend slightly, and the nanorods in second circumference bend slightly more, and so on (Fig. 3.14). Before the bending of the nanorod, the separation between the nanorods is d_0. Assuming the average size of the cluster is N,

$$N \approx 1 + \frac{2\pi D}{D} + \frac{4\pi D}{D} + \cdots + \frac{2m\pi D}{D} = 1 + m(m+1)\pi\,, \tag{3.32}$$

where m is the mth ring filled by the nanorods. The mechanical bending energy ΔE_b associated with each bent nanorod is [110],

$$\Delta E_b \approx \frac{\pi E D^4 \Delta y^2}{16 h^3}, \tag{3.33}$$

where Δy is the lateral displacement of the nanorod due to the bending. For a cluster depicted in Fig. 3.14, the bending of nanorods in different circumferences has a different lateral displacement,

In the first circumference, $\Delta y_1 = d_0 - D$,

In the second circumference, $\Delta y_2 = 2(d_0 - D)$,

……,

In the mth circumference, $\Delta y_m = m(d_0 - D)$.

Therefore, the total mechanical energy E_m stored in one of the bundled cluster is

$$E_m = \sum_{n=1}^{m} \frac{\pi E D^4}{16 h^3} [n(d_0 - D)]^2 \cdot 2n\pi = \frac{\pi^2 E D^4 (d_0 - D)^2}{8 h^3} [\frac{1}{2} m(m+1)]^2 . \tag{3.34}$$

From Eq. 3.32, the total mechanical energy E_m is a function of the cluster size N,

$$E_m = \frac{E D^4 (d_0 - D)^2}{32 h^3} (N-1)^2 . \tag{3.35}$$

Furthermore, the capillary interaction between two adjacent nanorods due to the meniscus has been solved by Kralchevsky et al [95]. Two identical rods have a capillary interaction energy ΔE_c,

$$\Delta E_c = \frac{\pi}{2}\gamma D^2 \cos^2\theta \ln(\gamma_e qs), \tag{3.36}$$

where γ_e = 1.781072418…, is called the Euler-Masceroni number, and $q^2 = \Delta\rho g/\gamma$, characterizing the capillary length, in which $\Delta\rho$ is the liquid density difference around the two rods. The quantity $2s$ represents the separation of the meniscus of the two rods. In general, $0 < \gamma_e qs << 1$, thus $\ln(\gamma_e qs) < 0$. Inside a bundled cluster, one can treat the average separation between the nanorods as a constant, therefore the capillary interaction between the nearest neighboring nanorods can be assumed as a constant. In addition, the cluster structure proposed in Fig. 3.14 is very close to a closed-pack structure, and one unit cell possesses the capillary interaction energy of $\frac{5}{4}\Delta E_c$. Therefore the total capillary energy E_c in a bundled cluster is

$$E_c = \frac{5\pi}{8} N\gamma D^2 \cos^2\theta \ln(\gamma_e qs). \tag{3.37}$$

Therefore, during the clustering process, the total energy gained in the cluster is

$$E_t = E_m + E_c = \frac{ED^4(d_0 - D)^2}{32h^3}(N-1)^2 + \frac{5\pi}{8} N\gamma D^2 \cos^2\theta \ln(\gamma_e qs). \tag{3.38}$$

The critical cluster size is determined by the condition that gives the minimum total energy,

$$\frac{\partial E_t}{\partial N} = 0, \tag{3.39}$$

$$N - 1 = -\frac{10\pi h^3}{D^2(d_0 - D)^2}\frac{1}{E}\gamma \cos^2\theta \ln(\gamma_e qs). \tag{3.40}$$

Equation 3.40 gives the relation between the average cluster size and the physical properties of the nanorod array as well as the liquid. The size of the cluster is inversely proportional to the Young modulus of the nanorod, and is proportional to the surface tension of the liquid. More importantly, the size of the cluster is closely related to the shape and density (or aspect ratio and height) of the nanorods,

$$N - 1 \propto \frac{r^3 D\sigma}{(1-\sqrt{f})^2}, \tag{3.41}$$

where $r = h/D$ is the aspect ratio of the nanorods, $f = \frac{\pi D^2}{\pi d_0^2}$ is the coverage of nanorods on the surface, and $\sigma = \frac{1}{\pi d_0^2}$ is the density of the nanorods. For nanorods with a uniform diameter, the higher is the aspect ratio, the larger is the cluster size.

Equation 3.40 can be tested from our experiment. Silicon nanorod samples with different aspect ratios were prepared on *p*-type silicon (100) substrates using the GLAD technique. The deposition angle was 86^o and the substrate rotation speed was 0.05 rev/s. The normal film growth rate was 0.2 nm/s. To form watermarks, water drops with controlled volumes 2.5 μL were dispensed onto an as-prepared silicon nanorod surface using a contact angle measurement system at room temperature. The coverage of nanorods on the surface for different nanorod heights was close to a constant, ~ 46 – 47%. Figure 3.15 shows the representative SEM images at the center of the watermarks for nanorod arrays with h = 115 nm, 649 nm, and 890 nm, respectively. For different nanorod heights, the nanorods bent and bundled tightly together to form clusters. Three characteristics were observed: (1) the clusters of bundled nanorods were closely packed; (2) the size of the cluster was also a function of the distance from the center of the watermark. In a large area close to the center, the cluster statistically had the same average size, while at the edge of

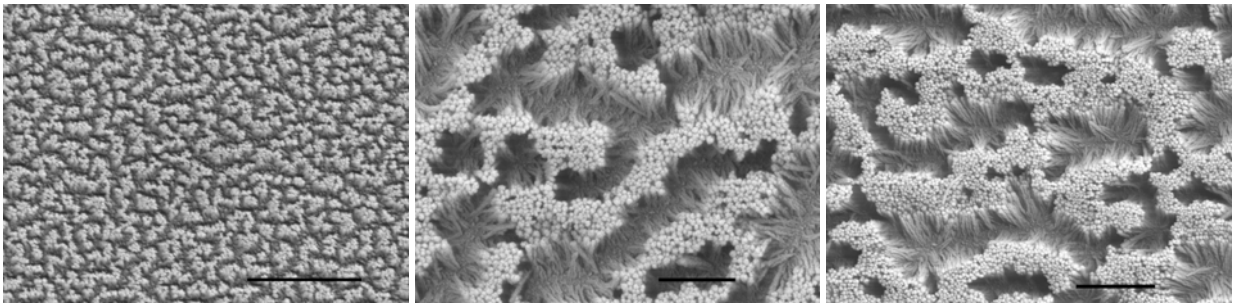

(a) h = 115 nm (b) h = 649 nm (c) h = 890 nm

Figure 3.15. SEM images of bundled nanorods near the center of the watermark from Si nanorod arrays with different heights. The water volume used to create the watermarks was 2.5 μl. The scale bar represents 1 μm.

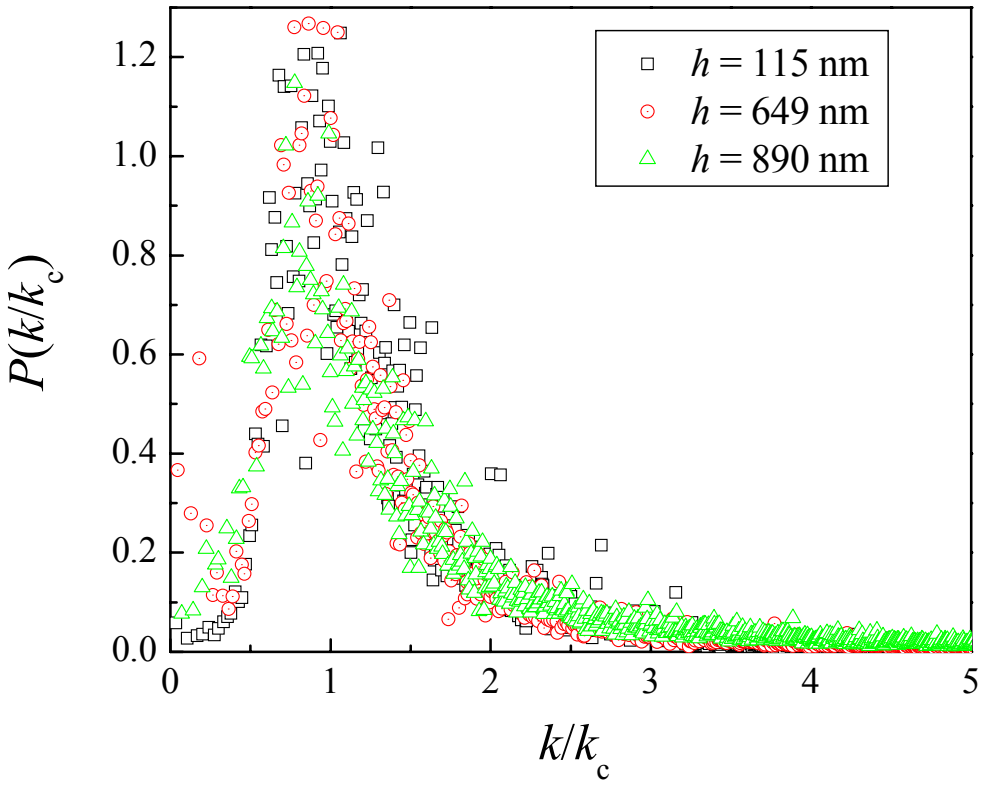

Figure 3.16. The collapse of rescaled average power spectra obtained from Fig. 3.15.

watermark the cluster size decreased with the distance; (3) the cluster size in the center increased with the nanorod height. The cluster size of the bundled nanorods can be estimated from the characteristic peak of the power spectra of the SEM images. Figure 3.16 shows the circularly

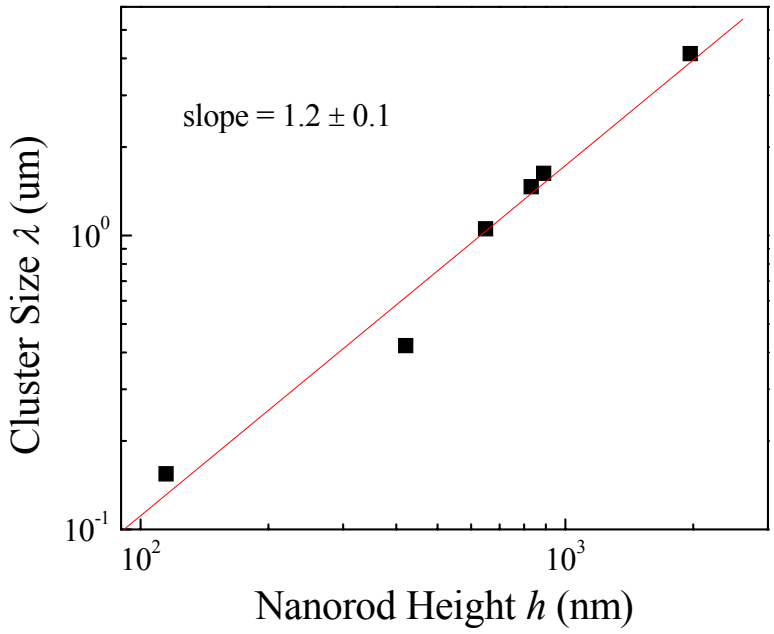

Figure 3.17. The log-log plot of the average cluster diameter λ versus nanorod length h. The scaling exponent obtained from a power-law fitting (the straight line in the plot) is 1.2 ± 0.1.

averaged power spectra of the bundled nanorods near the center of the watermarks from different samples. The vertical axis was rescaled by the total area of the power spectrum and the horizontal axis was rescaled by k_c, the characteristic peak position of each power spectrum. The power spectra from samples with different nanorod heights all collapsed together, which further suggest that the underling bundling process is the same for different samples. Figure 3.17 plots the average diameter λ (= $1/k_c$) of the cluster versus the height h of the nanorods in log-log scale. The diameter increases monotonically with the height, with $\lambda \propto h^{1.2\pm0.1}$. From Eq. 3.32 and 3.40,

one can obtain that $\lambda = 2(m+\frac{1}{2})D \approx 2\sqrt{N-1}D \propto h^{1.5}$. This prediction is qualitatively consistent with the experimental result.

3.2.2 Theoretical model for the morphology [96]

Before the water invaded into the nanostructure, as shown in Fig. 3.18(a), the total free energy for a cluster with N nanorods can be written as

$$F_i = N\pi Dh\gamma_{SV} + \frac{\sqrt{3}}{2}Nd_0^2\gamma_{SV}, \tag{3.42}$$

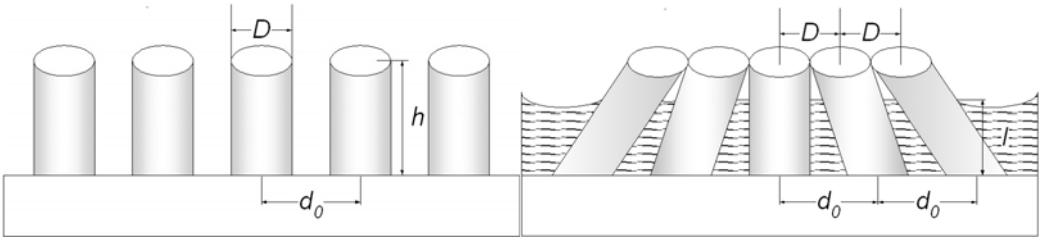

(a) Before liquid invasion (b) After partially invaded by liquid

Figure 3.18. The sketches show (a) the arrangement of the nanorods before water invasion; and (b) the bundling of the nanorods after water invasion with a general water height level l from the substrate.

where D and d_0 are the diameter and average separation of the nanorods, respectively, and γ_{SV} is the interfacial energy between the solid and the vapor (air). The $\frac{\sqrt{3}}{2}$ in the second term of Eq. 3.42 is obtained by assuming a unit cell of a close-packed lattice. When liquid invades the structure with a height of l as shown in Fig. 3.18(b) and the nanorods start to bundle together, the total free energy changes to

$$F_f = N\pi Dl\gamma_{SL} + N\pi D(h-l)\gamma_{SV} + N\pi\frac{D^2}{4}\gamma_{SV} + \frac{\sqrt{3}}{2}Nd_0^2\gamma_{SL} - N\pi\frac{D^2}{4}\gamma_{SL} + E_m, \quad (3.43)$$

where E_m is the mechanical energy gained through nanorod clustering. Assuming that all nanorods in a cluster are closely packed, and using the model described in the previous section, the mechanical energy for an N-cluster bundle can be written as

$$E_m = \frac{\pi^2 E_Y D^4 (d_0 - D)^2}{32h^3}(N-1)^2, \quad (3.44)$$

where E_Y is the Young's modulus of the nanorod material. Thus, the total energy change during the spreading and bundling processes is

$$\Delta F = N\pi Dl(\gamma_{SL} - \gamma_{SV}) + N(\frac{\sqrt{3}}{2}d_0^2 - \pi\frac{D^2}{4})(\gamma_{SL} - \gamma_{SV}) + \frac{\pi^2 E_Y D^4 (d_0 - D)^2}{32h^3}(N-1)^2, \quad (3.45)$$

where $\gamma\cos\theta_e = \gamma_{SV} - \gamma_{SL}$ according to Young's theory of a flat surface. In order for the process to be energy favorable, $\frac{d\Delta F}{dN} = 0$,

$$Dl\gamma\cos\theta_e + (\frac{\sqrt{3}}{2\pi}d_0^2 - \frac{D^2}{4})\gamma\cos\theta_e = \frac{\pi E_Y D^4 (d_0 - D)^2}{16h^3}(N-1). \quad (3.46)$$

The total cluster area can be written as

$$A_{cluster} = (N-1)D^2 = \frac{16(Dl + \frac{\sqrt{3}}{2\pi}d_0^2 - \frac{D^2}{4})h^3\gamma\cos\theta_e}{\pi E_Y D^2 (d_0 - D)^2}, \quad (3.47)$$

i.e., the cluster-cluster distance λ can be expressed as

$$\lambda = \sqrt{\frac{16(Dl + \frac{\sqrt{3}}{2\pi}d_0^2 - \frac{D^2}{4})h^3\gamma\cos\theta_e}{\pi^2 E_Y D^2 (d_0 - D)^2}}. \quad (3.48)$$

For the clusters in the center of the watermark, $l = h$, and Eq. (3.48) shows that the average size λ of the cluster in the center of the watermark monotonically increases with the nanorod height,

which is consistent with our observation with different nanorod heights in Fig. 3.13. The decreasing of the cluster size on the edge of the watermark can also be explained by Eq. (3.48). According to the studies on the liquid capillary flow in a groove, the capillary front in the groove can be approximated by linearly decreasing the liquid level with an angle α, which is different from the equilibrium contact angle θ_e [111]. If we make a similar assumption to the liquid front inside the nanorod array, as shown in Fig. 3.19, the behavior of the clustering at the edge of the watermark can be estimated. As shown in Fig.3.19, at distance r_0 from the center of the watermark, the liquid level in the nanorods starts to decrease. At distance r from the center of the

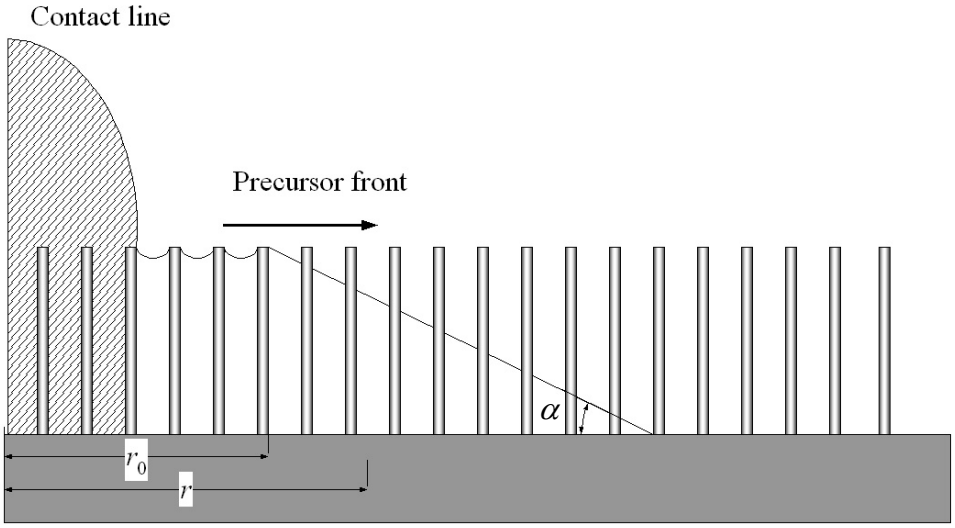

Figure 3.19. The sketch of the water invasion front inside the nanorod array. The water height level l at the edge of the invasion front deceases linearly with a constant angle α with respect to the substrate surface. For simplicity, the bundling of nanorods is not illustrated but it should be like the cluster depicted in Fig. 3.18.

watermark, the height l of the liquid level in the nanorod becomes,

$$l = h - (r - r_0)\tan\alpha\,. \tag{3.49}$$

Then Eq. 3.48 becomes

$$\lambda^2 = \frac{16[Dh - D(r - r_0)\tan\alpha + \sqrt{3}d_0^2/(2\pi) - D^2/4]h^3\gamma\cos\theta_e}{\pi^2 E_Y D^2 (d_0 - D)^2} = \lambda_0^2 - \frac{\lambda_0^2}{h + \sqrt{3}d_0^2/(2\pi D) - D/4}(r - r_0)\tan\alpha \quad , \tag{3.50}$$

where λ_0 is the cluster size in the center of a watermark. Equation (3.50) predicts that if one plots λ^2 versus *r*, at the edge of the watermark, the average area of the clusters should decrease linearly with the distance *r*. The slope of the linear decline, $-\frac{\lambda_0^2 \tan\alpha}{h + \sqrt{3}d_0^2/(2\pi D) - D/4)}$, is determined by the shape and separation of the nanorods. The absolute value of the slope increases monotonically with the nanorod height according to Eq. 3.48. This prediction is consistent with the experimental results shown in Fig. 3.13.

3.2.3 Summary

From the above characterizations and modeling, several stages may exist during the water spreading on the nanorod surface. These stages are sketched in Fig. 3.20. The first stage is when the water droplet impacts the nanorod surface due to gravity. During the impact, the capillary interaction between the water and nanorods starts from the very top of the nanorods. At that moment, the external bending moment acting on the nanorods is high, leading to a large lateral displacement. When the center of the water droplet contacts the nanorod surface vertically above the surface, there is no preferred direction for the nanorods to deform. This corresponds to the morphology of the watermark center (Region I). The second stage is when the water droplet spreads from the top to bottom of the nanorods, which is also governed by gravity [112]. At this stage, the fast spreading water front is on the top of the nanorods, and the spreading direction is

radially out from the center. Since the capillary force acts on the tip of the nanorods, the deformation is large. In addition, unbalanced forces are created as the water front spreads outward: the capillary force between the inside-wall of the nanorods and the spreading water front is always pointing towards the center of the water mark since there is not yet water on the

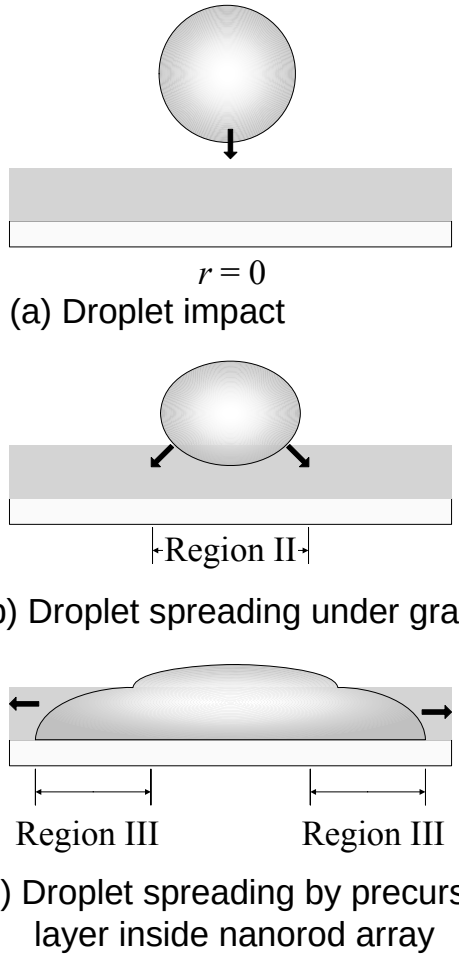

Figure 3.20. The water droplet spreading processes on the aligned nanorod surface: (a) direct impact; (b) spreading under gravity; and (c) capillary invasion.

other side of the nanorods. Thus, a net moment is created that bends all the nanorods towards the center. This gravitation effect should also last for a short period of time which means the physical size of Region II should be much smaller than the size of the ideal water droplet on the surface. Our experimental results in section 3.12 have confirmed this with d_i = 3.5 mm while d_e =

7.7 mm. The third stage is when the water droplet spreads in a percolation manner guided by a layer of precursor front. During the transition period, the spread of the water invasion front inside the nanorods will gradually exceed that of the water droplet front due to the gravitational effect. Therefore, there will be a layer of precursor formed inside the nanorod structure to precede random invasion. This kind of invasion starts from the bottom of the nanorods and it is governed by the thickness of the precursor layer. The closer it gets to Region II, the thicker the precursor layer becomes, and the larger the capillary interaction is (so is the bending moment caused by the capillary force). This interaction decreases during the precursor invasion process. This spreading model is to be tested with carefully designed experiments.

3.3 Freezing a water droplet on an aligned Si nanorod array substrate [113]

3.3.1 Introduction

The nanocarpet effect has a direct impact on the stability of nanostructures used for chemical and biological sensors as well as other related applications in a liquid environment. Thus, to explore more stable nanostructures withstanding the liquid treatment or to design the liquid treatment procedure to prevent this effect is critical for many applications. This relies on a fundamental understanding of the nanocarpet effect, i.e. the detailed physical interactions between liquid and nanorods, nanorods and nanorods, and the dynamic process that causes this effect. In the last two sections we have shown that both the capillary force caused by the liquid and the mechanical bending of the nanostructure play an important role for the nanocarpet effect. Therefore, one could minimize the nanocarpet effect by reducing the surface tension of the liquid, or by improving the mechanical structure of the nanorod array.

There are still controversies in the literature on how the bundling is formed during liquid treatment. So far, two possible mechanisms have been proposed for the structure change. One proposed mechanism is that, after being immersed into a liquid and dried, the aligned nanowires bundle together to form cellular network structures [82,84,88,89]. The direct experimental evidences are a freeze-dry experiment and an *in situ* optical microscope observation of the formation of a cellular network after immersing and drying a 50 μm long aligned CNT array [84]. The other proposed mechanism is that the bundling of nanorods occurred during the spreading of a liquid droplet [70,85,86,90]. The experimental evidence is the color change of the nanorod/nanotube array during the spreading of liquid on the nanostructured surface [86,90]. For both mechanisms, the experimental evidences are indirect. Thus, direct experimental evidence will be needed to resolve this controversy. Here we use a rapid freezing process to investigate the bundling formation during water spreading on a nanorod array surface. Rapid freezing or solidification behavior is fundamental to crystal growth, refrigeration, frost formation, biomedical research and applications such as cryomicroscopy, cryopreservation, and cryosurgery [114-120]. In most cases, ultra-rapid freezing prevents water motion inside structures like tissues, soils, and foods. Therefore, by investigating the top view and cross section of a frozen water droplet on a nanorod array surface, we expect to observe whether the nanorods are bundled together during the spreading process. In addition, the experiment could also tell one how freezing behavior changes on a nanorod array surface.

3.3.2 Experiments

The vertically aligned Si nanorod array sample was prepared by GALD. The substrate was a Si(100) wafer cleaned by RCA1 process. The deposition angle was 86^{o}, and the substrate

rotation speed was 0.15 rev/s. The nominal Si film deposition rate was 0.3 nm/s monitored by a QCM. The total nominal thickness of the Si deposited was 1700 nm. Figure 3.21 shows the top-view and cross-section SEM images of the as-deposited Si nanorod array. From these SEM images, one can obtain the following nanorod parameters: the average nanorod height was

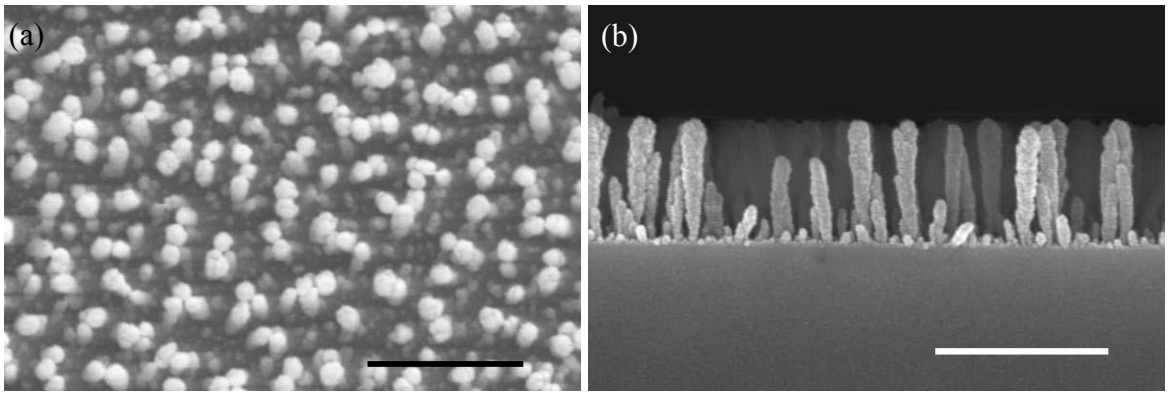

Figure 3.21. SEM images of as-deposited Si nanorod arrays: (a) top-view and (b) cross-section. The scale bars represent 1 μm.

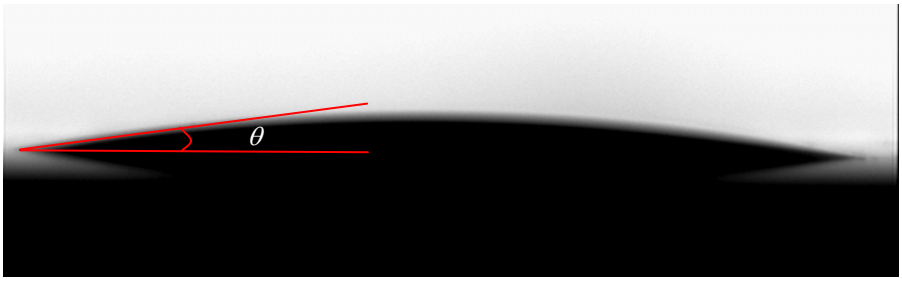

Figure 3.22. The contact angle θ of a water droplet (2 μL) on the Si nanorod array.

708 ± 25 nm; the average nanorod diameter near the top of the nanorods was 113 ± 17 nm; the average nanorod diameter near the bottom of the nanorods (close to substrate) was 36 ± 6 nm; and the average rod-rod separation was 276 ± 93 nm. The static contact angle of an as-grown control sample was measured before the freezing experiment by the sessile drop method. As shown in Fig. 3.22, the water droplet (2 μL) spread very fast on the surface and formed a very

small apparent contact angle θ of 10.9 ± 1.4°. From our previous discussion, for the Si nanorod array with a height of ~ 653 nm, the water was imbibed into the nanorod channels. Therefore, the apparent contact angle became much smaller than the contact angle on a smooth Si thin film. The freezing of water droplets was performed directly on the Si nanorod array samples mounted on a

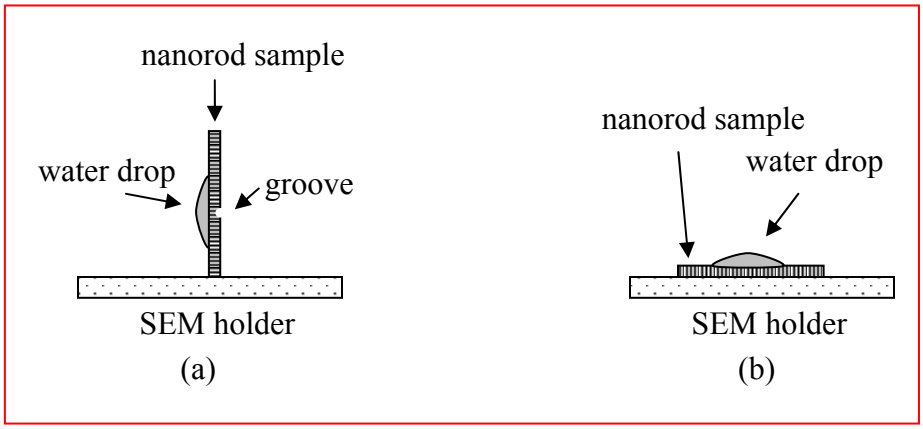

Figure 3.23. The rapid freezing experiment for (a) cross-section SEM imaging, and (b) top-view SEM imaging.

cryo-SEM sample stage (Gatan). In order to obtain a complete picture of the frozen ice/nanorod interface, we have designed two different experiments to acquire both the SEM cross-section and the top-view images of the frozen samples. The Si nanorod samples were cut into a rectangular shape with a dimension of about 0.7 × 1.5 cm^2. To obtain the cross-section SEM of the nanorod/ice interface inside the frozen droplet, a thin groove was engraved on the backside of the substrate with a diamond scriber with great care. Then the sample was mounted vertically to a SEM holder as shown in Fig. 3.23(a) and a water droplet of about 0.5 μL was dispensed onto the sample surface when the sample was laid horizontally. When dispensing the water droplet, the location of the groove on the backside was chosen as the center of the water droplet. Then the sample, while still remaining horizontal, was immediately immersed into liquid nitrogen to

rapidly freeze the water droplet. After that, the sample was transferred to the cryo-SEM loading chamber, where the sample was broken along the pre-cut groove with a sharp blade so that the frozen droplet was also broken cleanly across its center. To obtain the top-view SEM images of the frozen droplet, the nanorod sample was laid horizontally on the SEM sample holder as shown in Fig. 3.23(b). A water droplet of about 0.5 μL was dispensed onto the sample surface, frozen in the liquid nitrogen, and delivered to the cryo-loading chamber. The temperature of the cryo-stage was usually maintained at -170 ^{o}C. However, for the cross-section sample, the temperature of the cryo-stage in the loading chamber was raised temporarily to -90 ^{o}C in order to get rid of possible ice formation on the cross section. All the frozen samples were coated with a thin layer of Au in the loading chamber. Finally, the frozen sample was transferred to the SEM chamber for imaging.

3.3.3 Results and discussions

Figure 3.24 shows the cross-section SEM images of the frozen droplet. From the slope of the frozen droplet (Fig. 2.34a), we calculated that the contact angle was 12.1 ± 1.5^{o}, which was consistent with the static contact angle measured before freezing. This suggests that the shape of the water droplet before and after freezing does not change dramatically. However, with higher magnification SEM images on the nanorod/ice interface (Fig. 3.24b-d), we observed that the entire ice droplet was completely separated from the nanorod array surface, and inside the nanorod arrays, there was almost no observable ice formation. With higher magnification, occasionally we observed ice needles connecting the ice droplet and the nanorods, as indicated by the circles in Fig. 3.24d. The nanorod array also became slightly disturbed and formed small 2-4 rod clusters (cross-section).

Figure 3.25 shows the top-view SEM image of the ice droplet (the shaded area). The inset in Fig. 3.25 showed the overall morphology of the droplet, which was distorted particularly in the top-right corner and the bottom of the image due to extremely low magnification. There were also several ice chips along the boundary of the ice drop. The formation of these irregularities may be due to the local non-uniformity of the nanorod structure and the existence of surface defects. The close-up view SEM image revealed that there were four clear contours on

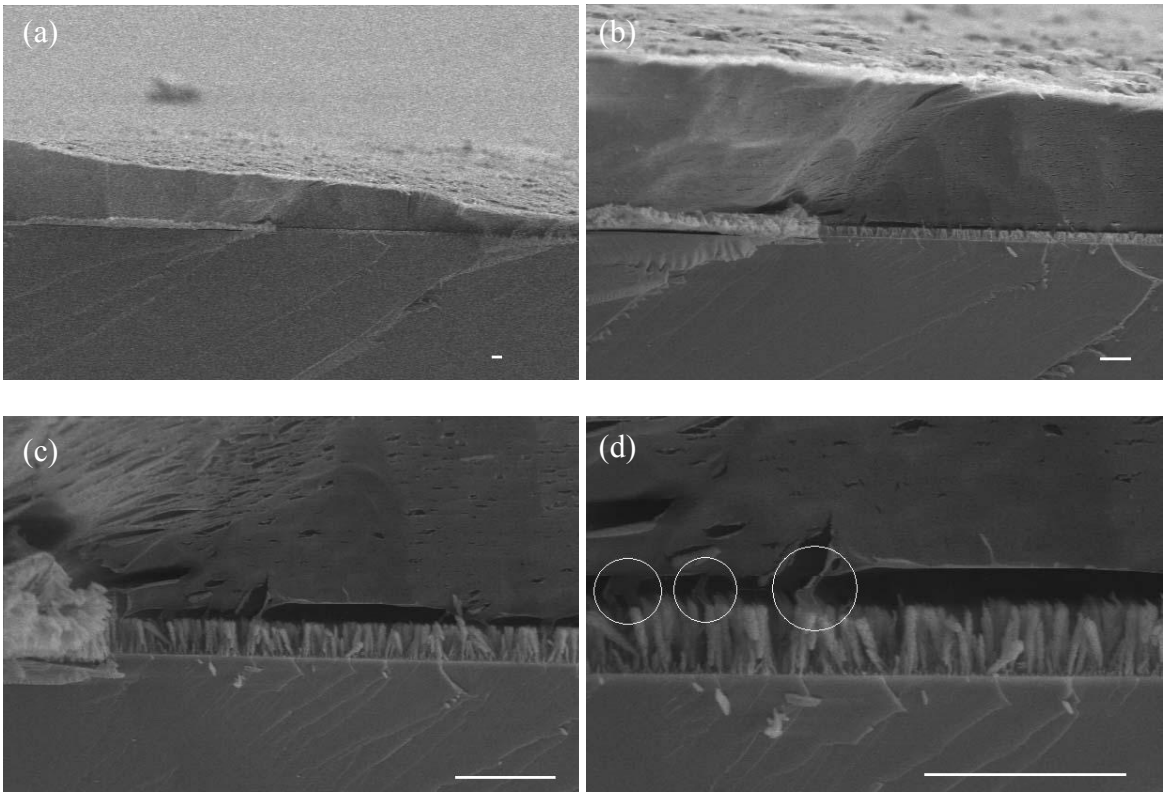

Figure 3.24. Cross-section SEM images of the ice-nanorod interface with different magnifications. The scale bars represent 2 μm.

the surface as illustrated in Fig. 3.25. The L_1 contour was close to the center of the ice droplet, and L_2 was about 0.5 - 1 mm away from L_1. Contour L_3 was about 1-1.3 mm away from L_2, and it was very like an arc of a circle. About another 1 mm away from L_3, there was another contour L_4. These four contour lines divided the top view image into five different regions, and we have

selected seven different locations within the regions to further trace and understand the morphological changes.

Location A was selected right on top of the ice droplet and its top view SEM images were shown in Fig. 3.26a. There were cracks formed on the ice surface during the rapid freezing process. These cracks were formed due to thermal stress. The large magnification image showed that the ice surface was very rough, with fiber-like aggregates uniformly distributed. Those fiber-like aggregates were amorphous ice produced due to the rapid freezing process. Location B, which was about 0.43 mm away from Location A, was at the edge of contour L_1, or at the edge of the ice droplet. We can clearly distinguish the boundary of the droplet from Fig. 3.26b. The

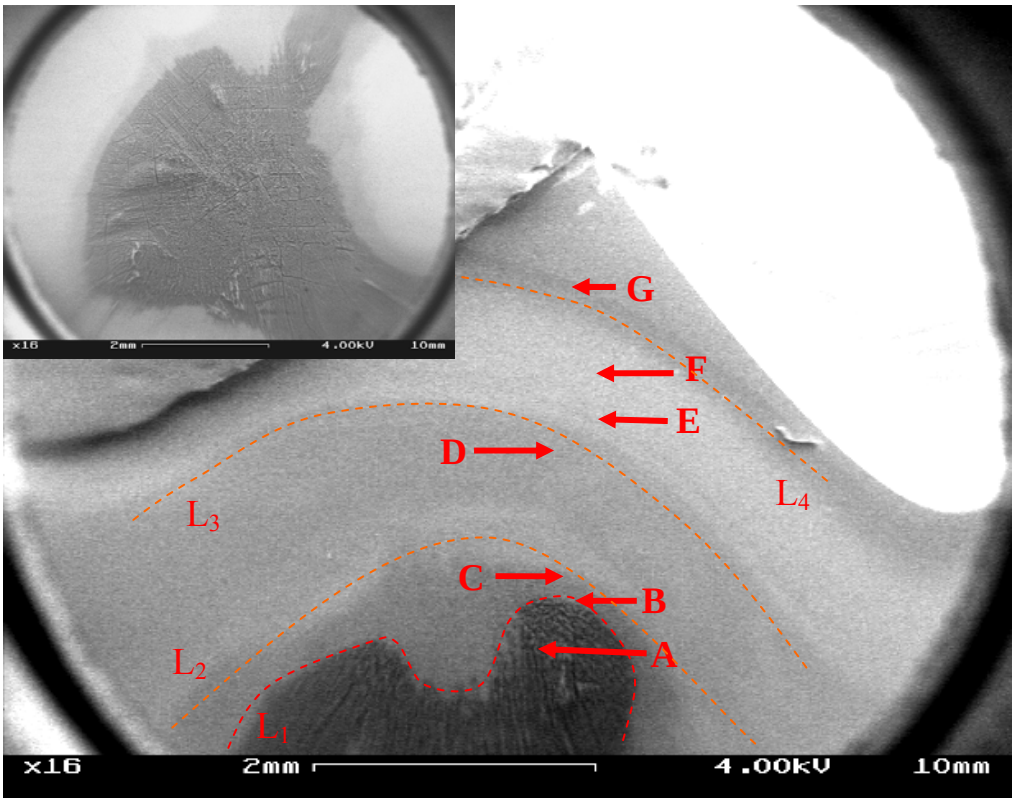

Figure 3.25. The overall top-view SEM images of the ice drop on Si nanorod surface. The inset shows the entire drop. The dashed lines outline the contours and the ends of arrows represent the locations with detailed SEM images shown in Fig. 3.26.

zoom-in SEM image on the upper part of the boundary showed the bundling of the nanorods, with average bundling size of ~ 318 nm, and average bundle-bundle separation of ~ 761 nm. Two other features have also been demonstrated in this SEM image: (1) Almost all the bundled nanorods were tilted downwards, i.e., tilting toward the droplet boundary; (2) particles with diameters smaller than 1 μm were present on the surface. The diameter of the particles was much larger than the average gap (about 60 nm) between the nanorods. Those particles are presumably

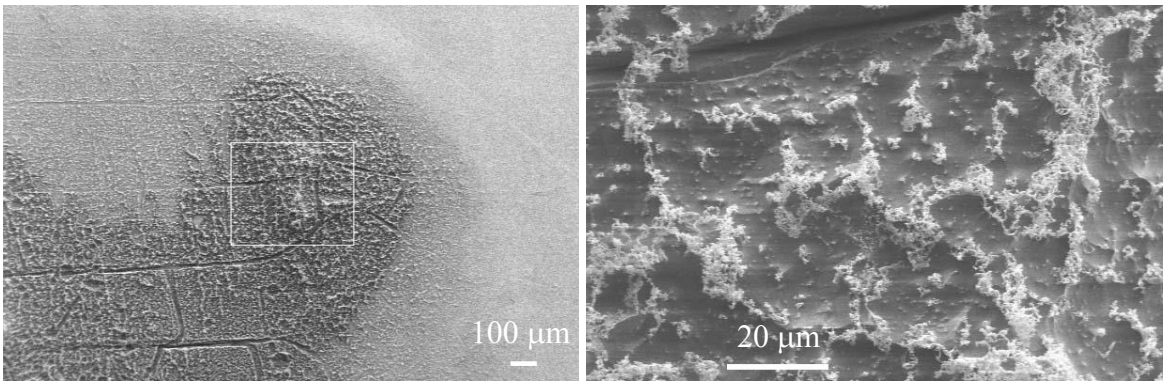

(a) Location A

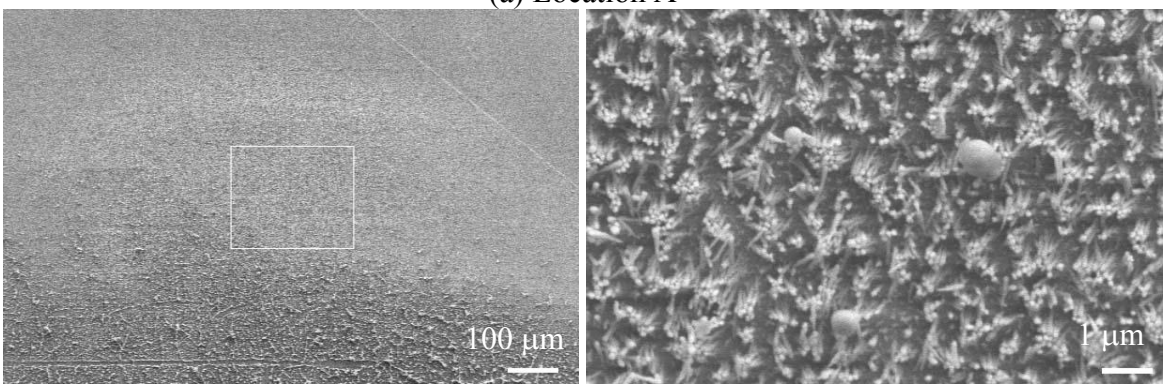

(b) Location B

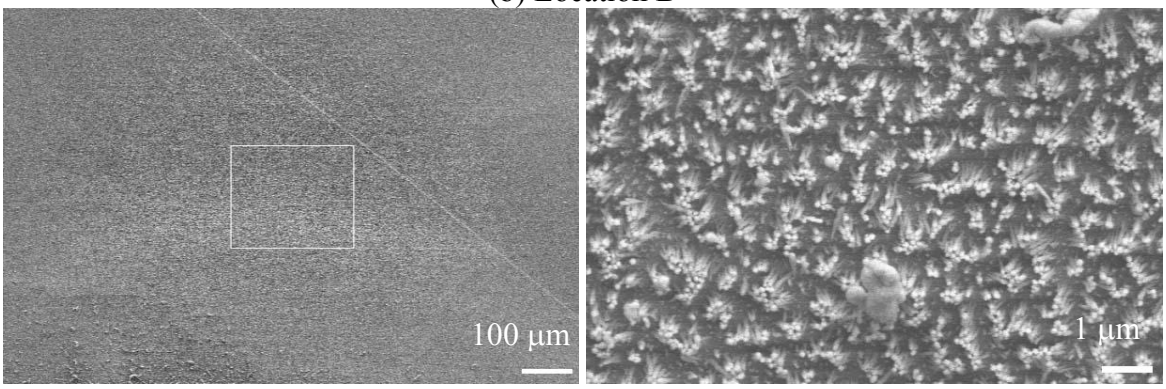

(c) Location C

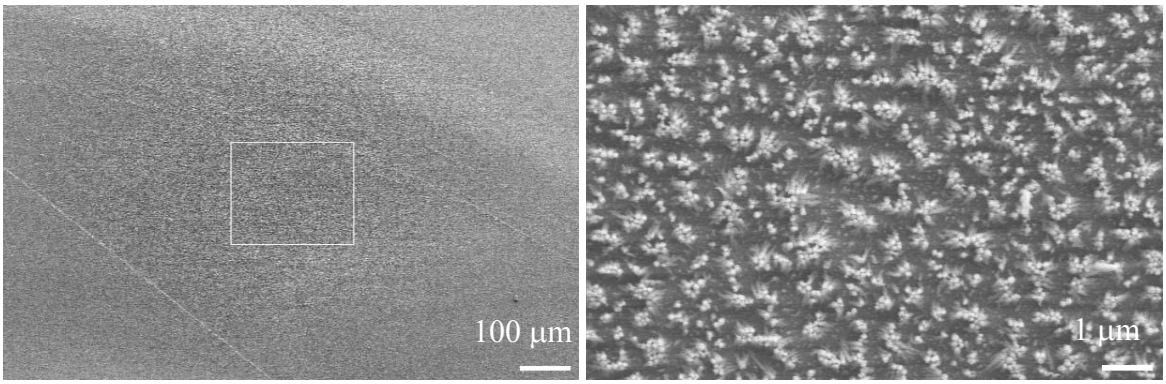

(d) Location D

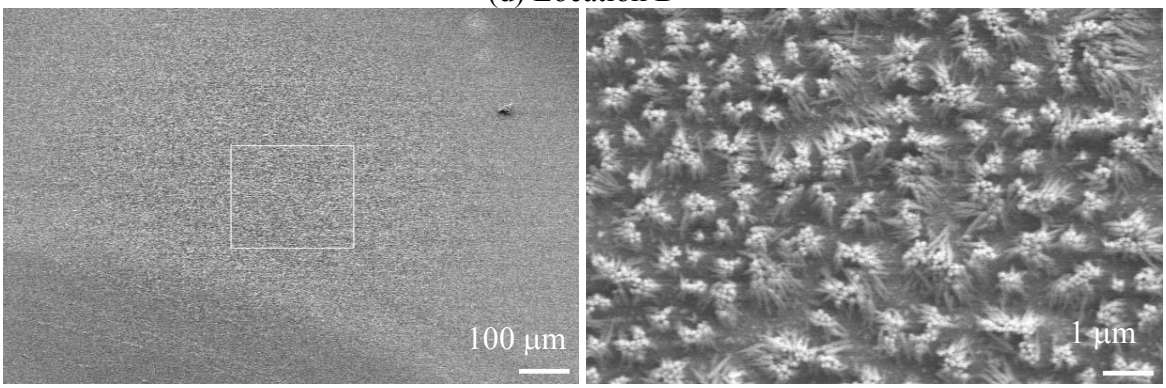

(e) Location E

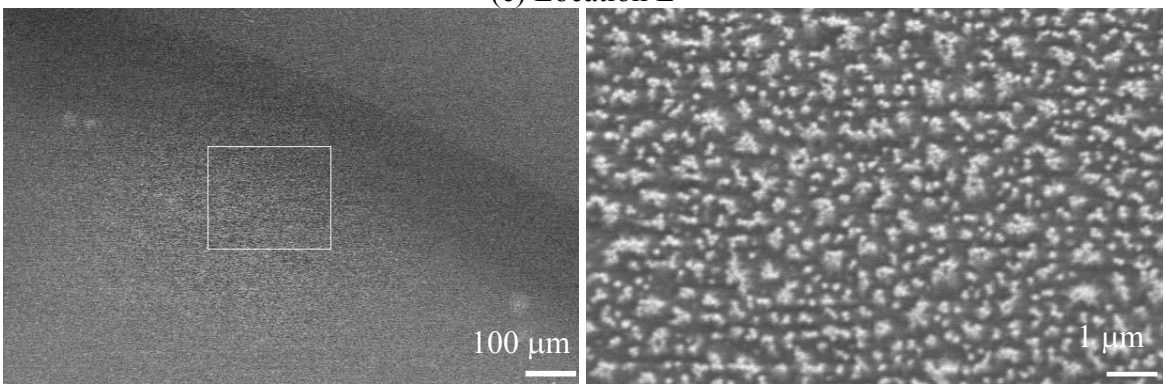

(f) Location F

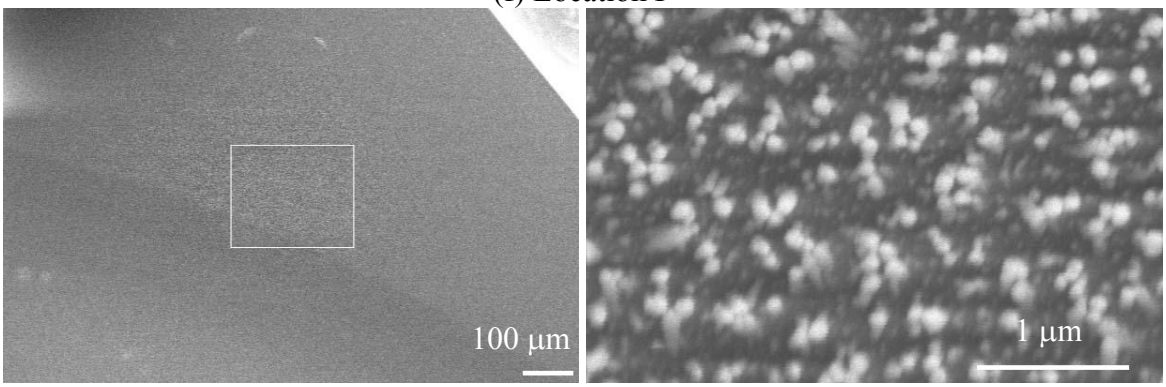

(g) Location G

Figure 3.26. The magnified SEM top view images of Locations A-G labeled in Fig. 3.25.

ice particles. Similar phenomena have also been observed at Location C (Fig. 3.26c), which was about 0.54 mm away from Location A, and was almost on the contour L_2. This indicates that in the belt region between contour L_1 and contour L_2 (the belt width is about 0.5 - 1 mm), the nanorods were bundled towards the ice droplet contour, and there were ice particles formed in this region. This was consistent with our previous observation for the nanocarpet effect, where immediately apart from the central region of the droplet, the nanorods bundle towards the center. Location D was between contour L_2 and contour L_3, and was about 1.4 mm away from Location A. The SEM image shown in Fig. 3.26d also revealed bundled nanorods. Unlike the bundles in Figs. 3.26b and 3.26c, the bundles in Fig. 3.26d were not tilted, and the size of the bundles was about 310 nm, with an average separation ~ 749 nm. There were almost no ice particles on the surface. Location E was at the edge of contour L_3, and was about 1.68 mm from Location A. As shown in Fig. 3.26e, the nanorods bundled with no preferred tilting direction, as demonstrated in Fig. 3.26d. However, the bundle size and the separation became larger as compared to Fig. 3.26e, with size of ~ 467 nm and separation of ~ 975 nm. Location F was between contour L_3 and contour L_4, and was about 1.97 mm away from Location A. The nanorods in this region also bundled together (Fig. 3.26f), but formed much smaller clusters as compared to Figs. 3.26d and 3.26e, with size ~ 217 nm and separation ~ 500 nm. Location G was at the edge of contour L_4, with a distance 2.56 mm from Location A. There was only a slight bundling (about 2-6 nanorods) through the surface, as shown in Fig. 3.26g. Thus, from Location D to Location G, except for Location E, the bundle size became smaller and smaller, which was also consistent with our previous observation for the nanocarpet effect.

Assuming that the fast freezing does not change the overall top-view structure, the above results demonstrate that there were four different regions on the nanorod surface when a water

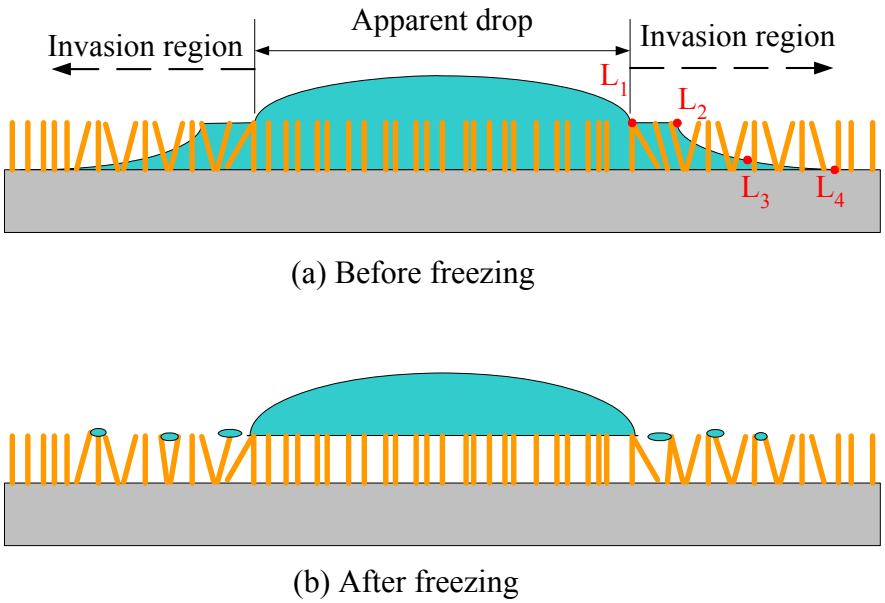

Figure 3.27. The illustration of a water droplet on a nanorod array surface: (a) before freezing; and (b) after freezing.

droplet was spread, which were outlined by contours L_1, L_2, and L_4, as depicted in Fig. 3.27a.The region from the center of the water to contour L_1 was the apparent water droplet, which we observed in Fig. 3.22. In the region between contour L_1 and contour L_2, the water was fully absorbed into the nanorod channels, and the surface became a water-nanorod composite. This composite surface was the new interface for the apparent water droplet to spread on, i.e. when considering the spreading dynamics of the water droplet on the nanorod array surface, the apparent advancing front of the water droplet moved on the water/nanorod composite surface, rather than on a fresh nanorod array surface. In the region between contour L_2 and contour L_4, the water level inside the nanorod channels decreased monotonically with the distance from the center of the droplet, and this was the precursor front or the stain area [121]. This model is consistent with the water invasion model shown in Fig. 3.19. After rapid freezing, the water within contour L_1 became an ice droplet as shown in Fig. 3.27b. The nanorods below the ice

droplet slightly bundled together, while the water in the region between contour L_1 and L_2 emerged from the nanochannels and formed small ice particles on the nanorod surface. A similar effect occurred in the region between contour L_2 and contour L_4. However, since the amount of water inside the nanochannels was less than that in region between contour L_1 and contour L_2, the density and the size of the ice particles were much smaller. The contour L_3 observed in Fig. 3.25 was between contour L_2 and contour L_4, and could be due to the fluctuation of the precursor front during the rapid freezing. The above discussion elicits two very interesting phenomena. First, in the ice droplet region, the ice growth front is almost completely separated from the nanorod surface; secondly, in regions between contour L_1 and contour L_4, there are formations of nanorod bundles.

In principle, at liquid nitrogen temperature, the critical nucleation radius of water is about 4.3 nm [122]. Therefore, it is possible for ice particles to form inside the nanochannels. However, in the rapid freezing process, a thin layer of water prefers to form structures much larger than that of a critical radius. To estimate the size and shape of the nanoparticle, we performed a similar experiment with a water droplet on a flat Si(100) surface. The top view SEM images were shown in Fig. 3.28. The precursor was formed during the spreading of the water droplet and was located at the edge of the frozen droplet (the circled area in Fig. 3.28a). There were cotton-like structures formed in the precursor region, which were ~ 10 μm long and a few micrometers wide. Those are the preferred structure for this rapid freezing. These kinds of structures were also observed in the region between contour L_1 and contour L_4 on the nanostructured surface as shown in Fig. 3.29. If those structures can be formed inside the nanorods, they should connect more than 100 nanorods. Therefore, the volume expansion of the water into ice should cause those 100 nanorods to be displaced or bent, which introduces extra free energy, i.e. the

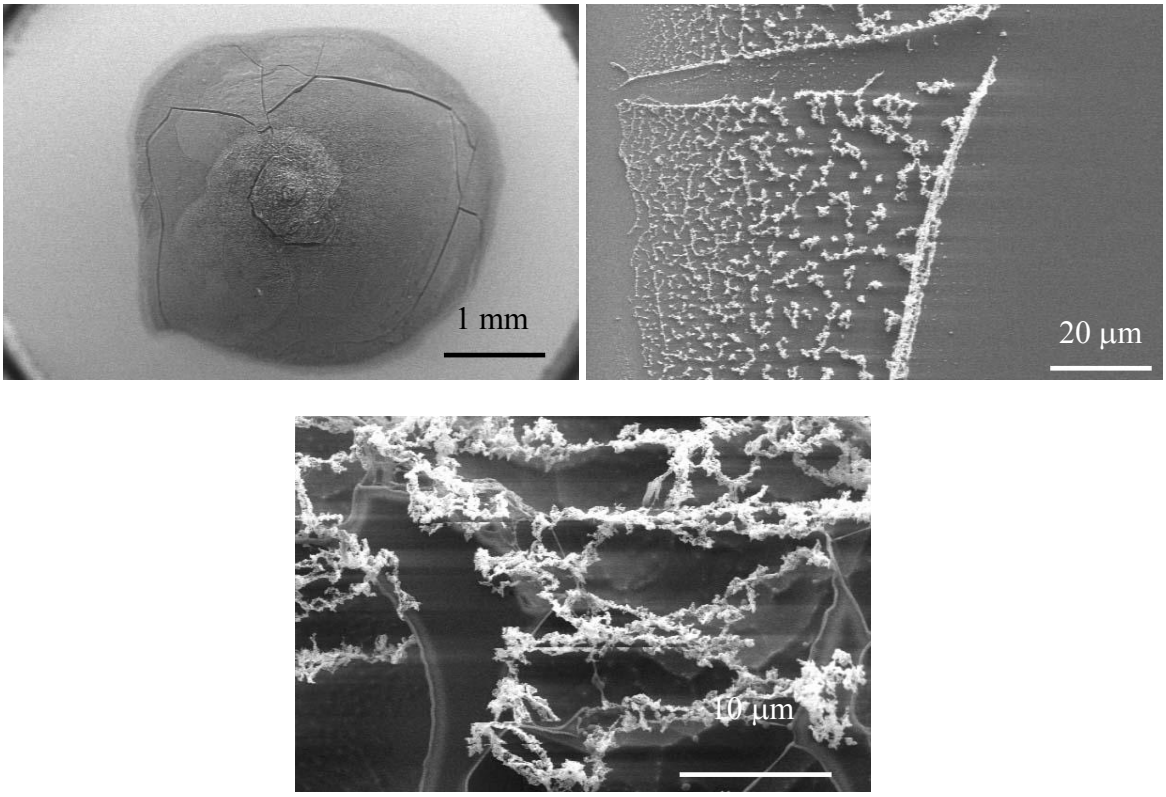

Figure 3.28. The top view SEM images of a frozen water droplet on a flat Si surface with different magnifications.

mechanical bending energy. However, this process should not happen because it is not energetically favorable for the formation of water clusters inside the nanorods.

The slight bundling of nanorods underneath the ice drop may be caused by the spreading process, where the advance of water flow and the viscosity drag force deform the nanorods slightly. When the nanorods are entirely immersed in water, the net interaction between the water and nanorods is almost zero, which will not cause further bundling. During the freezing, the water diffuses upwards to the ice growth front simultaneously around the nanorods, which is not likely to cause further deformation. Therefore, the slight bundling of nanorods underneath the ice drop is mainly due to the spreading process. Comparing the bundling to those from dried surfaces as shown previously, we conclude that the drying process is the main cause of the

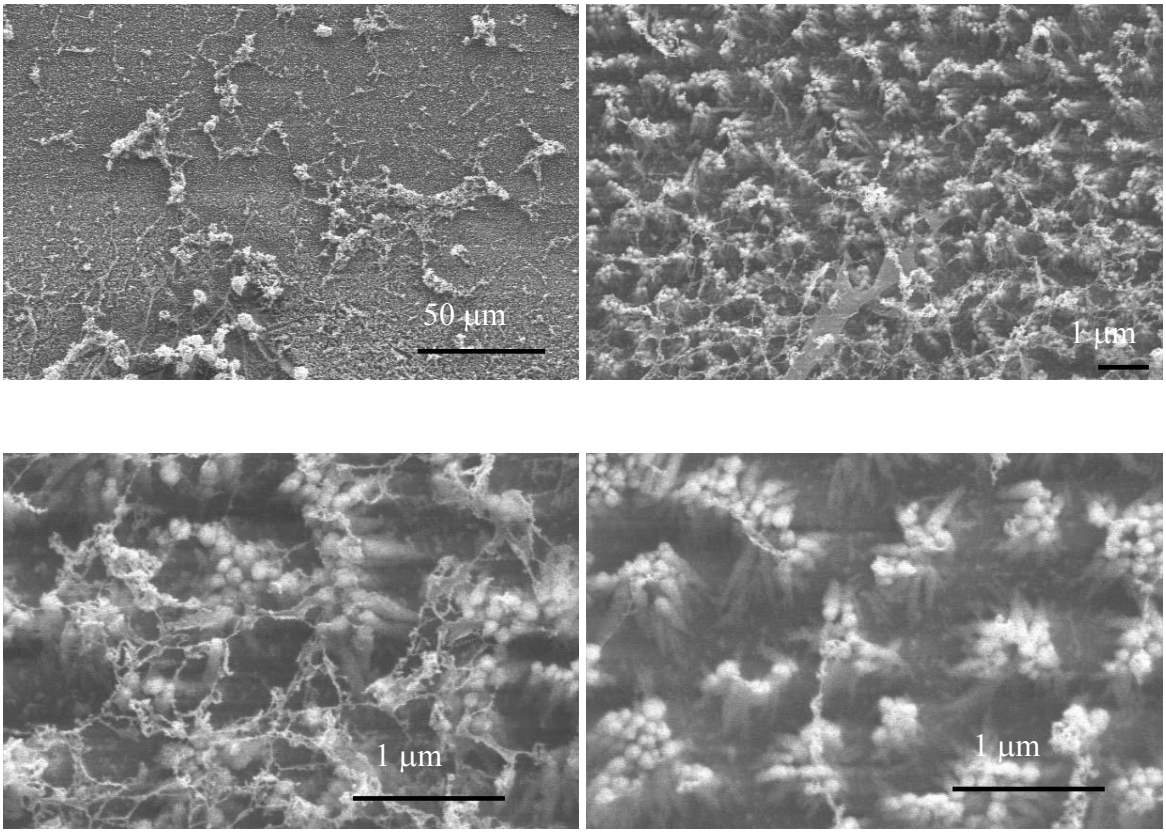

Figure 3.29. The cotton like ice structures formed on Si nanorod substrate.

bundling of nanorods under the apparent water droplet. The tilted bundling in the region between contours L_1 and L_2, as well as the bundling in region between contours L_2 and L_4, is caused by the spreading process. As illustrated in Fig. 3.27(a), the level of the water meniscus inside the nanorod channels deceases with the increasing distance from the apparent droplet. Concurrently, the slope of the meniscus also decreases. Thus, unlike the nanorods in the central region, the nanorods in the precursor film experience a net torque due to different heights of the capillary force acting on both sides of the nanorods during the dynamic spreading process. This torque also decreases with the increasing distance from the apparent droplet due to the shape of the meniscus. This is the reason for the formation of relatively large nanorod bundles in the regions close to the contour L_1. For the nanorod bundles tilting towards the edge of the apparent droplet

in the belt region outlined by L_1 and L_2, we propose that the local fluid flow plays a central role. Near the boundary, the water below the apparent droplet penetrates into the unfilled nanorod channels. This flow is compensated by the flow from the apparent droplet along the boundary in a caterpillar-like motion [112].

3.3.4 Conclusions

From above discussions, we have reached two conclusions. First, the rapid freezing of a water droplet on the top of a nanostructured surface does not preserve the water inside the nanochannels, instead, almost all the water forms ice on top of the nanorod surface, either as a planar interface or as particles, depending on the locations. The phenomenon of the separated ice-nanorod interface is very interesting, and may find some important applications. For example, since the ice and nanorods are separated, a freeze-dry experiment can be designed to separate liquid from nanostructured surfaces with the minimum deformation to the nanorod array structure. Similarly, a nanostructured surface can be designed for crystal growth, so that after crystallization, the crystal can be easily separated from the substrate. This method can also be applied to separate fluid from biological cell membranes and perhaps intact cells and tissues. Second, the nanorod bundling can be induced by either spreading or drying, and it is caused by a net torque resulted from the uneven distribution of the capillary force exerted on the surroundings of the nanorods. This implies that controlling the way of liquid contacting/leaving nanostructures may provide a route to minimize the nanocarpet effect. For example, the bundling can be minimized by immersing the entire nanorod samples inside a liquid with the surface structures contacting uniformly with the liquid surface. When the samples are to be dried, a uniform evaporation will be preferred to avoid bundling. However, this process is hard to control,

since the liquid usually dewets a surface non-uniformly due to the chemical or morphological non-uniformity of the surface. A freeze-dry process is suggested to eliminate this effect.

3.4 The affect of the shape of nanorod arrays on the nanocarpet effect [123]

3.4.1. Introduction

The nanocarpet effect presents a challenge for applications of nanostructures that involve a liquid environment. For example, in biosensing, enzymes or antibodies need to be immobilized onto high aspect ratio nanostructures. On these high aspect ratio nanostructures there are multiple liquid treatment steps involved. After those treatments, the arrangement of the nanostructures may totally change due to the nanocarpet effect. As a result, one may not be able to obtain desired performances of the sensors with desired sensitivity and reproducibility. Thus, there is an urgent need to find/design high aspect ratio nanorod/nanotube arrays to minimize the nanocarpet effect, i.e., to make the nanostructure more stable in liquids. Nguyen et al. use spin-on glass to fill the CNT gaps and provide mechanical support for the structure to prevent the structure from totally collapsing [89]. As a result, the CNTs bundle less severely and a nucleic acid coupling test shows improved coupling. However, this treatment blocks the channels from ion exchange and macromolecule diffusion. In this section, we investigate the wet treatment of five different nanostructures fabricated by GLAD: vertically aligned, tilted, zigzag, square spring and capped nanorod structures, and we compare their stabilities. We show that the zigzag and spring structures significantly improve the stability of nanorod arrays. We also demonstrate that with a minimum sacrifice of the total surface area, the capped nanorod structure is very stable and is promising for chemical and biological sensing.

3.4.2 Experiment

The Si nanorod arrays were prepared by the GLAD technique. The substrates were *p*-type Si(100) wafers cleaned using the RCA1 method for 10 minutes followed by thorough DI water rinsing. The deposition rate was 0.3 – 0.4 nm/sec. To achieve different shaped nanorod arrays such as vertically aligned nanorods, titled nanorods, zigzag, and square spring structures, one simply programs the azimuthal rotation of the substrate about its normal axis. A sketch of these four nanorod structures is shown in Fig. 3.30(a)-(d). The length of the nanorod (or the arm length of the zigzag or square spring) was controlled during the deposition. For vertical nanorod growth, the substrate was rotated continuously with an azimuthal rotation rate of

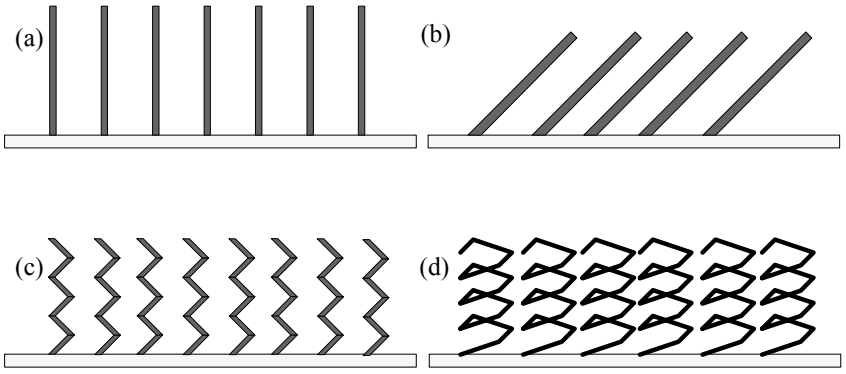

Figure 3.30. A sketch of (a) the vertically aligned, (b) the tilted, (c) the zigzag, and (d) the square spring nanorods

0.5 rev/sec. For titled nanorods, the rotation rate was 0 rev/sec, i.e., stationary, during the deposition. For zigzag structure, the substrate was rotated alternatively between two azimuthal angles 0^o and 180^o (0^o was the initial position of the substrate) for the deposition of each arm (e.g. Fig. 3.30(c) shows 6 arms with each arm resembling those in Fig. 3.30(b)): at 0^o, deposit tilted nanorod of a desired thickness (arm length) without rotation, then rotate the substrate

azimuthally 180^{o} (at a speed of 0.5 rev/sec) and deposit the tilted nanorod with the same thickness, and then rotate back to 0^{o} and repeat the deposition process again till the desired number of arms is reached. For square spring fabrication, the deposition was similar to that of the zigzag nanorod structure, but the substrate was rotated sequentially from $0^{o} \rightarrow 90^{o} \rightarrow 180^{o} \rightarrow 270^{o} \rightarrow 360^{o}$ (0^{o}) for the deposition of each arm in one pitch of the spring. In our experiment, the nominal film thicknesses for vertical and tilted nanorods were 3.2 μm while the zigzag and square spring structures each composed 8 arms with nominal arm thickness of 400 nm. For preparing the capped nanorod structure, a Si film was deposited on top of the vertical Si nanorods. More details on determining the film deposition angle will be discussed later. To investigate the stability of these structures in a liquid environment, the nanorod samples with different shapes were immersed in DI water and then dried at room temperature (~ 25 ^{o}C, and 30-40% relative humidity). The nanorod/arm length and structures of these as-grown samples together with water induced patterns were characterized by SEM.

3.4.3 Results and discussion

Figure 3.31(a)-(d) shows the SEM top-view and cross-sectional images of the vertical, tilted, zigzag and square spring Si nanorod structures, respectively. From Figure 3.31(a), the Si nanorods had an average vertical height h_r = 1.19 ± 0.08 μm, and they had an increasing diameter from bottom to the top, i.e., the diameter near the bottom was 33 ± 4 nm and 128 ± 32 nm near the top. A scaling relationship of the nanorod diameter with the nanorod height has been reported by Karabacak et al. [91]. For tilted nanorods, as seen from Fig. 3.31(b), they had a tilting angle $\beta = 51 \pm 3^{o}$ with respect to the substrate normal, and the nanorod length was l = 3.16 ± 0.12 μm. Thus the vertical height was $h_t = 3.16 \times \cos 51.4^{o} \approx 1.97$ μm. For tilted nanorod

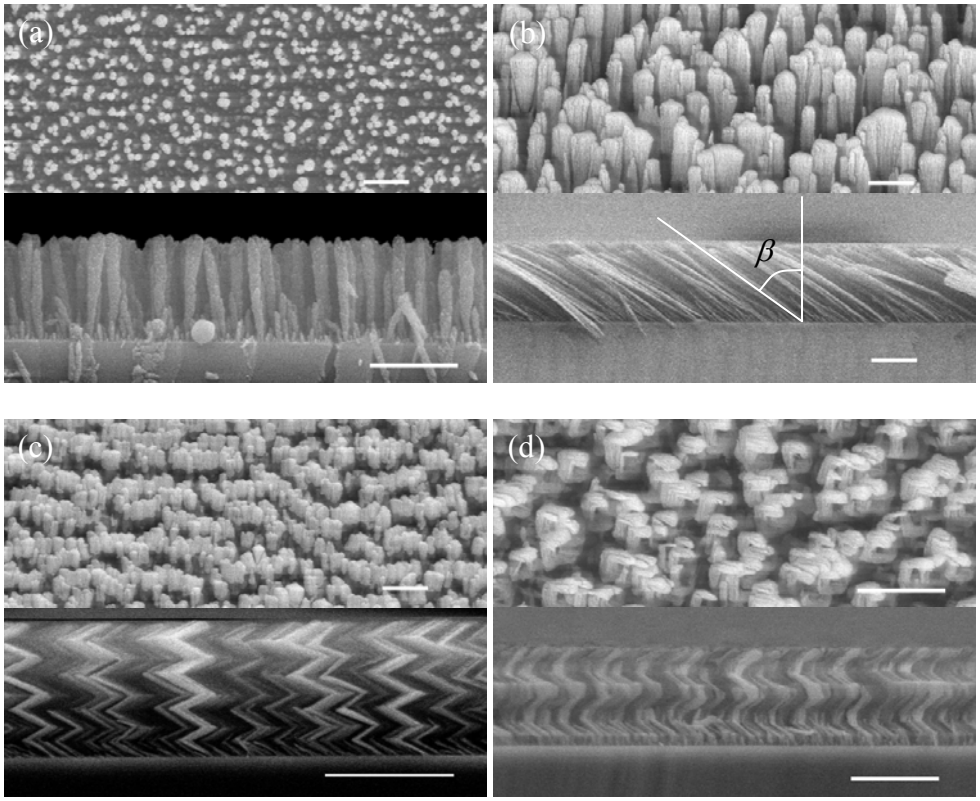

Figure 3.31. Top-view and cross-section SEM images of the (a) vertical, (b) tilted, (c) zigzag, and (d) square spring Si nanorod arrays. In each image, the upper half is the top view and the lower half is the cross-sectional view. All the scale bars in the SEM images are 1 μm.

growth, the nanorod cross section was not circular due to a so-called "fan-out" effect. This effect caused the nanorod broadening in the direction (the "fan-out" direction) perpendicular to the plane (deposition plane) of the incident flux and the substrate surface normal [26,27], and the structure of the rods was more like the shape shown in Fig. 3.32. For zigzag and square spring structures, each arm was a tilted nanorod. The average tilting angle was about 54 ± 3^{o} which is in agreement with the tilting angle β of the tilted nanorod arrays. The vertical heights of the zigzag and square spring structures were $h_z = 1.44 \pm 0.02$ μm and $h_s = 1.15 \pm 0.01$ μm, respectively. Thus the average individual arm lengths of the zigzag and square spring structures were 307 nm (total arm length ~ 2.46 μm) and 245 nm (total arm length ~ 1.96 μm), respectively. The "fan-

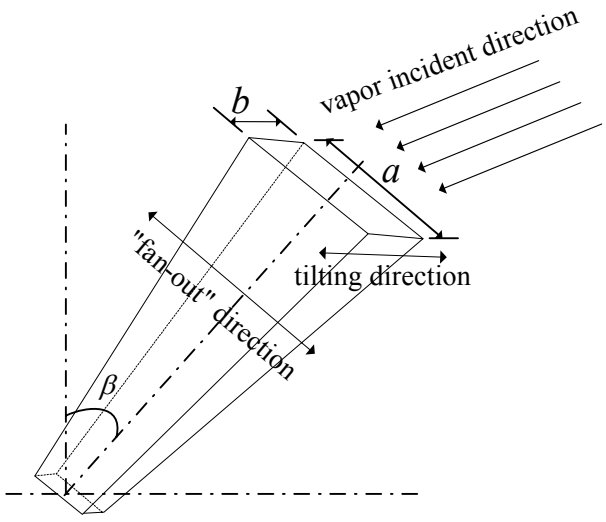

Figure 3.32. A sketch of a tilted nanorod having a rectangular cross section: *a* and *b* are the lateral lengths of the nanorod top in the "fan-out" and tilting directions, respectively.

out" effect was also observed from the top-view SEM images for these two structures.

To obtain a quantitative comparison of the top-view nanorod structures before and after water treatments, we used the power spectrum (PS) to analyze the SEM images. Figure 3.33(a)-(d) shows the power spectra of the as-prepared nanorod structures. For vertical nanorods (Fig. 3.33(a)), there was a circular ring in the two-dimensional PS plot. The radius of the ring k_c is the reciprocal of the average nanorod-nanorod separation r_c, with $r_c \sim 1/k_c$, while the width of the ring reflects the uniformity of the separation. The calculated nanorod-nanorod separation (after circular average to improve the statistics) was 430 ± 37 nm, which is consistent with the estimation from the top-view SEM image shown in Fig. 3.31(a). For tilted nanorods, the PS shown in Fig. 3.33(b) did not reveal a circular ring. Instead, we observed an oval shaped PS. From Fig. 3.33(b), the separations of the tilted nanorods were estimated to be $d_h \sim 899 \pm 336$ nm in the horizontal direction (or the "fan-out" direction) and $d_v = 1301 \pm 393$ nm in the vertical

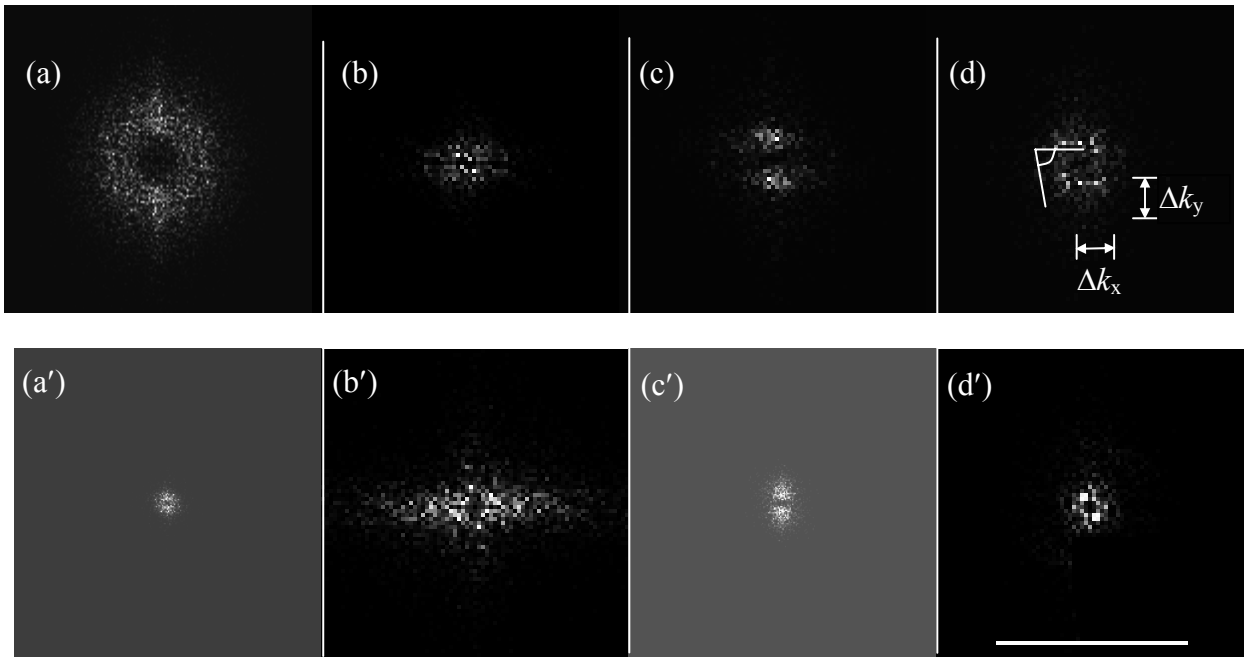

Figure 3.33. Power spectra of the (a) vertical, (b) tilted, (c) zigzag, and (d) spring nanorod arrays, respectively. (a′)-(d′) are the power spectra of the corresponding nanorod arrays after being immersed in water and dried in air. The scale bare is 10 μm^{-1}.

direction. Thus the eccentricity was $e_{\text{tilt}} = \sqrt{1-\left(d_{\text{h}}/d_{\text{v}}\right)^2} \approx 0.72$. For zigzag nanorods, two large bright spots were observed in the vertical direction of the PS (Fig. 3.33(c)). These two spots in the vertical direction demonstrated that the surface morphology of the zigzag nanorod arrays had high periodicity in the vertical direction. Compared to that in the horizontal direction, these two spots were also in the same plane of the zigzag structure, which reflected the symmetry of the nanorod. From Fig. 3.33(c), the separation of the zigzag structure in the vertical direction was d_{v} = 701 ± 130 nm. However, the PS only had very few dim dots (barely visible when increasing the image contrast) along the horizontal axis. This implied the zigzag structure was quite random in the horizontal direction, without a characteristic length. By measuring directly from the top-view SEM image in Fig. 3.31(c), the average horizontal separation for the zigzag structure was d_{h} = 369 ± 123 nm. Then the eccentricity was $e_{\text{zigzag}} = \sqrt{1-\left(d_{\text{h}}/d_{\text{v}}\right)^2} \approx 0.85$. The PS for the

spring nanorods showed a rhombus shape (Fig. 3.33(d)), with $\Delta k_x = \Delta k_y = 2.09\ \mu m^{-1}$ and an acute angle of 73.3^o as indicated in the figure. Thus the spring-spring separation was $2/(\Delta k_x \sin 73.3^o) =$ 999 nm. The shape of the PS of the nanospring arrays also reflected the symmetry of the square spring structure.

In order to investigate the effect of water on different nanorod arrays, we dipped the sample entirely into water instead of dispensing a water droplet onto the sample surface and then took it out gently and allowed it dry in air. The SEM image (Fig. 3.34(a)) of the dried nanorod surface confirmed that the nanorods bundled together. This demonstrated that the bundling does

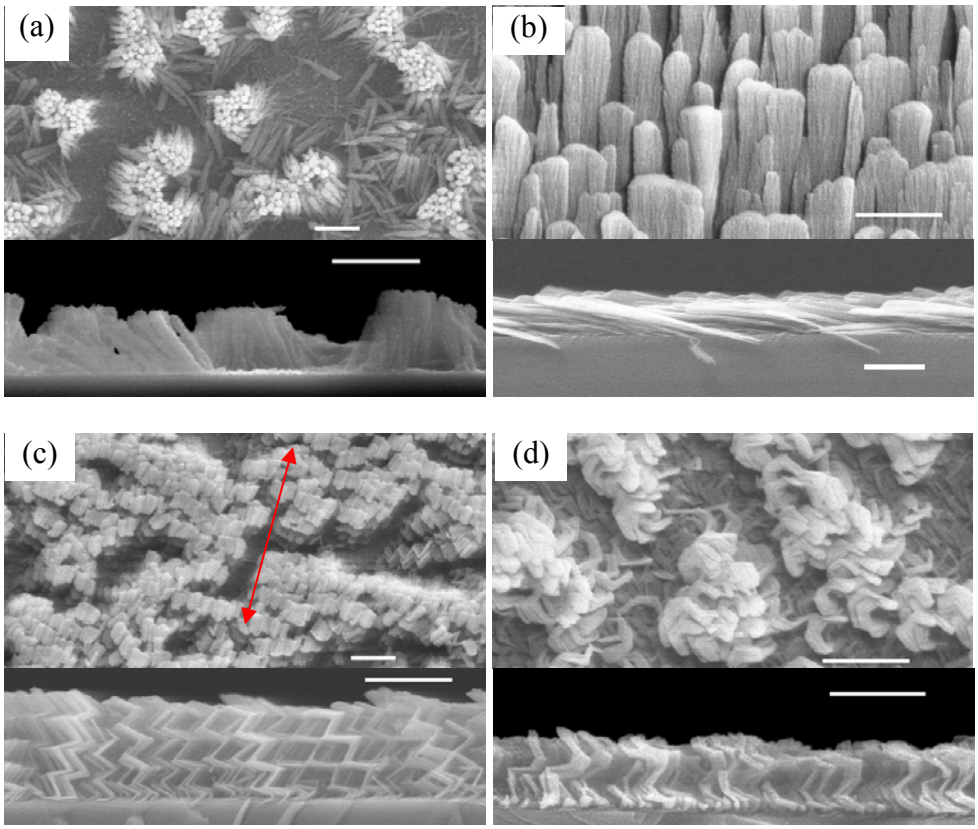

Figure 3.34. Top-view and cross-section SEM images of the (a) vertical, (b) tilted, (c) zigzag, and (d) square spring Si nanorod arrays after being immersed in water and dried. In each image, the upper half is the top view and the lower half is the cross-sectional view. The double arrow in (c) marks the deposition plane in which zigzag nanorod prefers to bundle. The scale bars for all the SEM images are 1 μm.

not depend on how water invades the sample surface (or the bundling could happen during the drying process). The PS of the wetted structure is shown in Fig. 3.33(a′). Comparing to Fig. 3.33(a), a similar ring shape was observed but with a smaller radius. This radius reflected the average separation of the bundled nanorod cluster, which was found to be 3.04 ± 0.47 μm. This result agrees with the power law relationship of the bundle size versus nanorod height [109]. The cross-sectional view SEM image in Fig. 3.34(a) gave a detailed view of how the nanorods were bundled together. Due to the bending of the nanorods, the height of the nanorod film became $h_{\mathrm{r}}^{'} = 854 \pm 89$ nm. Thus, the height ratio R_{r}, which was defined as $R_{\mathrm{r}} = h_{\mathrm{r}}^{'} / h_{\mathrm{r}}$, was $\sim 72\%$.

Figure 3.34(b) (the upper image) showed the morphology of the tilted nanorod structure after dipping in water. From the top-view SEM image, one can not tell whether the nanorods bundle together or not, but the average visible length of the nanorods in the SEM image along the tilting direction became longer as compared to that in Fig. 3.31(b), which suggested that the nanorod tilting angle β became larger. This was confirmed by the cross-sectional SEM image in Fig. 3.34(b) (the lower image). The tilting angle β was measured to be 77 ± 3°. Thus the vertical height of the nanorod film decreased to $h_{\mathrm{t}}^{'} = 3.16 \times \cos 77^{\mathrm{o}} \approx 0.71$ μm, and the height ratio was $R_{\mathrm{t}} \sim 36\%$, indicating a significant bending towards the surface. The PS of the water treated structure in Fig. 3.33(b′) showed an oval shape more elongated in the horizontal direction as compared to that of Fig. 3.33(b), while there was no obvious change in the vertical direction. This wide distribution of the PS in the horizontal axis suggested that there was a broad length scale distribution in the horizontal direction (Fig. 3.34(b)). Direct measurement from SEM images showed the average horizontal separation was 798 ± 341 nm, which was comparable to that of the as-prepared nanorod structure in Fig. 3.31(b). This anisotropic bending is attributed to the "fan-out" nature of the tilted nanorods. Figure 3.32 showed a sketch of a single tilted nanorod.

The length of the nanorod top along the "fan-out" direction was about a = 477 ± 112 nm, while the length along the "tilting direction" was about b = 77 ± 16 nm. From classical mechanics, the deflection of a beam is expressed as

$$\Delta y = FL^3 / 3EI = \chi L^3, \tag{3.51}$$

where Δy is the displacement, F is the force exerted on the top, L is the length of the beam, E is the modulus of elasticity, and I is the area momentum of inertia [110]. The bending factor χ is defined as $\chi = F / 3EI$. If we treat the cross section of the tilted nanorod as a rectangle of $a \times b$ in two dimensions, for the bending in the tilting direction, the area moment of inertia is $I_t = ab^3/12$; while for the bending in the "fan-out" direction $I_f = a^3b/12$. Since $a >> b$, $I_t << I_f$. Thus, the bending in the tilting direction will be much easier than the "fan-out" direction if applying the same force on the top. In fact, the capillary forces acting in the two directions are also different. It is reasonable to assume that the capillary force per unit length on the nanorod surface is the same for both directions. Thus for bending in the tilting direction, the force is a/b times that of the "fan-out" direction. Therefore, the bending distance in the titling direction to that of the "fan-out" direction can be estimated as $\Delta y_t / \Delta y_f = (a/b)^3 \approx 238$, which is over two orders of magnitude larger.

For zigzag and square spring structures, each individual nanorod occupied a larger lateral size (arm length × cosβ) compared to a straight nanorod (diameter of the nanorod). It was expected that the joints of the arms would touch each other first during bending and thus prevent further bending. For the zigzag structure sketched in Fig. 3.30(c), all arms were in the deposition plane, so bending would be reduced in this plane; while for the square spring structure sketched in Fig. 3.30(d), arms existed in two planes perpendicular to each other thus bending would be reduced in both planes. However, from the SEM images (Fig. 3.34(c) and (d)), we found both

structures bent after the water treatment. The zigzag nanorods bent mostly in the deposition plane (marked by an arrow in the SEM image), which was similar to the tilted nanorods. One can also attribute this to the "fan-out" effect. The difference was that the zigzag nanorods bundle together to form large clusters, as indicated by the decrease of the pattern size in the PS (Fig. 3.33(c′)), while the tilted nanorods bent toward the surface with no obvious bundling. The bundle size was 5.46 ± 1.11 μm in the "fan-out" direction as directly measured from the top-view SEM images and 2.49 ± 1.03 μm in the orthogonal direction, which was obtained from the PS. From the cross-sectional SEM image, we found out that the bundled film height changed to $h_z^{'}$ = 1.24 ± 0.09 μm, and the height ratio changed to $R_z \sim$ 86%. For the square spring structure, the nanosprings bundled together from all directions. The uniformity of the bundling was confirmed by the circular ring pattern in Fig. 3.33(d′). The nanospring bundle size was 1.53 ± 0.20 μm. After bundling, the height of the spring structure changed from 1.15 ± 0.01 μm to $h_s^{'}$ = 0.92 ± 0.08 μm, and the height ratio became $R_s \sim$ 80%. The height ratios R_z and R_s are significantly larger than R_t and R_r.

In order to compare the stabilities of these structures, Table 3.1 summarizes the total lengths and heights of the four nanorod structures before and after water treatment. It is seen that neither the total length nor the height of the four original nanostructures is the same. To eliminate the effect of the nanostructure height difference, we can estimate the length-independent bending factor $\frac{F}{3EI}$ by assuming that the zigzag and spring nanorods can be treated effectively as a vertical nanorod. For a nanorod with a tilting angle of β, from Eq. (1), the film height h' after water treatment is

$$h' \approx \sqrt{L^2 - (L\sin\beta + \Delta y)^2} = L\sqrt{1 - \left(\sin\beta + \chi L^2\right)^2} \,. \tag{3.52}$$

Thus, the height ratio R can be expressed as

$$R = \frac{h'}{h} = \frac{1}{\cos\beta}\sqrt{1 - \left(\sin\beta + \chi L^2\right)^2} \tag{3.53}$$

For vertical nanorods ($\beta = 0$, $L = h$), the above equation can be reduced as

$$R = \sqrt{1 - \chi^2 h^4} \,. \tag{3.54}$$

For zigzag and spring nanorods, we assume they have effective area moments of inertia, I_{eff}. Therefore, for the vertical, tilted, zigzag and spring structures, one obtains that the bending factors χ are 0.49, 0.03, 0.25, and 0.45 μm^{-2}, respectively. This clearly demonstrates that the

Table 3.1. Comparison of the film height change after water treatment

	Total length of nanorod l (m)	Original vertical height h (m)	Height after water treatment h' (m)	Height Ratio R (%)	Bending factor γ (μm^{-2})	χ/l (μm^{-3})
Vertical nanorods	1.19	1.19	0.85	72	0.49	0.41
Tilted nanorods	3.16	1.97	0.71	36	0.03	0.01
Zigzag structure	2.46	1.44	1.24	86	0.25	0.1
Spring structure	1.96	1.15	0.92	80	0.45	0.23

tilting nanorod array has the smallest bending factor. From Eq. 3.53, one could conclude that the larger the angle β, the smaller the bending factor implying a more stable structure. However, one also sees that when $\beta = 90°$, $\sin\beta = 1$ and $\cos\beta = 0$, the nanorods lay horizontally on the surface and there is no bending at all. Theoretically this is the ideal structure, but practically as a sensor, this structure cannot significantly increase the actual surface area. For the other three aligned nanorod arrays, the zigzag nanorod array is the most stable structure. The vertical nanorods and the spring nanorods have similar bending factors. However, the actual length of the spring nanorods is much larger than the length of the straight nanorods. For some sensor applications, the actual surface area of the nanostructures plays a critical role. Thus, a better criteria for judging stability would be the bending factor per unit surface area, i.e., χ / A. For the straight, tilted, zigzag and spring nanorod array, since the deposition angle is fixed at 86°, which determines the density of the nanorods, the surface area A is proportional to the total length of the nanorods l. Therefore, the bending factor per unit length of the nanorod, χ/l, is a better criterion. Table I also lists the values of χ/l for the four different nanorod structures. Again, the tilted nanorod array is most stable. Compared to the vertical nanorod array, the zigzag and spring structures have also improved the stability for water treatment.

However, the above discussions are based on the assumption that the capillary force F and the effective area moment of inertia I_{eff} are independent of the nanorod height h or length l. In fact, the capillary force F depends on the shape that the contact line water makes with the nanorod, and I_{eff} depends on the effective radius of the structure. While due to the "fan-out" effect for GLAD, the diameter D of the nanorods increases monotonically from the bottom to the top as $D \propto l^{\alpha}$, where $\alpha \sim 0.24 - 0.34$ [91]. Thus, we have $F \propto D \propto l^{\alpha}$ and $I_{\text{eff}} \propto l^4 \propto l^{4\alpha}$. From Eq. 3.54, the length independent bending factor χ' can be expressed as

$$\chi' \propto \left(\frac{1-R^2}{h^{4-3\alpha}}\right)^{1/2}. \tag{3.55}$$

Since $4-3\alpha > 1$, Eq. 3.55 also gives a similar result that the previous conclusion that zigzag and spring nanorod arrays are the most stable nanorods among the three structures.

From the above analysis, although all the vertically aligned nanorod structures, vertical, zigzag and spring nanorod arrays, bundled together, the first two have shown improved stability over the third one. One could also use a numerical method such as finite element analysis, to further design and optimize stable aligned nanostructures with different topological shapes, and make the structures more suitable for sensor applications, or for sustaining liquid environments. This stability comparison demonstrated that the increase of the lateral size of a single nanorod by using zigzag or spring structure did reduce the bundling. It should also be noted that the tilting nature of the arms of these two structures may also reduce the bending. The reason for not eliminating the bundling could be that all zigzag or spring nanorod elements are in phase. This means that the joints of the arms in the same plane are still well separated. To completely overcome the nanocarpet effect, it is important to limit the spacing between nanorods in order to prevent large bending. We propose to deposit an extra layer of material into the nanorod channels in order to better support the nanorods and also make them stiffer by using a side wall coating. Since the nanorods fabricated by GLAD are not cylindrical in shape but rather they are in an inverted frustum array, in order to put a uniform layer of thin film in between the nanorods, the side angle of the inverted frustum is a very important design element in the deposition process. From the parameters measured from Figure 3.31(a), the side of nanorods forms an angle $\tan^{-1}[(128-33)/2/1190] \approx 2.3^{o}$ with the surface normal (note: this estimation is very rough, assuming the nanorod diameter is linearly broadening instead of power law [90,91]). In addition, the center of the nanorod gap has an average viewing angle $2\tan^{-1}((430-128)/2/1190) \approx 14.5^{o}$, as

sketched in Fig. 3.35(a). Ideally, to deposit a solid film uniformly covering the entire bottom, the deposition angle should satisfy $2.3^o < \theta < 7.3^o$ ($14.5^o/2$). In the experiment, we used a deposition angle of 3^o. Fig. 3.35(b) shows the result of applying a 100 nm Si film coating on Si nanorods 750 nm tall. The average nanorod diameter was 208 ± 17 nm and the separation was 253 ± 58 nm from the top- view SEM image. The inter-nanorod gap at top was 45 ± 9 nm, which was much smaller than the 302 nm gap for the nanorod array of 1.19 μm. The film coating also made the nanorod "head" larger (similar to a match stick), which was a result of the side wall growth (same as "fan-out" effect). From the top-view SEM (Fig. 3.35(c)), each nanorod had a big "head" almost touching its adjacent nanorods, and it appeared to be quite smooth. To test the stability of this structure, a water droplet was dispensed on the surface of the capped nanorods. After drying, no obvious watermark was observed. Figure 3.35(d) was a typical SEM image in the water invaded region. It was hard to tell any difference from Figure 3.35(c) and (d). Power spectra analysis (shown as insets) of Figure 3.35(c) and (d) confirmed that there was almost no structural change before and after applying the water droplet. The stabilization of the nanorods could be attributed to two facts: the first is the very small gap between the nanorods at their tops, which limits the space for nanorod bending. The second is the capping of shorter nanorod inside the channels, which provides additional support for the nanorod array. In fact, such short capped nanorods are observable in Fig. 3.35(b).

Although the mechanical stability of the nanorods has been improved significantly by the second layer deposition, for sensing applications, the porosity of the nanorods is still a key to characterizing the structure. In order to compare the porosity of the nanorods before and after the capping, we compared the fluorescence signal of fluorescein-5-isothiocyanate (FITC: Molecular Probe) attached to three different types of surfaces: flat Si substrate, Si nanorods, and capped Si

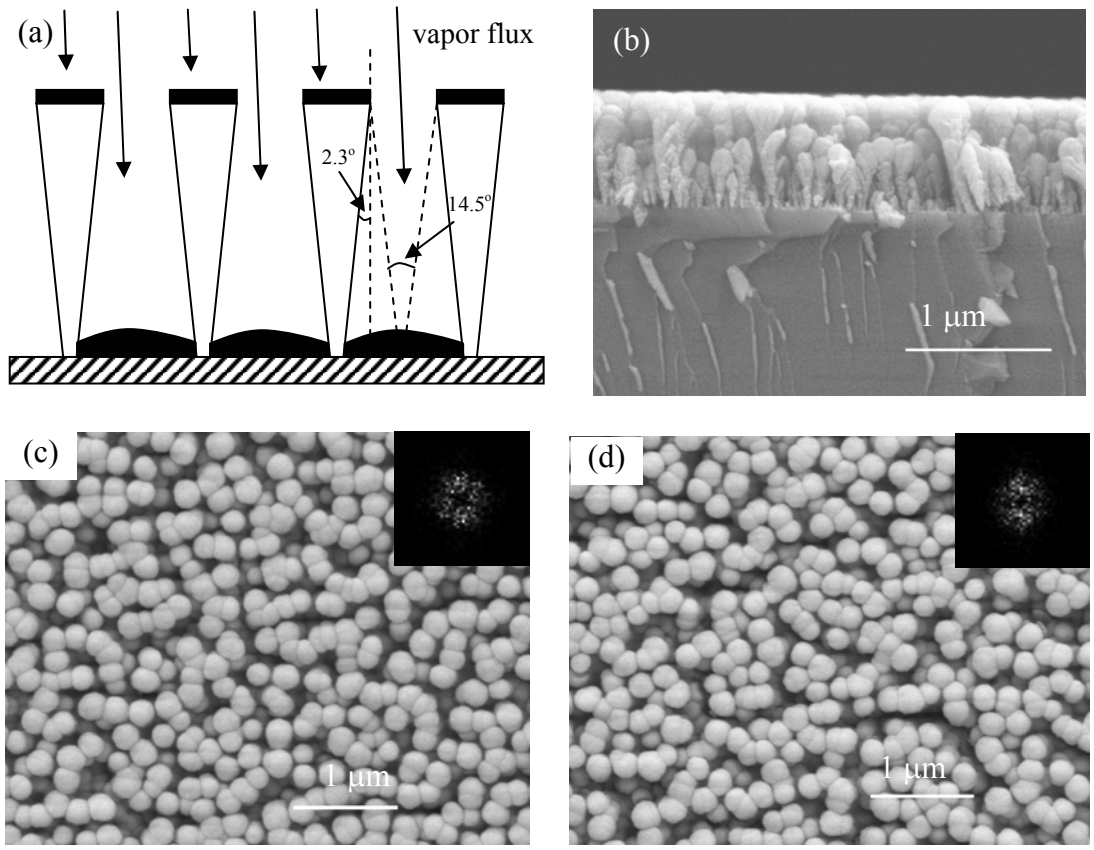

Figure 3.35. Capping the vertically aligned Si nanorod array: (a) a sketch of the film deposition scheme; The SEM (b) cross-sectional and (c) top-view images of the capped nanorods, and (d) SEM of the capped nanorods after water treatment. Insets in (c) and (d) are the corresponding power spectra of the SEM images.

nanorods. First these three samples were treated with an oxygen plasma for 10 minutes. Then they were immersed in a 2% 3-Aminopropyltriethoxysilane (APTES: Sigma)/Acetone solution at 45°C overnight so that the hydroxylated surfaces were coupled with the amine groups. By combining 1-Ethyl-3-[3-dimethylaminopropyl]carbodiimide Hydrochloride (EDC: Pierce) and *N*-hydroxysulfosuccinimide (Sulfo-NHS: Pierce), amine reactive Sulfo-NHS esters can be created on any carboxyl-containing molecule. Based on this principle, 19.2 mg EDC and 11.2 mg Sulfo/NHS were dissolved in 400 μL DI water and then mixed with 8 mg FITC which had been dissolved in 100 μL Dimethylsulfoxide (DMSO: Sigma). The mixture was magnetically stirred

for 30 minutes and then spread onto APTES-treated samples (250 μL for each). These samples were left under room temperature for one hour and then transferred to a 4°C refrigerator where they remained overnight. The above mentioned process immobilized the FITC dye onto the silica surfaces uniformly. The fluorescence was taken from a Typhon fluorescence Scanner (532nm excitation / 526nm short pass emission filter). The relative intensities were 3.0×10^6 for the Si film, 93.1×10^6 for the capped Si nanorods, and 163.7×10^6 for the Si nanorods (here the comparison is a little bit unfair since the Si nanorod is 1.92 μm, while the capped nanorod is 1.5 μm. Also, the capping layer partially blocks the fluorescence signal). From this result, it is seen that although the capped nanorod structure may lose a fraction of the porosity due to the coating of an extra layer, it still gives at least half of the fluorescence signal intensity compared to that from the original nanorod array. Moreover, the stability of this structure is undoubtedly a great advantage for repeated and reliable experimentation in liquid environments.

3.4.4 Conclusions

In summary, we have compared the stability of five GLAD structures: vertical, tilted, zigzag, square spring, and capped nanorod arrays after water treatment. The vertical, zigzag and square spring nanorod structures all suffer from the nanocarpet effect. Among them, the zigzag and spring structures are least affected, more mechanically stable. Despite the structural difference, the vertical and spring nanorod arrays bundle quite similarly. The zigzag structure bundles mostly in the deposition plane, which is a result of the "fan-out" effect. The tilted nanorod array shows anisotropic bending after water treatment but the tilted nanorods only bend towards the substrate without bundling. The bending may be reduced by using a two-phase rotation to make tilted nanorods with uniform diameter [124,125]. The coating of an additional

layer on the vertically aligned nanorod array effectively stabilizes the structure and maintains the overall porosity as confirmed by a fluorescence test. The loss of the fluorescence signal is due to the extra layer of Si. If we replace this layer with a transparent layer or anti-reflection layer, the signal will be stronger. Also the deposition angle of this film and the film thickness still need to be optimized.

CHAPTER 4.

THE DYNAMIC WETTING OF ALIGNED NANOROD ARRAYS

4.1 Spreading of water droplets on vertically aligned Si nanorod array surface [121]

4.1.1 Introduction

Spreading of liquids on solid surfaces has been studied extensively. Depending on the specific surface used, the spreading behavior of a liquid drop, such as water or silicon oil behaves differently. So far, most researches have focused on three types of surfaces: flat, rough and porous surfaces. On a flat surface, the radius of the contact line R(t) obeys a dynamic scaling law [112,126,127], $\pi R^2(t) \approx t^n \Omega^p$, where Ω is the volume of the liquid droplet. If $R < \kappa^{-1}$ ($\kappa^{-1} = \sqrt{\gamma/\rho g}$ is the capillary length), capillary is the main driving force and $n = 0.2$, $p = 0.6$; if $R > \kappa^{-1}$, gravity plays a more important role and $n = 0.25$, $p = 0.75$. Very often, a thin film precedes the apparent contact line during the spreading, which is called the precursor film. The width of the precursor front was found to follow the diffusion-like law, $\delta \propto t^{1/2}$ [127,128].

As a surface becomes rough, the spreading behavior for the surface changes. For random rough surfaces, Cazabat et al. [98] found four different scaling regimes with the power-law exponents of 1/4, 1/9, 0.50 and x ($0.32 < x < 0.34$). A precursor rim was observed and followed the diffusion law $\delta \propto t^{1/2}$. It was also shown that the normalized wetted area ($A/\Omega^{2/3}$) followed the relation $A/\Omega^{2/3} = k(t+\tau)^n$ [97], where k, τ and n are empirical constants determined from

best fit of experimental curves. The exponent n was found to be in the range of 0.20 to 0.55, depending strongly on the surface roughness.

For a porous surface, due to the penetration/transport of liquids into the porous structures, parameters such as the pore size, pore density, and permeability, become important. The spreading consists of two parts, the expansion of the contact line of the apparent droplet, and the evolution of a so-called stain due to the liquid penetrating the pores. It is believed that the stain evolution follows the classical Washburn equation [11], $\delta = \left(\frac{R_e \gamma \cos\theta}{2\mu} \right)^{1/2} \sqrt{t}$, where δ is the stain penetration length, R_e is the effective radius of the capillary, and μ is the viscosity of the liquid. Based on Darcy's law and the equation of continuity, Gillespie further modeled and tested the spreading of low vapor pressure liquids on filter paper and PrintFlex cards [129]. His results were later generalized by Kissa to the following scaling law [99], $A = K\left(\frac{\gamma}{\mu} \right)^{\nu} \Omega^m t^n$, where A is the area covered by a liquid stain and K is an empirical constant coefficient. Kissa has observed $\nu = 0.3$, $m = 0.7$, and $n = 0.3$, respectively, for n-alkanes spreading on paper and fabrics [99]. The dynamics of the apparent contact line has been modeled by Starov et al. on both saturated and dry thin porous films [130,131]. They found that during the capillary spreading stage, the radius of the contact line followed a power law $R \propto t^{0.1}$, which is the same as spreading on a dry solid substrate.

Recent investigations of the static wettability behavior of nanostructure films have revealed some very intriguing hydrophilic and hydrophobic properties [70]. Depending on the detailed structure, one can treat a nanostructured surface either as a rough surface or as a porous surface. It is interesting to know whether the spreading of a liquid droplet on these surfaces

follows a similar dynamic scaling law as a rough or porous surface. In this section, we investigate the spreading law of water on silicon nanorod array surfaces, and show that the nanorod height does not affect the spreading exponents.

4.1.2 Experiment

Vertically aligned silicon nanorod arrays with different heights were prepared on glass substrates by GLAD. The deposition angle was 86°. The spreading experiments were performed by a modified contact angle measurement system (Fig. 4.1(a)). Water drops were dispensed onto the nanorod sample *S* through a computer controlled syringe and syringe pump *P* (Hamilton; 250 μl). CCD camera *C* (210 frame per second (fps) at VGA mode) monitors the drop diameter. To

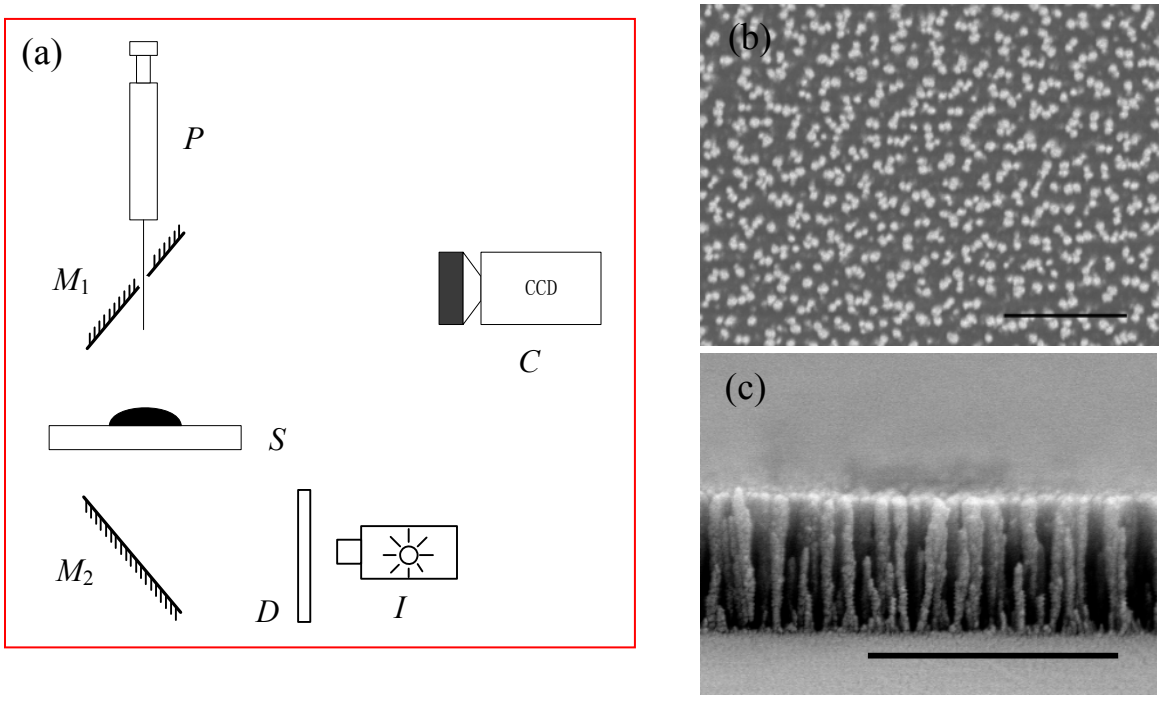

Figure 4.1. (a) Sketch of the experimental setup: M_1, M_2 are mirrors, *S* is the sample, *I* is an illuminating source, *C* is a fast CCD camera with a camera lens, *P* is a syringe and *D* is a diffuser. (b) The top-view and (c) the cross-section SEM of the silicon nanorod sample. The scale bar is 2 μm.

allow the dispensing of water from the syringe while monitoring the liquid drop, an aperture with a diameter ~ 2 mm was opened in the center of mirror M_1. The stainless steel needle of the syringe was replaced with a polyimide coated capillary tube with 191 μm OD and 101 μm ID to minimize the scattering of light. Spreading videos were recorded by XCAP software (EPIX, Inc.). During the experiment, the temperature was ~ 25°C and the humidity was ~ 23%.

4.1.3 Results and discussion

Figure 4.1(b) and (c) show typical top-view and cross-sectional SEM images of the silicon nanorod sample. The morphological parameters obtained from the SEM images are: the average diameter of the nanorods on the top is d_t = 133 ± 34 nm, the average rod-rod separation is L = 280 ± 106 nm, and the average nanorod height is h = 1106 ± 104 nm. For the spreading

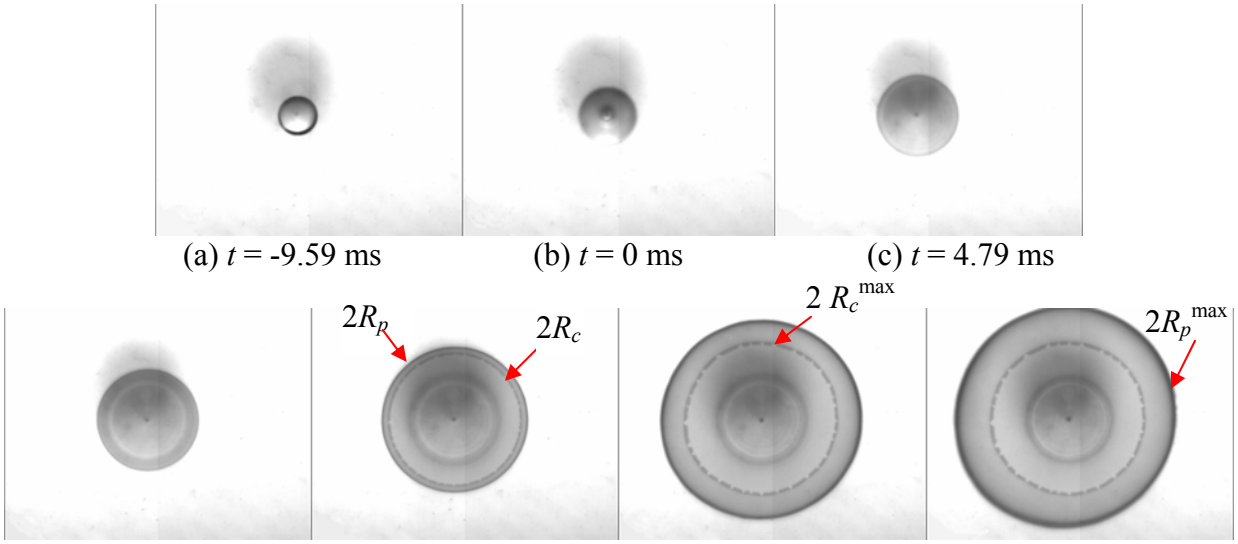

Figure 4.2. Snapshots of the spreading video at t = -9.59 ms, 0 ms, 4.79 ms, 23.97 ms, 383.51 ms, 3355.71 ms and 11026.89 ms. In the late stage of the spreading, one can clearly observe the three-phase contact line and the precursor front.

measurement, a 3-μL water drop was dispensed onto the freshly prepared sample surface with a very slow approaching speed to minimize the impact effect. The video recording was started manually right before the contact. Figure 4.2 shows the snapshots of a water droplet spreading on the above mentioned Si nanorod surface. At t = -9.59 ms, the water drop was right above the sample surface. At $t = t_{c0}$ = 0 ms (defined as the start point of the spreading: the maximum error for the time is the sampling interval 1/frame rate = 4.79 ms), the drop touched the sample surface, and at t = 4.79 ms, the water drop fully settled down onto the surface. The contact line of the droplet spread further till at $t = t_{p0}$ = 23.97 ms, an additional rim, which is called the precursor rim, visually appeared ahead of the apparent contact line. But the precursor rim was so close to the contact line that it was hard to distinguish. After further spreading, at t = 383.51ms, the precursor rim advanced well ahead of the contact line. Both the diameters of the contact line and the precursor rim increased with time till $t = t_c$ = 3355.71 ms, when the contact line reached a

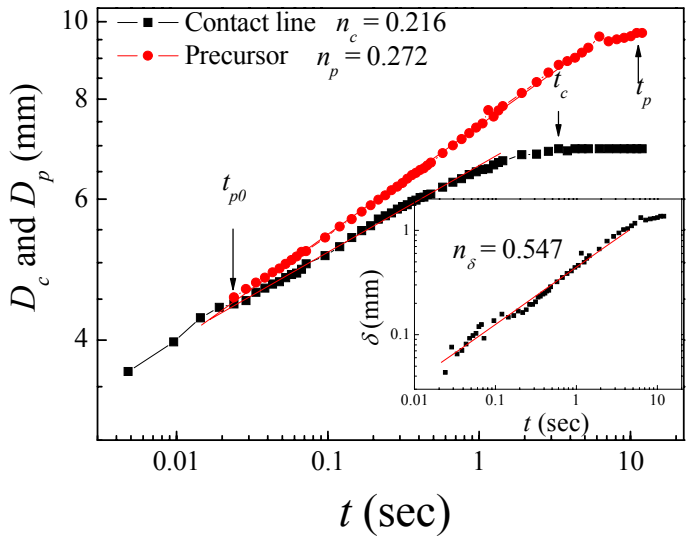

Figure 4.3. Diameters of the contact line and precursor as a function of time plotted in log-log scale. Insert showing the precursor length evolves with time.

maximum. The precursor rim continued to expand, and at $t = t_p$ = 11026.89 ms reached its maximum. From these snapshots, it was found that both the contact line and the precursor rim were almost circular. Thus, the spreading was uniform and isotropic, from which it can be inferred that the nanorod surface was uniform and isotropic. The diameters of the contact line D_c and the precursor rim D_p averaging over two perpendicular directions were measured as a function of spreading time, and were plotted on log-log scale in Fig. 4.3. At small t, both D_c and D_p exhibited a dynamic scaling behavior, $D \propto t^{n/2}$. Specifically, for the contact line, the power law fitting gives an exponent $n_c = 0.216 \pm 0.006$, and for the precursor rim, $n_p = 0.272 \pm 0.006$. The exponent n_c for the contact line falls in the range of the spreading on a rough or porous surface. According to Starov et al, this exponent is a result of capillary driven spreading due to the contact line moving on the pre-wetted surface (smooth) formed by the precursor rim [130,131]. The precursor rim is similar to the stain formed on a porous surface. However, the exponent n_p is smaller than that (n = 0.3) for a porous surface [99], but larger than that (~ 0.25) for a rough surface (in the capillary regime) [98]. Since there are many nanochannels within the Si nanorod array, the possible reason for the precursor rim formation is the capillary spreading inside the channels. Therefore, the Washburn equation should hold for the advancing of the precursor rim with respect to the contact line. The inset in Fig. 4.3 is the log-log plot of $\delta = D_p - D_c$, the distance between the diameter of the precursor rim and the contact line. It appears that δ also follows a power law, $\delta \propto t^{n_\delta}$, with n_δ = 0.547 ± 0.003 for t < 6232.02 ms, which is consistent with the Washburn equation.

From the above discussions, the spreading of the contact line roughly can be divided into four different stages according to the changes of the precursor and the contact line:

Stage I: $t_{c0} < t < t_{p0.}$ In this very early stage of spreading, no precursor rim is observed, and several factors such as inertia and drop shape relaxation could be important [131]. However, the diameter of the contact line can be fitted by the same dynamic scaling law as for the next stage, which suggests that the spreading at this stage is predominantly capillary driven, or the effects other than the capillary force may be negligible.

Stage II: $t_{p0} < t < t_c$. This is a capillary driven spreading stage, both for the contact line and the precursor rim. In this stage, the apparent drop acts as a reservoir for the precursor rim to penetrate the nanorod channels in advance, while itself spreads on the pre-wetted nanochannel surface. For the spreading of liquids on saturated thin porous films, Starov et al. have derived that the spreading of the contact line follows a complicated power law $D_c = D_0\left(1 + t/t_0\right)^{n_c/2}$, where t_0 is the starting time for the spreading [130]. The fitting of this function by the data in Fig. 4.3(a) gives D_0 = 3.387 mm, t_0 = 2.14 ms, and $n_c = 0.216$. However, since t_0 is so small, the dynamics of D_c is dominated by the power law $D_c \approx D_0\left(t/t_0\right)^{n_c/2}$. In the late part of this stage, the spreading of D_c tends to slow down possibly owing to the increasing transport of water from the apparent drop to the precursor film. Evaporation may not be considered so far since this stage only lasts about 3 seconds. In this stage, the penetration of the nanochannel by the precursor rim obeys the Washburn equation.

Stage III: $t_c < t < t_p$. In this stage, D_c reaches its maximum while D_p increases further till it reaches its maximum. This implies that the draining rate of water from the apparent drop into the nanochannels is increasing since the precursor rim is enlarging. Thus one would expect to see water spread over the entire surface while the apparent droplet volume (the height and the apparent contact line) shrinks. This is true for a non-volatile liquid like poly (dimethyl siloxane) (PDMS). We found the PDMS precursor film covers the entire nanorod surface after several

hours. However, for water, D_p reaches a maximum shortly after the contact line does. Thus evaporation must play an essential role for this stage. When the precursor increases, the surface area also increases, and hence so does the evaporation rate. The spreading process can be thought as a competition between the spreading and evaporation.

Stage IV: $t > t_p$. Both the contact line and the precursor reach their maxima, and after certain time the contact line starts to recede due to droplet evaporation.

A phenomenon that must not be ignored in the spreading of liquids on nanostructured surface is the so called nanocarpet effect, which is the bundling of nanorods during the spreading/drying process. This bundling provides an extra path for energy dissipation. To understand fully this phenomenon, one should consider all the effects including the capillary driving force, the transport of liquid in between the apparent drop and the precursor film, evaporation and mechanical dissipation through nanorod bundling.

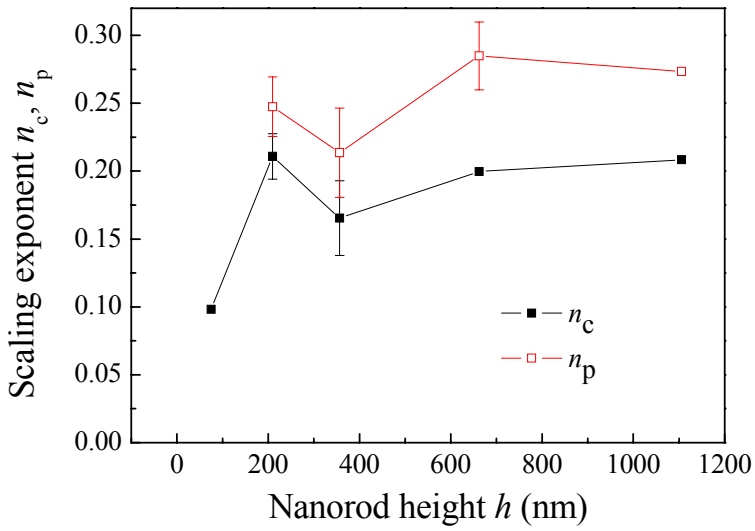

Figure 4.4. The relationship of the scaling exponents of the contact line and precursor with the nanorod height h.

Finally, to examine whether the exponents n_c and n_p are universal for nanorod surfaces, the spreading of water droplets on Si nanorod surfaces with different heights were carried out, and the obtained dynamic exponents n_c and n_p are plotted as a function of the nanorod height in Fig. 4.4. From Fig. 4.4, one can obtain three common trends: (1) The precursor rim was always ahead of the contact line; (2) $n_p > n_c$ for all nanorod heights (no precursor was observed for h = 75.1 nm); (3) except for very small height (h = 75.1 nm, n_c = 0.098), $n_c \sim 0.2$ while $n_p \sim 0.24 - 0.28$. This means both exponents n_c and n_p are universal for nanorod arrays with different heights.

4.2 Capillary rise on aligned nanorod array surfaces

In this section, we study the capillary rise of water on aligned Si nanorod array surfaces to examine the applicability of those scaling relationships for liquid transport in capillary tubes or porous media. In addition, we compare the dynamic behaviors of the precursor and contact line to those in the spreading process presented above.

4.2.1 Experiments

Two sets of surfaces were tested for the capillary rise: flat and nanorod array surfaces. The flat surfaces were pre-cleaned microscope cover slides (Gold Seal) cut into 1 × 2.54, 2 × 2.54, and 3 × 2.54 cm^2. Before the capillary rise experiment, they were immersed in piranha solution (sulfuric acid : hydrogen peroxide 4 : 1 heated to 70 ^oC) for 30 minutes followed by thorough DI water rising and compressed N_2 drying. The Si nanorod array surfaces were prepared by GLAD. The substrates for growing the nanostructures were the same microscope

cover slides cut into the three sizes specified above and were cleaned by the same piranha method. The nanorod samples were fabricated in a custom-made e-beam evaporation system with a base pressure of 1.0×10^{-6} Torr. The deposition angle for the Si nanorods was 86^{o}. During the nanorod deposition, the substrate was continuously rotated azimuthally with a rotation speed of 0.5 revolution/second. The nominal Si film deposition rate was 0.4 nm/second and the final nominal film thickness was 3 μm monitored by QCM. The nanorod structure was examined by SEM. The set-up for measuring the capillary rise is shown in Fig. 4.5. The sample was able to be moved vertically up and down at variable speed controlled by an electronic motor. The rectangular glass container was first treated with HFTS to render its inner wall hydrophobic and then it was filled partially with DI water. The glass surface treated with HFTS has a water contact angle of about 110^{o}, thus water does not climb on the inner wall of the container and will not interfere with the recording of the capillary rise. A fast CCD camera (210 frame per second at 800 × 600 resolution) was used to monitor the capillary rise. The video was recorded with

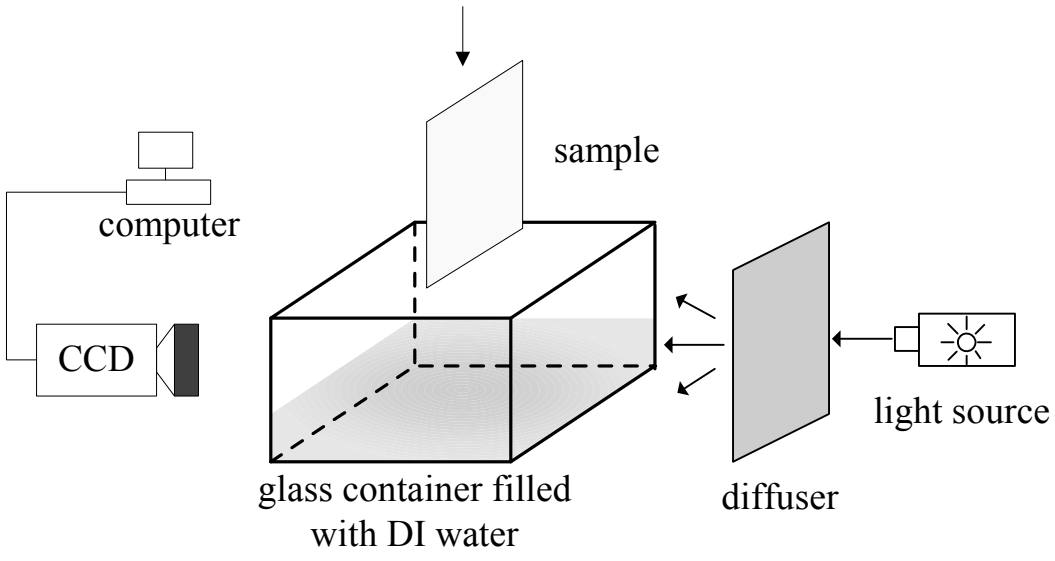

Figure 4.5. Sketch of the experimental set-up for recording the capillary rise.

Xcap software. Before immersing a sample into the water bath, it was positioned approximately 1 mm above the surface. The sample was then brought towards the water surface with a speed of ~ 0.25 mm/second and the CCD camera was triggered immediately to allow the full recording of the capillary rise process. The first frame of water-sample contact was determined by examining the recorded video. When changing sample size, spacers were either inserted or removed between the camera lens and the CCD to make the sample image occupy at least 4/5 of the horizontal size of a frame. Calibration between the image pixels and the real sample size was carried out for each measurement.

4.2.2 Results and discussions

4.2.2.1 Capillary rise on flat substrates

Figure 4.6 shows some snap-shots of the water rising on a flat microscope slide with lateral length (width) of 1 cm. At an early stage, e.g. t = 9.6 ms, only part of the sample bottom contacts with water. Practically, for a macroscopic sample, this kind of non-uniform contact is unavoidable. After aligning the sample many times, we find that the contact either starts at the left or right corner or in the middle, but the entire bottom never contacts the water simultaneously. At a later stage, e.g. t = 19.2 ms, the invading front (or the three-phase contact line) gradually flattens.

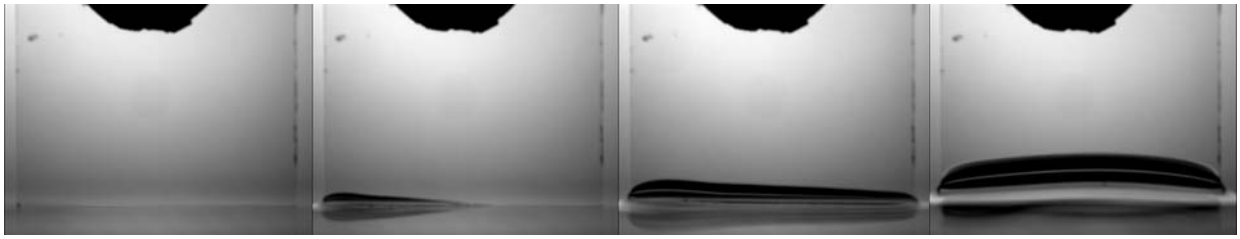

t = 0 ms, t = 9.6 ms, t = 19.2 ms, t = 67.1 ms

Figure 4.6. Snap-shots showing the evolution of the capillary rise

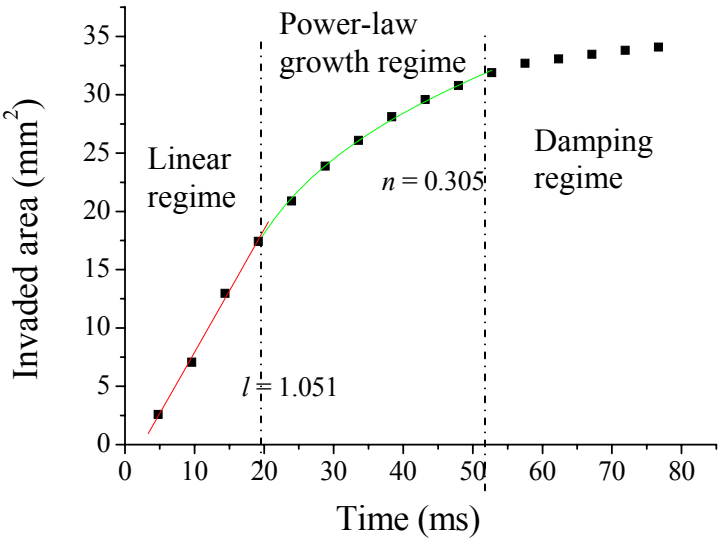

Figure 4.7. Plot of the evolution of water covered area with time on the flat microscope slide.

Finally at t = 67.1 ms, the invading front becomes quite uniform in the central part. This is the result of the interplay of the viscous force, the contact line relaxation, and the hydrostatic leveling effect. However, at the edge of the sample, the contact line remains curved. Since the contact line changes its shape during the invading process, it is inappropriate to use the contact line height to characterize the invading dynamics as for a capillary tube. Therefore, we attempted to examine the evolution of the water covered area A, since it reflects the surface free energy change. In Fig. 4.7, the plot of area A vs. t shows several distinct regimes. Linear regime: at t < 19.2 ms, the invaded area has a linear relationship with t (the solid line for the first 4 data points is from the linear fitting). Power-law growth regime: after 19.2 ms, the data follows a parabola. We use a power law expression

$$A = C(t - t_0)^n \tag{4.1}$$

to fit the data, where C is a fitting coefficient, t_0 is the initial time for the starting of the power law growth, and n is the scaling exponent. For 19.2 ms < t < 52.7 ms, the data can be perfectly fitted (fitting quality R^2 = 0.999) by Eq. 4.1 as indicated by the solid curve in Fig. 4.7. Damping regime: beyond 52.7 ms, the data deviate from what Eq. 4.1 predicts. At t = 52.7 ms, the contact line height is ~ 3.2 mm, which is larger than the water capillary length $\kappa^{-1} = \sqrt{\gamma / \rho g}$ = 2.7 mm. Thus the hydrostatic force effect can not be neglected at this stage, which damps the invading. The linear fitting slope in the early stage is l = 1.051 mm^2/ms, which is also the invading rate. The power law fitting gives an exponent n = 0.305 for the stage followed. The capillary rise is repeated three times and the average value for the linear slope is l_1 = 0.925 ± 0.110 mm^2/ms, and the average scaling exponent is n_1 = 0.346 ± 0.041.

To examine whether the sample size affects the scaling relationships, we further compare the capillary rise on micro slides with width of 2 cm and 3 cm. The linear, power-law growth and damping regimes are observed in each case. The exponents are found to be l_2 = 1.808 ± 0.121 mm^2/ms, n_2 = 0.318 ± 0.059 for 2 cm samples and l_3 = 2.762 ± 0.304 mm^2/ms, n_3 = 0.297 ± 0.008 for 3 cm samples. It is seen that with increasing slide width, the slope for the linear regime increases. This linear regime should have a similar origin as that of the inertial regime of capillary rise in capillary tubes [132-134]. At the same time, the power-law growth exponent decreases with increasing sample width.

4.2.2.2 Capillary rise on nanostructured surface

The top and cross-sectional views of the Si nanorod structures were shown previously in Fig. 3.31(a). The nanorods are all vertically aligned and uniformly distributed over a large area. The average nanorod height is 1.2 μm, the average nanorod diameter near top is 128 nm, and the

t = 4.8 ms, t = 47.9 ms, t = 143.8 ms, t = 11984.7 ms

Figure 4.8. Snapshots of water rise on the Si nanorod array surface.

average rod-rod separation is 430 nm. This nanorod structure is completely wettable by water. When the sample is in contact with water, a capillary rise similar to those of the flat micro slides is observed at early stages. However, at later stages a precursor film is observed to advance ahead of the contact line. The capillary rise process is illustrated by several snapshots in Fig. 4.8. This observation is similar to what we have observed for a water droplet spreading on a horizontal nanostructured surface. However, the difference is that in this capillary rise, the contact line does not advance anymore when the precursor appears, or it simply oscillates near an equilibrium height as shown in a semi-log plot in Fig. 4.9. The oscillation is caused by the interplay of inertial and gravity for liquids of low viscosity, and the details have been discussed by Lorenceau and Quere [135].

Figure 4.10 shows the evolution of the invaded area for the 1 cm wide nanorod sample. The inertial, power-law growth and damping regimes are also identified. The slope for the linear regimes is l_{NR1} = 0.699 ± 0.061 mm^2/ms, averaged over 3 measurements. This slope is smaller than the counterpart for a flat micro slide. This is due to the water penetrating into the nanorod channels or the sticking from the nanorods. After the inertial regime, the capillary rise follows a power law growth, with the exponent n_{NR1} = 0.354 ± 0.011. The corresponding slopes and exponents are l_{NR2} = 0.856 ± 0.207 mm^2/ms, n_{NR2} = 0.413 ± 0.063 for 2 cm sample and l_{NR3} =

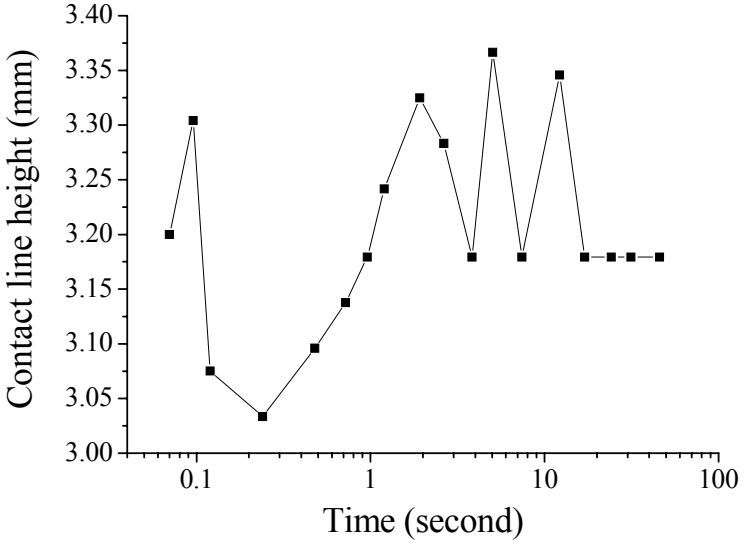

Figure 4.9. Oscillation of the contact line

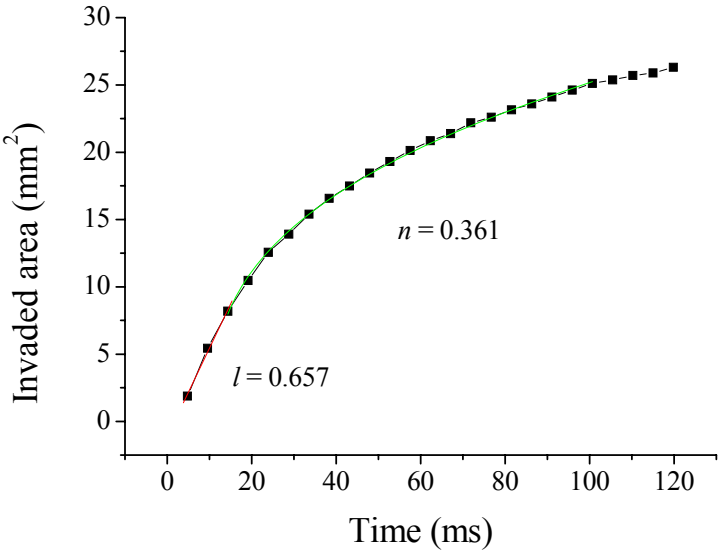

Figure 4.10. Plot of the invaded area vs. time for Si nanorod sample of 1 cm wide. The solid curves represent a linear fitting and a power-law fitting, with the slope l and scaling exponent n labeled.

2.074 ± 0.187 mm^2/ms, n_{NR3} = 0.507 ± 0.023 for 3 cm sample. The general trend is with Increasing sample width, the invading rate for the inertial regime increases, and the scaling exponents for the power-law growth regime also increases, which is opposite to the trend on the flat surface.

The evolution of the precursor film is plotted in Fig. 4.11 for the 1 cm wide nanorod sample. In this plot, the precursor film length is measured instead of the area since the shape of the precursor and contact line fronts are already fully developed. Data fitting using Eq. 4.1 reveals that at early stage of the precursor penetrating inside the nanorod channels, the precursor length follows a power law growth, with exponent n_{p1} = 0.517 ± 0.064. For 2 cm and 3 cm wide samples, the scaling exponents are n_{p2} = 0.477 ± 0.011, n_{p3} = 0.468 ± 0.015, respectively. These values are very close to the $t^{1/2}$ law predicted by the Washburn's equation.

We are currently developing the theoretical interpretations on the above results.

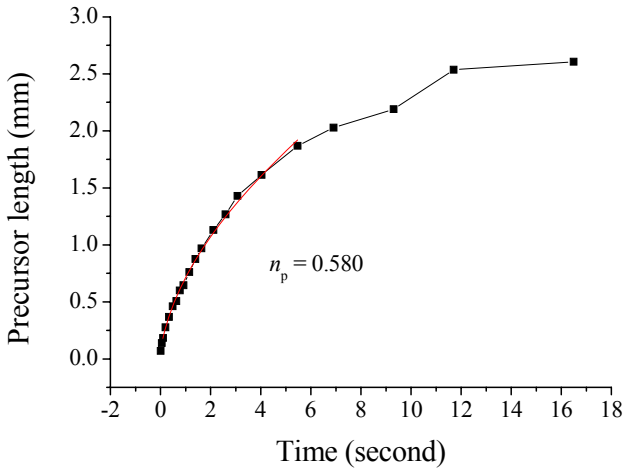

Figure 4.11. Plot of precursor with time for the 1 cm wide Si nanorod sample. The data at t < 6s are fitted with a power law and the exponent is labeled.

4.3 Conclusion

In this chapter, we have studied the dynamic spreading and capillary rise of water on nanostructured surfaces. Due to the effective lubrication of a precursor film in the nanorod channels, the spreading is very similar to that on a flat surface. The precursor evolution follows Washburn's law. These behaviors are almost unaffected by the height of the nanorods. However, scaling relationships for the capillary rise on nanostructured surfaces are more complicated and the data interpretation is not complete yet. We predict that the gravity effect will be significant, since a relatively large amount of water is attracted above the water surface.

CHAPTER 5.

CONCLUSIONS AND FUTURE WORK

In this dissertation, I have used the glancing angle deposition technique to fabricate various aligned nanorod arrays and performed a systematic study on the wettability of aligned nanorod surfaces.

The static wettability of the Si nanorod array surfaces was investigated by the sessile drop method. The contact angle was successfully tailored from superhydrophilic to superhydrophobic by controlling the nanorod height, rod-rod separation, and chemical treatment. Wetting transitions between different regimes were identified and different models like the Wenzel's law and Cassie's law were successfully applied to explain the phenomena.

In the contact angle experiment, a nanocarpet effect is discovered, which is the bundling of nanorods during the wetting/dewetting process. I have carried out a very detailed characterization of this effect and tried to understand it both theoretically and experimentally. For example, I considered the total free energy minimization to estimate the nanorod bundle size and used a cryo-SEM experiment to investigate whether the bundling happened in the spreading or the drying process. The nanocarpet effect is undesirable for many practical applications because of the significant change in the structure. In order to minimize the nanocarpet effect, I have compared the mechanical stability of five nanorod array structures and found that by

designing complicated tilting structures or by coating a capping layer, the structures could be stabilized while the high porosity was maintained.

I have also investigated the dynamic spreading of water droplets on vertically aligned silicon nanorod arrays. The purpose was to compare the spreading behavior of water droplets on aligned nanorod surfaces to conventional flat, rough, and micro porous surfaces. I used a fast CCD camera to record the process. A precursor film was observed to evolve in the nanorod channels and the scaling of both the contact line and the precursor followed power laws. Specifically, the contact line evolved as if on a flat surface, while the precursor film length evolution followed the classic Washburn's law for describing the penetration depth of liquids in capillary tubes. I have also experimentally observed the capillary rise of water on nanostructured surfaces. The scaling relationships appeared to be more complicated than those of the spreading process.

In the future, it will be of interest to further the wettability study into several areas: one is to investigate the real-time control over the wettability, using methods like electric field, light illumination or chemical reaction; the second is micro/nano-fluidics, investigating how liquid transport occurs in nanochannels, both sealed and open ones, and examining factors that affect the dynamics. It is also important to better understand the nanocarpet effect. Some experiments can be envisioned such as *in situ* environmental SEM observation of water condensation and droplet coalescence on nanostructured surfaces, and polymer droplet curing on nanorod surfaces followed by SEM examination. For the capillary rise, the current difficulty in theoretically understanding the process is caused partially by the existence of the boundaries, which caused the triple line to be non-uniform. If we can incorporate nanostructures into the inner wall of a cylindrical tube, the symmetry will be much improved and gravity may be ignored if the tube

diameter can be made very small. Or we can study the capillary rise on a cylindrical fiber coated with nanorods (this is already realized), so that the meniscus will be more uniform while the gravity effect will still be significant.

REFERENCES

[1] T. Young, Philos. Trans. R. Soc. London **1805**, *95*, 65.
[2] R. N. Wenzel, Ind. Eng. Chem. **1936**, *28*, 988.
[3] A. B. D. Cassie and S. Baxter, Trans. Faraday Soc. **1944**, *40*, 546.
[4] W. Barthlott and C. Neinhuis, Planta **1997**, *202*, 1.
[5] J. Bico, C. Tordeux, and D. Quere, Europhysics Letters **2001**, *55*, 214.
[6] D. Quere, Rep. Prog. Phys. **2005**, *68*, 2495.
[7] J. Bico, C. Marzolin, and D. Quere, Europhysics Letters **1999**, *47*, 220.
[8] A. Marmur, Langmuir **2003**, *19*, 8343.
[9] M. Miwa, A. Nakajima, A. Fujishima, K. Hashimoto, and T. Watanabe, Langmuir **2000**, *16*, 5754.
[10] R. Lucas, Kolloid Z. **1918**, *23*, 15.
[11] E. W. Washburn, Phys. Rev. **1921**, *17*, 273.
[12] A. Nakajima, K. Hashimoto, and T. Watanabe, Monatsh. Chem. **2001**, *132*, 31.
[13] M. L. Ma and R. M. Hill, Curr. Opin. Colloid Interf. Sci. **2006**, *11*, 193.
[14] H. J. Li, X. B. Wang, Y. L. Song, Y. Q. Liu, Q. S. Li, and L. Jiang, Angew. Chem. Int. Ed. **2001**, *40*, 1743.
[15] L. Feng, S. H. Li, Y. S. Li, H. J. Li, L. J. Zhang, J. Zhai, Y. L. Song, B. Q. Liu, L. Jiang, and D. B. Zhu, Adv. Mater. **2002**, *14*, 1857.
[16] X. F. Gao and L. Jiang, Nature **2004**, *36*, 432.
[17] S. H. Li, H. J. Li, X. B. Wang, Y. L. Song, Y. Q. Liu, L. Jiang, and D. B. Zhu, J. Phys. Chem. B **2002**, *106*, 9274.
[18] X. Y. Lu, C. C. Zhang, and Y. C. Han, Macromol. Rapid Commun. **2004**, *25*, 1606.
[19] L. zhai, F. C. Cebeci, C. R. E., and R. M. F., Nano Lett. **2004**, *4*, 1349.
[20] L. Jiang, Y. Zhao, and J. Zhai, Angew. Chem. Int. Ed. **2004**, *43*, 4338.
[21] X. Zhang, F. SHi, X. Yu, H. Liu, Y. Fu, Z. Q. Wang, L. Jiang, and X. Y. Li, J. Am. Chem. Soc. **2004**, *126*, 3064.
[22] J. T. Han, J. Y., D. Y. Lee, J. H. Park, S. H. Song, D. Y. Ban, and K. Cho, J. Mater. Chem. **2005**, *15*, 3089.
[23] M. H. Jin, X. J. Feng, J. M. Xi, J. Zhai, K. W. CHo, L. Feng, and L. Jiang, Macromol. Rapid Commun. **2005**, *26*, 1805.
[24] M. H. Sun, C. X. Luo, L. P. Xu, H. Ji, O. Y. Qi, D. P. Yu, and Y. Chen, Langmuir **2005**, *21*, 8978.
[25] X. J. Feng, J. Zhai, and L. Jiang, Angew. Chem. Int. Ed. **2005**, *44*, 5115.
[26] L. Jiang, Y. Zhao, and J. Zhai, Angew. Chem. Int. Ed. **2004**, *43*, 4338.
[27] L. Zhai, F. C. Cebeci, R. E. Cohen, and M. F. Rubner, Nano Lett. **2004**, *4*, 1349.
[28] N. Zhao, J. Xu, Q. D. Xie, L. H. Weng, X. L. Guo, X. L. Zhang, and L. H. Shi, Macromol. Rapid Commun. **2005**, *26*, 1075.

[29] D. Nystrom, J. Lindqvist, E. Ostmark, A. Hult, and E. Malmstrom, Chem. Commun. **2006**, 3594.
[30] Y. H. Yang, Z. Y. Li, B. Wang, C. X. Wang, D. H. Chen, and G. W. Yang, J. Phys.: Condens. Matter **2005**, *17*, 5441.
[31] E. Bormashenko, T. Stein, G. Whyman, Y. Bormashenko, and R. Pogreb, Langmuir **2006**, *22*, 9982.
[32] H. E. Jeong, S. H. Lee, J. K. Kim, and K. Y. Suh, Langmuir **2006**, *22*, 1640.
[33] L. B. Zhu, Y. H. Xiu, J. W. Xu, P. A. Tamirisa, D. W. Hess, and C. P. Wong, Langmuir **2005**, *21*, 11208.
[34] L. C. Gao and T. J. McCarthy, Langmuir **2006**, *22*, 2966.
[35] D. H. Xu, H. Liu, L. Yang, and Z. G. Wang, Carbon **2006**, *44*, 3226.
[36] R. H. Dettre and R. E. Johnson, Adv. Chem. Ser. **1964**, *43*, 136.
[37] E. Martines, K. Seunarine, H. Morgan, N. Gadegaard, C. D. W. Wilkinson, and M. O. Riehle, Nano Lett. **2005**, *5*, 2097.
[38] K. K. S. Lau, J. Bico, K. B. K. Teo, M. Chhowalla, G. A. J. Amaratunga, W. I. Milne, G. H. McKinley, and K. K. Gleason, Nano Letters **2003**, *3*, 1701.
[39] R. Furstner, W. Barthlott, C. Neinhuis, and P. Walzel, Langmuir **2005**, *21*, 956.
[40] H. M. Shang, Y. Wang, S. J. Limmer, T. P. Chou, K. Takahashi, and G. Z. Gao, Thin solid films **2005**, *472*, 37.
[41] G. Gu, H. Dang, Z. Zhang, and Z. Wu, Appl. Phys. A **2006**, *83*, 131.
[42] C. H. Su, J. Li, H. B. Geng, Q. J. Wang, and Q. M. Chen, Appl. Surf. Sci. **2006**, *253*, 2633.
[43] G. R. J. Artus, S. Jung, J. Zimmermann, H. P. Gautschi, K. Marquardt, and S. Seeger, Adv. Mater. **2006**, *18*, 2758.
[44] M. Kemell, E. Farm, M. Leskela, and M. Ritala, Phys. Stat. Sol. A **2006**, *203*, 1453.
[45] J. Fresnais, J. P. Chapel, and F. Poncin-Epaillard, Surf. Coat. Technol. **2006**, *200*, 5296.
[46] Y. Liu, L. Mu, B. H. Liu, and J. L. Kong, Chem. Eur. J. **2005**, *11*, 2622.
[47] A. Kundt, Ann. Phys. Chem. Lpz. **1886**, *27*, 59.
[48] D. O. Smith, M. S. Cohen, and G. P. Weiss, J. Appl. Phys. **1960**, *31*, 1755.
[49] D. O. Smith, J. Appl. Phys. **1959**, *30*, 264S.
[50] T. G. Knorr and R. W. Hoffmann, Phys. Rev. **1959**, *113*, 1039.
[51] L. Holland, *Vapor Deposition of Thin Films*. (Wiley, New York, 1956).
[52] L. Holland, J. Opt. Soc. Am. **1953**, *43*, 376.
[53] H. Kronig and G. Helwig, Optik **1950**, *6*, 111.
[54] J. M. Nieuwenhuizen and H. B. Haanstra, Philips Tech. Rev. **1966**, *27*, 87.
[55] N. Kaiser, Appl. Opt. **2002**, *41*, 3053.
[56] M. Ohring, *The Materials Science of Thin Films*. (Academics Press, Toronto, 2002).
[57] K. Robbie, L. J. Friedrich, S. K. Dew, T. Smy, and M. J. Brett, J. Vac. Sci.Technol. A **1995**, *13*, 1032.
[58] K. Robbie, M. J. Brett, and A. Lakhtakia, J. Vac. Sci. Technol. A **1995**, *13*, 2991.
[59] B. Dick, M. J. Brett, and T. Smy, J. Vac. Sci. Technol. B **2003**, *21*, 2569.
[60] A. W. Adamson and A. P. Gast, *Phys. Chem. Surf.*, 6th ed. (Wiley, New York, 1997).
[61] A. Kawai and H. Nagata, Jpn. J. Appl. Phys. **1994**, *2*, L1283.
[62] W. Chen, A. Y. Fadeev, M. C. Hsieh, D. Oner, J. Youngblood, and T. J. McCarthy, Langmuir **1999**, *15*, 3395.
[63] D. Oner and T. J. McCarthy, Langmuir **2000**, *16*, 7777.
[64] J. Bico, C. Marzolin, and D. Quere, Europhys. Lett. **1999**, *47*, 220.

[65] S. Herminghaus, Europhys. Lett. **2000**, *52*, 165.
[66] J. Bico, C. Tordeux, and D. Quere, Europhys. Lett. **2001**, *55*, 214.
[67] T. N. Krupenkin, J. A. Taylor, T. M. Schneider, and S. Yang, Langmuir **2004**, *20*, 3824.
[68] L. Feng, S. H. Li, H. J. Li, J. Zhai, Y. L. Song, L. Jiang, and D. B. Zhu, Angew. Chem. Int. Ed. **2002**, *41*, 1221.
[69] B. Muller, M. Riedel, R. Michel, S. M. De Paul, R. Hofer, D. Heger, and D. Grutzmacher, J. Vac. Sci. Technol. B **2001**, *19*, 1715.
[70] J.-G. Fan, X.-J. Tang, and Y.-P. Zhao, Nanotechnology **2004**, *15*, 501.
[71] P. Meakin, *Fractals, Scaling, and Growth Far from Equilibrium*. (Cambridge University Press, Cambridge, 1998).
[72] Y.-P. Zhao, G.-C. Wang, and T.-M. Lu, *Characterization of Amorphous and Crystalline Rough Surface-Principles and Applications (Experimental Methods in the Physical Sciences Vol 37)*. (Academic, New York, 2001).
[73] J. T. Drotar, Y. P. Zhao, T. M. Lu, and G. C. Wang, Phys. Rev. B **2000**, *62*, 2118.
[74] J. H. Yao and H. Guo, Phys. Rev. E. **1993**, *47*, 1007.
[75] G. Wolansky and A. Marmur, Colloid Surf. A **1999**, *156*, 381.
[76] J. Bico, U. Thiele, and D. Quere, Colloid Surf. A **2002**, *206*, 41.
[77] R. E. Johnson and R. H. Dettre, Adv. Chem. Ser. **1964**, *43*, 112.
[78] H. Tada and H. Nagayama, Langmuir **1994**, *10*, 1472.
[79] S. Shibuichi, T. Yamamoto, T. Onda, and K. Tsujii, J. Colloid Interf. Sci. **1998**, *208*, 287.
[80] J. J. Steel and M. J. Brett, J. Mater. Sci: Mater. Electron. **2007**, *18*, 367.
[81] J. C. Love, B. D. Gates, D. B. Wolfe, K. E. Paul, and G. M. Whitesides, Nano Lett. **2002**, *2*, 891.
[82] K. K. S. Lau, J. Bico, K. B. K. Teo, M. Chhowalla, G. A. J. Amaratunga, W. I. Milne, G. H. McKinley, and K. K. Gleason, Nano Lett. **2003**, *3*, 1701.
[83] J. Y. Shiu, C. W. Kuo, P. L. Chen, and C. Y. Mou, Chem. Mater. **2004**, *16*, 561.
[84] N. Chakrapani, B. Q. Wei, A. Carrillo, P. M. Ajayan, and R. S. Kane, Proc. Natl. Acad. Sci. **2004**, *101*, 4009.
[85] M. A. Correa-Duarte, N. Wagner, J. Rojas-Chapana, C. Morsczeck, M. Thie, and M. Giersig, Nano Lett. **2004**, *4*, 2233.
[86] H. Liu, S. H. Li, J. Zhai, H. J. Li, Q. S. Zheng, L. Jiang, and D. B. Zhu, Angew. Chem. Int. Ed. **2004**, *43*, 1146.
[87] W. Lee, M.-K. Jin, W.-C. Yoo, and J.-K. Lee, Langmuir **2004**, *20*, 7665.
[88] C. Journet, S. Moulinet, C. Ybert, S. T. Purcell, and L. Bocquet, Europhys. Lett. **2005**, *71*, 104.
[89] C. V. Nguyen, L. Delzeit, A. M. Cassell, J. Li, J. Han, and M. Meyyappan, Nano Lett. **2002**, *2*, 1079.
[90] J. G. Fan, D. Dyer, G. Zhang, and Y. P. Zhao, Nano Lett. **2004**, *4*, 2133.
[91] T. Karabacak, J. P. Singh, Y. P. Zhao, G. C. Wang, and T. M. Lu, Phys. Rev. B **2003**, *68*,
[92] R. F. Voss, R. B. Laibowitz, and E. I. Allessandrini, Phys. Rev. Lett. **1982**, *49*, 1441.
[93] J. G. Amar, F. Family, and P. M. Lam, Phys. Rev. B **1994**, *50*, 8781.
[94] D. R. Franca and A. Blouin, Meas. Sci. Technol. **2004**, *15*, 859.
[95] P. A. Kralchevsky, V. N. Paunov, N. D. Denkov, I. B. Ivanov, and K. Nagayama, J. Colloid Interf. Sci. **1993**, *155*, 420.
[96] J. G. Fan and Y. P. Zhao, Langmuir **2006**, *22*, 3662.
[97] M. Apel-Paz and A. Marmur, Colloid Surf. A **1999**, *146*, 273.

[98] A. M. Cazabat and M. A. C. Stuart, Colloid Polym. Sci. **1987**, *74*, 69.
[99] E. Kissa, J. Colloid Interf. Sci. **1981**, *83*, 265.
[100] A. Marmur, J. Colloid Interf. Sci. **1988**, *124*, 301.
[101] A. Borhan and K. K. Rungta, J. Colloid Interf. Sci. **1993**, *158*, 403.
[102] D. Danino and A. Marmur, J. Colloid Interf. Sci. **1994**, *166*, 245.
[103] H. Modaressi and G. Garnier, Langmuir **2002**, *18*, 642.
[104] D. Seveno, V. Ledauphin, G. Martic, M. Voue, and J. De Coninck, Langmuir **2002**, *18*, 7496.
[105] P. G. de Gennes, F. Brochard-Wyart, and D. Quere, *Capillary and Wetting Phenomena: Drops, Bubbles, Waves*. (Springer, New York, 2003).
[106] M. Sahimi, *Applications of Percolation Theory*. (Taylor & Francis Ltd, London, 1994).
[107] R. H. Lopez, A. M. Vidales, and G. Zgrablich, Physica A **2003**, *327*, 76.
[108] M. Ferer, G. S. Bromhal, and D. H. Smith, Physica A **2004**, *334*, 22.
[109] Y.-P. Zhao and J.-G. Fan, Appl. Phys. Lett. **2006**, *88*, 103123.
[110] F. P. Beer, E. R. Johnson Jr., and J. T. Dewolf, *Mech. Mater.* (McGraw-Hill, New York, 1996).
[111] R. R. Rye, J. A. Mann, and F. G. Yost, Langmuir **1996**, *12*, 555.
[112] P. G. de Gennes, Rev. Mod. Phys. **1985**, *57*, 827.
[113] J. G. Fan and Y.-P. Zhao, submitted to Nanotechnology
[114] B. Rubinsky and D. E. Pegg, Proc. R. Soc. B **1988**, *234*, 343.
[115] C. Y. Lee and J. Bastacky, Cryobiology **1995**, *32*, 299.
[116] Z. F. Cui, R. C. Dykhuizen, R. M. Nerem, and A. Sembanis, Biotechnol. Prog. **2002**, *18*, 354.
[117] R. Viskanta, M. V. A. Bianchi, J. K. Critser, and D. Gao, Cryobiology **1997**, *34*, 348.
[118] K. A. Jackson and B. Chalmers, J. Appl. Phys. **1958**, *29*, 1178.
[119] K. A. Jackson, D. R. Uhlmann, and B. Chalmers, J. Appl. Phys. **1966**, *37*, 848.
[120] T. Duffar and M. Bal, J. Cryst. Growth **1995**, *151*, 213.
[121] J.-G. Fan and Y.-P. Zhao, Appl. Phys. Lett. **2007**, *90*, 013102.
[122] H. K. Christenson, J. Phys.:Condens. Matter **2001**, *13*, R95.
[123] J. G. Fan, J. X. Fu, A. Collins, and Y.-P. Zhao, Nanotechnology (accepted) **2007**,
[124] D.-X. Ye, T. Karabacak, G.-C. Wang, and T.-M. Lu, Nanotechnology **2004**, *15*, 817.
[125] D.-X. Ye, T. Karabacak, R. C. Picu, G.-C. Wang, and T.-M. Lu, Nanotechnology **2005**, *16*, 1717.
[126] L. H. Tanner, J. Phys. D: Appl. Phys. **1979**, *12*, 1473.
[127] J. Lopez, C. A. Miller, and E. Ruckenstein, J. Colloid Interf. Sci. **1976**, *56*, 460.
[128] H. Xu, D. Shirvanyants, K. Beers, K. Matyjaszewski, M. Rubinstein, and S. S. Sheiko, Phys. Rev. Lett. **2004**, *93*,
[129] T. Gillespie, J. Colloid Sci. **1958**, *13*, 32.
[130] V. M. Starov, S. R. Kostvintsev, V. D. Sobolev, M. G. Velarde, and S. A. Zhdanov, J. Colloid Interf. Sci. **2002**, *252*, 397.
[131] V. M. Starov, S. R. Kosvintsev, V. D. Sobolev, M. G. Velarde, and S. A. Zhdanov, J. Colloid Interf. Sci. **2002**, *246*, 372.
[132] D. Quere, Europhys. Lett. **1997**, *39*, 533.
[133] K. G. Kornev and A. V. Neimark, J. Colloid Interface Sci. **2001**, *235*, 101.
[134] R. Lenormand, J. Phys.: Condens. Mat. **1990**, *2*, SA79.
[135] E. Lorenceau, D. Quere, J. Y. Ollitrault, and C. Clanet, Phys. Fluids **2002**, *14*, 1985.